Phonon Transport in Nanowires – Beyond Classical Size Effects

By

Lin Yang

Dissertation

Submitted to the Faculty of the

Graduate School of Vanderbilt University

in partial fulfillment of the requirements

for the degree of

DOCTOR OF PHILOSOPHY

in

Mechanical Engineering

May 10, 2019

Nashville, Tennessee

Approved:

Deyu Li, Ph.D.
Leon Bellan, Ph.D.
Joshua Caldwell, Ph.D.
D. Greg Walker, Ph.D.
Yaqiong Xu, Ph.D.

ACKNOWLEDGEMENTS

I would like to sincerely thank my advisor, Dr. Deyu Li, for giving me the opportunity to work with his research group and introducing me to the field of nanoscale thermal transport. His expertise, guidance and encouragement helped me overcome the challenges in my scientific endeavors, and allowed me to grow and flourish during my studies. I benefited tremendously from the inspiring discussions with him, and he continues to exemplify the importance of rigorous attitude and critical thinking in the scientific and academic process.

Next, I express my deepest gratitude to my committee members: Dr. Leon Bellan, Dr. Joshua Caldwell, Dr. Greg Walker, and Dr. Yaqiong Xu. Thank you for your time, patience, and helpful guidance throughout this process. I would also like to thank my collaborators at Vanderbilt, UNCC, Tulane, and Southeastern University in China. Without your help, the work presented in this dissertation would not be possible.

Thank you my colleagues in Micro/Nanoscale Thermal Fluids lab for the help, company, and friendship in the past five years. In particular, I am very grateful for the help and instructions of Dr. Qian Zhang during the beginning stage of my PhD study. I thank all the lovely and kind friends I met at Vanderbilt and Nashville, and it is a great pleasure to have you all in my life.

Finally, I am deeply appreciative of the love, support, and encouragement of my parents and grandparents. Thank you for always motivating me to try and excel in any interest I had, and thank you for making this journey possible.

TABLE OF CONTENTS

LIST OF FIGURES

Figure Page

Chapter 1

Introduction

Thermal transport in one dimensional nanostructures, such as nanowires, nanotubes, and nanoribbons of various morphologies, has attracted great attention because of the intriguing physics at nanoscale and the significance for technological applications in nanoelectronics, energy conversion and thermal management (Kim et al. 2001, Li et al. 2003b, Qing et al. 2014, Termentzidis et al. 2013, Yang et al. 2017, 2019; Zhang et al. 2017). This has fueled a significant body of research aiming at understanding the fundamental, microscopic origins of energy transport in nanostructures, and to realize the rational engineering of thermal transport properties.

For a nanostructured material, as the characteristic size shrinks to be smaller than the phonon mean free path (MFP), heat conduction via phonons will shift from diffusive to ballistic transport regime. In this latter case, phonons can travel through the medium without internal scattering, which could lead to absence of local temperature or thermodynamic equilibrium, and the interaction of phonons with surfaces or interfaces governs the energy transport. Therefore, the thermal conductivity becomes a property that depends on the system size, and this understanding is well-recognized as the classical size effect.

In the past two decades, the thermal conductivities of many different kinds of nanowires/nanoribbons have been explored and the underlying mechanisms governing the transport process have been dissected. In general, beyond the well-recognized classical size effect due to phonon-boundary scattering, several new factors, such as acoustic softening, surface roughness, and complex morphology, have been shown to be able to significantly alter the thermal conductivity of nanowires. Here, one particular example of great interest is to combine various

phonon scattering mechanisms to reduce the lattice thermal conductivity for thermoelectric energy conversions.

In view of the great relevance to practical applications, this dissertation seeks to further the understanding of the complicated transport dynamics in thin nanostructures and at their interfaces, and to answer some of the fundamental questions on interactions between energy and charge carriers in quasi-one-dimensional systems. In the introduction section, we will briefly review the existing work on the major nanoscale effects governing thermal transport through nanowires. It is important to point out that the fundamental understandings obtained from the study of nanowires have also greatly advanced our understanding of thermal transport in materials beyond nanowires. This is because the wire surface provides important boundary conditions to examine the contributions of different scattering mechanisms to the transport of energy carriers.

1.1 Classical Size Effects

For semiconductors and insulators, heat transport is dominated by quantized atomic vibrations (i.e. phonons). Owing to the extremely large surface-area-to-volume ratios, for structures with at least one dimension in nanoscale, such as thin films, nanowires, and nanotubes, the thermal transport properties is predominately dependent on the phonon interactions with the boundaries, or the classical size effect. If we treat the phonons as particles, their transport can be described using the kinetic theory where the thermal conductivity κ is formulated as:

$$\kappa = \frac{1}{3} c v \Lambda \,. \tag{1.1}$$

Here, c, v, and Λ are heat capacity, speed of sound, and phonon mean free path (MFP), respectively. The phonon MFP defines the average distance a phonon travels before it gets scattered, and the overall phonon MFP (Λ) is related to the individual MFPs according to the specific scattering mechanisms by the Matthiessen's rule:

$$\frac{1}{\Lambda}=\frac{1}{\Lambda_U}+\frac{1}{\Lambda_d}+\frac{1}{\Lambda_{e-ph}}+\frac{1}{\Lambda_b}, \tag{1.2}$$

where Λ_U, Λ_d, Λ_{e-ph}, and Λ_b are MFPs determined by the Umklapp scattering, defects scattering, electron-phonon scattering, and boundary scattering, respectively. The first three terms determine the intrinsic phonon MFP (Λ_i) in bulk materials and the last term, which is only important at very low temperatures for bulk materials, could become much more significant for nanostructures. For nanostructures with a characteristic length (i.e., Casimir length) smaller than the intrinsic phonon MFP, the effective phonon MFP could be drastically reduced by phonon boundary scattering with Λ_b as the dominant term on right-hand side in Eqn. (1.2).

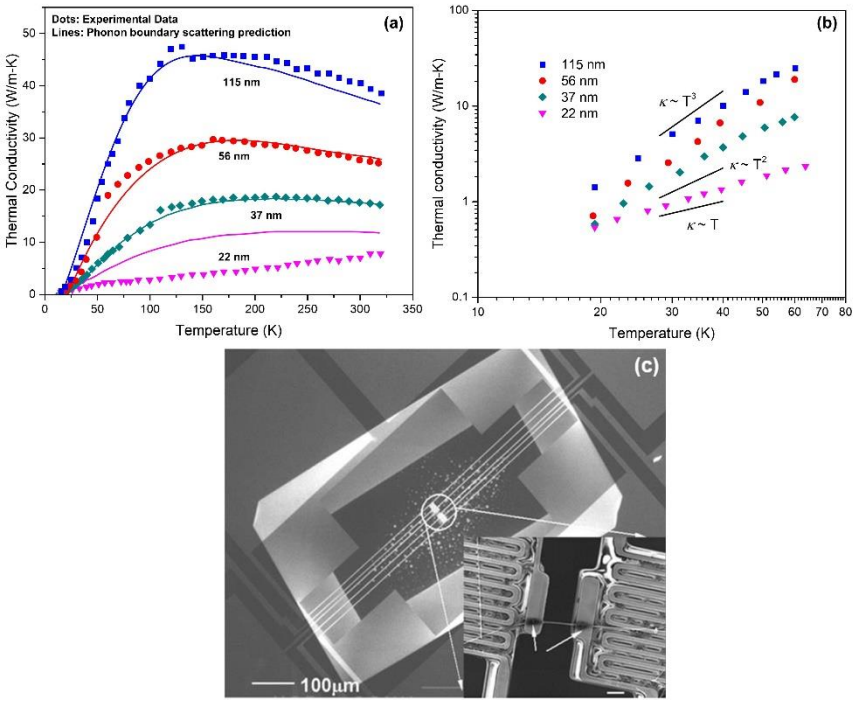

Figure 1.1 (a) Measured thermal conductivity of different diameter Si nanowires (Li et al. 2003b) as well as the fitted results (Mingo et al. 2003). The number besides each curve denotes the corresponding wire diameter. (b) Low temperature experimental data on a logarithmic scale. Also shown are T^3, T^2, and T^1 curves for comparison. (c) SEM images of the suspended micro-bridge device. The lower inset shows a 100 nm Si nanowire bridging the two side-by-side suspended membranes, with wire-membrane junctions wrapped with locally-deposited amorphous carbon (shown by arrows) to minimize the contact thermal resistance (Li et al. 2003b).

A prime example of the classical size effect can be observed in the thermal conductivity of Si nanostructures, including thin films and nanowires (Ju & Goodson 1999, Li et al. 2003b). Through measuring the thermal conductivities of 74–240 nm thick silicon thin films, Ju and Goodson first pointed out that the thermal conductivity of Si films is strongly size dependent, and phonon boundary scattering could reduce the thermal conductivity by up to 50% at room temperature (Ju & Goodson 1999). Their analysis further indicated that the intrinsic phonon MFP in Si could be as long as 300 nm at room temperature, which is much longer than the value of 43 nm predicted when phonon dispersion is neglected (Ju & Goodson 1999). Later, Li et al. conducted a systematic thermal conductivity measurement on individual Si nanowires with diameters of 22, 37, 56, and 115 nm. The measured thermal conductivity shows more than one magnitude reduction compared with the corresponding bulk value, and also demonstrate a strong size dependence with lower thermal conductivity for smaller diameter wires, as shown in **Figure. 1.1a** (Li et al. 2003b).

This set of data attracted significant attention and extensive efforts have been made to model thermal transport in Si nanowires and explain the underlying transport mechanisms (Chen et al. 2008, Dames & Chen 2004, Mingo 2003, Mingo et al. 2003). The reduced thermal conductivity of Si nanowires, except for the 22 nm diameter wire, have been successfully explained based on the classical size effects, considering the reduced effective MFP caused by diffusive phonon boundary scattering (Mingo et al. 2003). However, for the 22 nm diameter wire, as shown in **Figure 1.1a**, the measured thermal conductivity is significantly lower than the theoretical prediction and showed an unusual linear temperature dependence with no peak over the measured temperature range. This is in contrast to the behavior of the larger diameter nanowires where we observe a peak thermal conductivity shifting to a higher temperature with decreasing wire diameters, indicating the growing importance of boundary scattering over Umklapp scattering.

To further examine phonon transport in these Si nanowires, the measured low temperature thermal conductivity data are plotted in **Figure 1.1b**, where the T^3, T^2, and T^1 curves are also plotted for comparison. At low temperatures, the thermal conductivity of relatively larger diameter wires (115 and 56 nm) exhibits a Debye T^3 dependence, similar to bulk Si. The transition occurs near ~30 nm. As the wire diameter shrinks to 37 nm, the measured thermal conductivity starts to deviate from the cubic trend. Further size reduction leads to a linear temperature dependence of the thermal conductivity observed in the 22 nm diameter nanowire. This suggests that for Si nanowires with diameters below ~20 nm, novel size effects beyond the classical boundary scattering could play an important role. The linear temperature dependence of the wire thermal conductivity was later confirmed by a group of thin Si nanowires with diameters all below 30 nm (Chen et al. 2008).

In the discussion above, the MFP due to phonon-boundary scattering is normally assumed to be the same for all phonon modes, and theories based on the assumption that the MFP is proportional to the nanowire diameter and independent of phonon frequency are able to explain the observed experimental results of Si nanostructures with critical dimension larger than 30 nm (Mingo 2003, Volz & Chen 1999a). However, because of the wide spectral distribution of heat carriers, this gray approximation severely underestimates the MFP of the phonons that contribute significantly to thermal conductivity. Thus, it is critical to quantify the contributions of different phonon modes with microscopic details for using nanostructuring approach to tailor the thermal conductivity.

Recent first-principles calculations predict that the phonon MFP relevant to thermal transport vary by more than 5 orders of magnitude in bulk Si (Ward & Broido 2010). Experimentally, both time domain thermoreflectance (TDTR) and x-ray transient grating technique were developed to

measure ballistic phonon transport in nanostructures (Koh & Cahill 2007, Minnich et al. 2011). However, spot-size limitations due to the diffraction limit of light and an upper limit to the modulation frequency achievable with pulsed lasers restrict TDTR's ability to probe a broad range of the MFP spectrum. More recently, through varying the modulation frequency of the continuous wave lasers in the broadband frequency domain thermoreflectance (BB-FDTR), Regner et al. extend the lower bound of the thermal penetration depth, L_p, of the pump laser down to 40 nm (Regner et al. 2013). Armed with this technique, they reported the first experimentally measured phonon MFP spectrum of bulk c-Si at device operating temperatures. As shown in **Figure 1.2**, the measured thermal conductivity of single crystalline bulk Si is plotted against L_p from 0.3-8 μm for different temperatures. Different from the classical kinetic theory, where the estimated phonon MFP based on Eqn. (1.1) is only 41 nm, it can be seen that phonons with MFPs longer than 1 μm contribute ~40% to bulk thermal conductivity at 311 K, and as temperature reduces, contribution from long MFP phonons further increases. Their measured results are also plotted to compare with the first-principle predictions (Esfarjani et al. 2011, Minnich et al. 2011); and the good agreement between the experimental data and theoretical prediction stresses again the importance of low-frequency phonons.

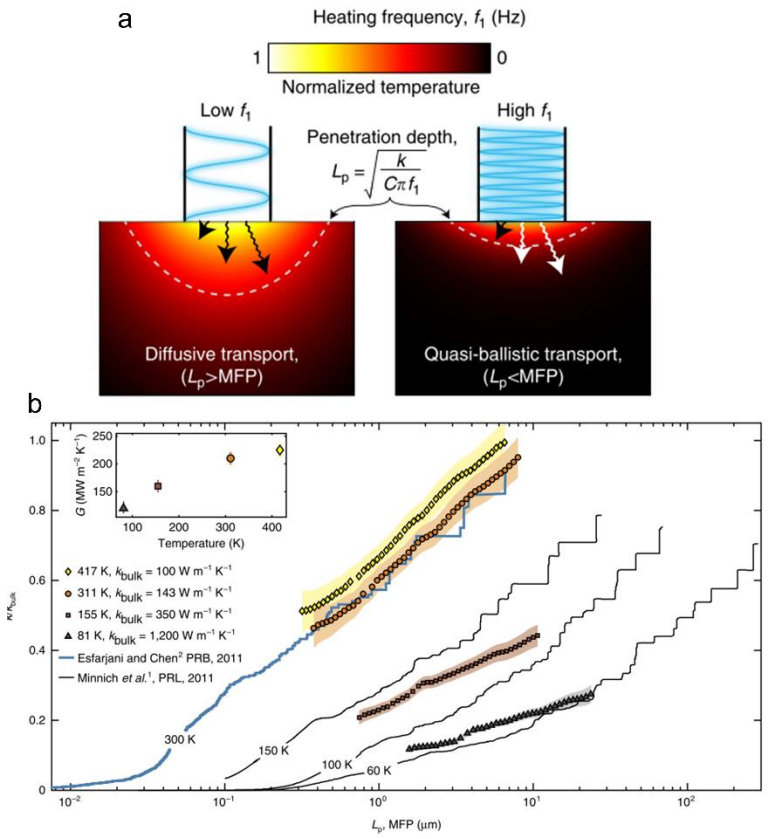

Figure 2.2 (a) Illustration of diffusive and ballistic transport. At low heating frequencies, when the thermal penetration depth L_p is greater than the phonon MFP, phonon transport is manily diffsuive, and a bulk value of thermal conductivity is measured. At high heating frequencies, the L_p decreases below the MFP of some phonons, which travel ballistically through the thermally affected zone (white arrows). (b) MFP spectra for intrinsic c-Si at T equals to 81, 155, 311, and 417 K compared with MFP predictions from first-principles calculations. At T = 311 K, phonons with MFP > 1um contribute 40% to bulk thermal conductivity (Esfarjani et al. 2011, Minnich et al. 2011, Regner et al. 2013).

Meanwhile, using Molecular Dynamics (MD) simulations, the phonon wavelength (λ) in Si is also shown to possesses a spectrum distribution, but the distribution range is much narrower compared with the MFP spectra, and is calculated to change from 0.5 to 6 nm at 277 K (Esfarjani et al. 2011). Their results indicate that while most thermal phonons have similar wavelength, the associated MFPs can vary by orders of magnitude. Therefore, it is crucial to consider the phonon MFP spectrum when interpreting the thermal measurement results in bulk and nanostructured materials.

Another important point is the contribution from the optical phonon modes to heat conduction in nanostructures. Due to their small group velocity, the optical phonon contribution is typically neglected, which is confirmed to be valid for bulk Si and Ge (Ward & Broido 2010). However, when the system size reduces to the nanoscale regime, boundary scattering suppresses the capability of acoustic phonons to transport heat, and the contribution from optical phonons is no longer negligible. Using first-principles calculations, Tian et al. show that for a 20 nm diameter Si nanowire, the optical phonons can contribute up to 18% at room temperature, as compared to only 5% for bulk Si (Tian et al. 2011). This understanding is also supported by a recent experimental work on thermal conductivity of individual Si nanowires with measurement temperature extended to 700 K (Lee et al. 2016a). It was shown that for a 20 nm diameter Si nanowire, the contribution from the optical phonons could be 20% at 700 K, and the relative importance of the optical phonons increased for smaller sized wires.

1.2 Acoustic Softening Effects

As shown in **Figure 1.1b**, even though the measured thermal conductivity of Si nanowires with diameters larger than 37 nm could be well captured by the phonon boundary scattering prediction, we do observe an outlier for the 22 nm diameter nanowire, where the measured thermal conductivity is significantly lower than the prediction based on the classical size effects. Similar behavior has been also observed in thin Ge nanowires as shown in **Figure 1.3c**, where the measured thermal conductivity deviates from the phonon boundary scattering prediction drastically for wires with diameters smaller than 15 nm (Wingert et al. 2011a).

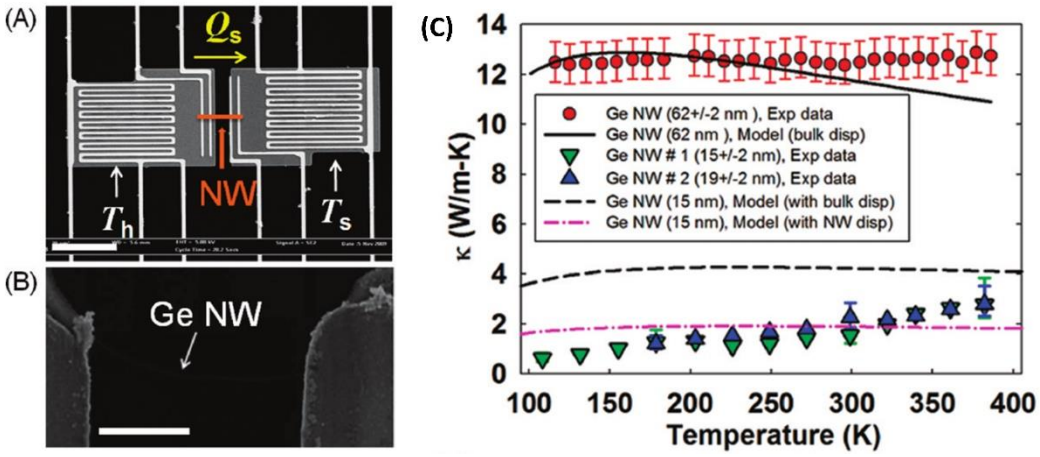

Figure 1.3 (A) A SEM image of a micro-fabricated device used for single nanowire κ measurement. (B) A SEM image of a ~15 nm Ge NW on the suspended device. (C) The calculated κ of the 62 nm Ge NW using bulk dispersions (black solid line) agree well with the experimental data (circles), whereas the calculated κ of the 15 nm Ge NW using bulk dispersions (black dashed line) is significantly higher than the experimental data (triangles), by more than 100% below 250 K. Modeling results using NW dispersions (pink dash-dot line) show good agreement with the data (Wingert et al. 2011b).

A lot of efforts have been paid to explain this unexpected observation. Theoretical studies suggest that for Si nanowires with diameter smaller than ~30 nm, the phonon dispersion relation could be modified due to phonon confinement, such that the phonon group velocity would be significantly less than the bulk value (Wingert et al. 2011b, Zou & Balandin 2001). This is further corroborated by the measured phonon dispersion relations using the angle-resolved Brillouin light scatterings, where a steep drop of phonon velocities for the fundamental flexural modes could be observed as the Si film thickness reduces to below ~30 nm (Cuffe et al. 2012). This observation indicates that, at these small size scales, the effective elastic constants have been reduced from bulk values, which would lead to changes in the elastic modulus of the nanostructure.

More recently, Wingert et al. performed systematic thermal conductivity measurements on ultrathin Si nanotubes (NTs) with wall thickness as small as 5 nm. Similar to wires with diameter smaller than 30 nm, the Si NTs also showed a thermal conductivity reduction much stronger than

that could be accounted for by diffusive boundary scattering effects (Wingert et al. 2015), and in fact, the values are even lower than that of amorphous Si NTs with similar geometries. It is noteworthy that from the elastic tensile tests on individual Si nanowires, the measured Young's modulus shows a steep reduction from the bulk value when the wire diameter is thinner than 30 nm (Zhu et al. 2009). Similar characterization on each Si NTs yielded Young's modulus up to 6-fold lower than the bulk value (shown in **Figure 1.4b**). Since speed of sound is proportional to the square root of Young's modulus, the drastically reduced Young's modulus value indicates strong elastic softening in thin Si and Ge nanowires as well as the crystalline Si NTs with thin walls, which subsequently leads to lower thermal conductivity (Wingert et al. 2015). This new finding by Wingert et al. thus points out a new route to further reduce the lattice thermal conductivity and enhance the thermoelectric performance of nanowires (Wingert et al. 2015).

Recently, the acoustic softening effect has also been used to explain the ultra-low thermal conductivity of porous silicon nanowires (~0.33 W/m-K at 300 K for a porosity of 43%) (Chiam et al. 2017); however, in general, the multi-physics phenomena of acoustic softening still have not been well explored. For example, while acoustic softening and the associated thermal conductivity reduction have been confirmed for Si nanowires, no combined study of both mechanical and thermal properties for other type of nanowires have been carried out, while Young's modulus reduction has been observed for several other kinds of nanostructures. For example, measurement on thin Cr cantilevers shows that the measured Young's modulus exhibits a continuous decreasing trend as the size is reduced to below 83 nm (Nilsson et al. 2004).

Theoretically, the reduced Young's modulus of the nanostructures could be explained based on an approximate core-shell composite model. In this model, The core has the elastic modulus of the corresponding bulk material E_0, while the surface shell possesses a surface modulus E_s, which

is correlated to the surface bond length contractions (Chen et al. 2006). As such, we have $EI = E_0 I_0 + E_s I_s$, where EI is the effective flexural rigidity of the composite nanowire, with E the effective Young's modulus, I_0 and I_s the moment of inertia of the core and shell, respectively. As such, the value E_s/E_0 becomes the critical parameter determining the tendency of the size dependence of the Young's modulus of a nanostructured material.

This theory is further corroborated by the argument that the Young's modulus of single crystalline materials depends heavily on its interatomic bond energy and lattice structure (Li et al. 2003c). For the surface atoms, owing to the lower coordination numbers and electron densities compared to the bulk counterpart, they tend to adopt different bond spacing, leading to an associated energy different from those in the core (Sadeghian et al. 2011). For example, simulations show that Si surface stress is compressive in nature and require atomic reorganization as well as bond lengthening to reach an equilibrium state, which eventually leads the elastic modulus of surface atoms to be much lower than that of core atoms (Miller & Shenoy 2000, Shim et al. 2005). Therefore, as the surface-area-to-volume ratio increases beyond a threshold value, the Young's modulus of Si nanostructures shows a decreasing trend, as demonstrated in the measurements and theoretical modeling (Wingert et al. 2015, Yao et al. 2012, Zhu et al. 2009).

However, investigations on some other nanostructured materials show an opposite tendency, i.e., their Young's moduli increases rapidly with decreasing diameters. For example, the bending modulus of carbon nanotubes (CNTs) (Poncharal et al. 1999) and Young's moduli of Ag, Pb (Cuenot et al. 2004) and ZnO nanowires (Chen et al. 2006) are found to be much higher than their bulk counterparts. **Figure 1.4d** plots the measured Young's modulus of ZnO nanowires along the axial direction for wires with diameters from 17 to 550 nm, and it is found that the Young's modulus increases drastically as the size reduces to below 120 nm. This stems from the opposite

surface atom binding condition compared with that of Si. For materials like ZnO, the effect of bond contractions at the surface will be more significant than that in the core part (Chen et al. 2006). As such, instead of lowering the nanostructure's elastic properties as the surface-area-to-volume ratio increases, the elastic stiffening effect will boost the Young's modulus as the size reduces.

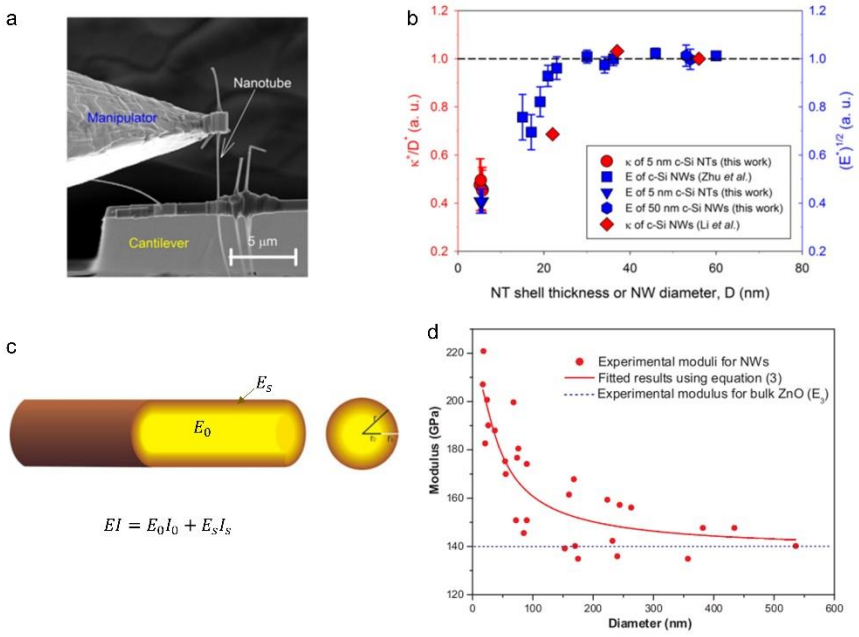

Figure 1.4 (a) Elastic modulus tensile measurement using manipulator probe to pull a Si NT attached to the end of an AFM cantilever. (b) Correlation between thermal conductivity (κ) and elastic modulus (E) in crystalline NTs and NWs. *κ*, *D*, and *E* have been normalized with their respective values for ~60 nm Si NWs (Wingert et al. 2015). (c) Schematic illustration of the core-shell composite NW model. (d) Diameter dependence of measured Young's modulus in [0001] oriented ZnO nanowires, where the red dots are experimental results, and solid line is fitted results by the core-shell composite NW model (Chen et al. 2006).

It is important to note that results from separate thermal measurement of ZnO nanowires conducted by Bui et al. (Bui et al. 2012) did not reflect the effects of the Young's modulus change, where the measured thermal conductivity exhibits a continuous decreasing trend for wires with diameter reducing from 209 to 70 nm. This could be due to the fact that the smallest pristine nanowire they measured is still 70 nm diameter, while more remarkable Young's modulus

enhancement occurs for wires of <50 nm in diameter according to Chen et al. (Chen et al. 2006). In addition, even though the elastic softening effect could reasonably explain the thermal conductivity reduction beyond the classical size effect, a full scope study of all changes in the heat capacity, phonon group velocity and MFP from the Young's modulus change in small nanowires should be carried out to dissect how different factors contribute to thermal conductivity variations. Finally, further study is still needed to elucidate the role of the acoustic softening on the deviation of T^3 dependence of thermal conductivity in smaller-sized Si nanostructures (**Figure 1.1**).

1.3 Surface Roughness Effects

Besides thin nanowires, surface roughened Si nanowires have also shown drastic thermal conductivity reduction, and the significant reduction was exploited to enhance the thermoelectric property of silicon nanowires, achieving a thermoelectric figure of merit more than two orders of magnitude higher than the bulk value (Boukai et al. 2008, Hochbaum et al. 2008). Shown in **Figure 1.5** is the measured thermal conductivities of electroless etched rough Si (EE-Si) nanowires. Compared with smooth nanowires of similar diameters, the Si nanowire with rough surfaces demonstrate much lower thermal conductivity, even approaching the amorphous limit for ~50 nm diameter wires, which is far below any prediction based on the classical size effects. This intriguing observation has attracted a great deal of attention and fueled a lot of research to explore the detailed mechanisms responsible for the ultra-low thermal conductivity.

Experimentally, Lim et al. conducted extensive measurements of rough-surface Si nanowires through simultaneously characterizing both the thermal conductivity and surface roughness of the same nanowire (Lim et al. 2012). Instead of using nanowires prepared via electroless etching, the nanowires were prepared through surface etching of smooth nanowires prepared with vapor-liquid-solid method. Quantitative parameters describing the surface roughness were extracted from

detailed transmission electron microscopy (TEM) characterization of the surface roughness. It was shown that larger surface roughness corresponded to lower thermal conductivity; and importantly, the thermal conductivity value could indeed drop far below the Casimir limit. In a separate effort, Blanc et al. fabricated Si nanoribbons with corrugated sidewalls using e-beam lithography and the measured thermal conductivity values were shown to be strongly reduced compared with straight wire, which provided additional evidence for that surface roughness could indeed reduce the thermal conductivity below the Casimir limit (Blanc et al. 2013). To explore the underlying mechanisms, Monte-Carlo (MC) ray-tracing simulations were carried out, which indicated that backscattering of ballistic phonons on the corrugated surfaces could pose significant resistance to phonon transport. In the best case, their results show that the effective MFP could be reduced by a factor of nine from that of the corresponding straight nanowire (Blanc et al. 2013). One limitation is that the experiment was done in a relatively small range of very low temperature spanning 0.3 to 5 K, where the wave length of thermal phonons could be much larger than the random surface roughness, and the phonon wave nature and phonon confinement might also play important roles.

Theoretically, the effects of non-smooth surface on the thermal transport of nanowires was also investigated by Moore et al. through applying MC simulations to study phonon transport in a nanowire with periodic sawtooth features on the surface (Moore et al. 2008). Their results show that despite the increase in the solid volume of the nanowire, phonon backscattering could suppress the thermal conductivity. However, the modeled thermal conductivity reduction is not sufficiently large to appraoch the thermal conductivity values reported for rough EE-Si nanowires (Moore et al. 2008). To understand the discrepancy between the experimental data and the prediction based on phonon particle transport theories, Martin et al. introduced an additional frequency-dependent phonon scattering term to characterize the phonon interaction with the surface roughness (Martin

et al. 2009). Based on the first order perturbation theory, also known as the Born approximation, the roughness induced volumetric phonon scattering rate was calculated and the thermal conductivity was derived. Their results show that the modeled thermal conductivity can be well modulated by adjusting the surface roughness, which could adequately reproduce the drastic reduction of measured thermal conductivity values with a root-mean-square (RMS) roughness, σ, of 3-3.25 nm. Moreover, they found that, instead of following a linear *D* dependence of the thermal conductivity for smooth nanowires, the roughened nanowire exhibits a clear $(D/\sigma)^2$ dependence (Martin et al. 2009).

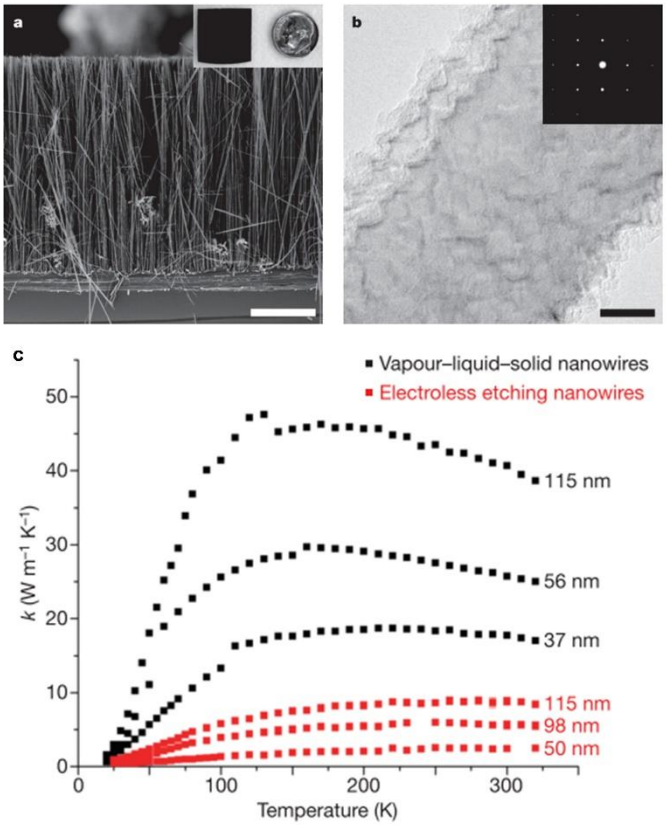

Figure 1.5 (a) Cross-sectional SEM of an EE Si nanowire array. (b) TEM image of a segment of an EE Si nanowire. The roughness is clearly seen at the surface of the wire. The selected area electron diffraction pattern (inset) indicates that the wire is single crystalline all along its length. (c) The temperature-dependent κ of VLS (black squares) (Li et al. 2003b) and EE nanowires (red squares). The peak κ of the VLS nanowires is 175–200 K, while that of the EE nanowires is above 250 K. Moreover, the measured thermal conductity of the rough Si nanowire are significantly lower than wires of similar diameter but with smooth surfaces (Hochbaum et al. 2008).

For the Born approximation, however, one strict assumption is that the phonon wavelength should be comparable with the roughness correlation length L_c, and failing to meet this condition would underestimate the transmission coefficient by one order of magnitude (Sadhu & Sinha 2011). As such, to accurately describe the phonon transport behavior in rough Si nanowires, Sadhu et al. employed a different Bourret approximation and in combination with the Green's function, they calculated the phonon transmission coefficient in 50 nm diameter nanowires of different σ and L_c values. From the calculation, they found that multiple scattering of phonons from correlated points on the wire surface lead to strong attenuation of phonon group velocity, which results in non-propagating vibrational modes. By setting $\sigma = 2.5\ nm$ and $L_c = 30\ nm$, they were able to obtain a phonon transmission coefficient well below the Casimir limit, and the result was used to fit the measured thermal conductivity of the 50 nm diameter rough Si nanowire (Sadhu & Sinha 2011). Their results further show that in addition to the RMS surface roughness, the correlation length could also play a critical role. However, validation of the assumptions for the model needs to be done to confirm the accuracy of the model.

Efforts have also been made to clarify the surface roughness effects through molecular dynamics (MD) simulations. Using non-equilibrium MD simulations (NEMD), Liu and Chen showed that the derived thermal conductivity reduces as the periodic length of the surface roughness decreases (Liu & Chen 2010). However, as the simulation was conducted on very small nanowires (~1.63 nm diameter), and roughness RMS was limited, and no quantitative comparison with the experimental results could be made. On the other hand, He and Galli conducted a systematic equilibrium MD simulation of Si nanowires of 15 nm diameter of different surface morphologies and with or without internal structural defects (grain boundaries and vacancies) (He & Galli 2012). Their results suggested that amorphous surface layers, surface oxide, surface

roughness, and internal structural defects could all contribute to reduced thermal conductivity. For a 13 nm diameter smooth Si nanowire core coated with 1 nm thick amorphous oxide, the modeled thermal conductivity could achieve a 10-fold reduction with respect to the bulk value. Moreover, by constructing a rippled nanowire coated with thin oxide layer with 1 nm sized nanovoids in Si core, they found that the thermal conductivity of the 15 nm diameter wire could achieve nearly 40-fold reduction compared to bulk value (He & Galli 2012). Note that this magnitude of thermal conductivity reduction is comparable to what Hochbaum et al. observed in their rough Si nanowires (Hochbaum et al. 2008), but the nanowire size in the modeling is still much less than the ~50 nm diameter in the experimental study of EE-Si nanowires.

In summary, the surface roughness could indeed be effective in reducing thermal conductivity of nanowires; however, to date, a straightforward physical picture that can quantitatively account for how surface roughness could lead to drastically low thermal conductivity is still not available. Further experimental and theoretical studies on nanowires with well designed and characterized surface roughness should be carried out to clarify this important issue. It is also worth noting that for EE-Si nanowires etched from highly doped Si wafers, the etching process might generate some internal structural defects such as voids (Hochbaum et al. 2009), which was utilized by Hippalgaonkar to study the ultralow thermal conductivity in nanoporous Si nanowires (Chiam et al. 2017). While nanoscale voids were not observed in the rough EE-Si nanowires studied by Hochbaum et al. (Hochbaum et al. 2009), which were etched from lightly doped Si wafers, the impact on the low thermal conductivity by smaller, atomistic scale impurities cannot be completely ruled out.

1.4 Effects of Complex Morphologies

In addition to the simple straight nanowires, wires with more complex morphologies have been synthesized and the effects of morphologies on thermal transport have been investigated. In this session, several strategies will be discussed to fabricate nanostructures with complex structures to tune the thermal conductivity.

Previous studies on Si thin films and nanowires as well as wires with roughened surface have demonstrated thermal conductivity values as small as two orders of magnitude lower than the bulk counterpart (Chen et al. 2008, Hochbaum et al. 2008, Ju & Goodson 1999, Li et al. 2003b). However, this size-dependent thermal conductivity occurs mostly through modification of phonon relaxation rates in the phonon particle picture. On the other hand, studies have been going on to design and fabricate Si nanostructures of complex morphologies, and thus exploit coherent phonon processes to further reduce the lattice thermal conductivity (Ravichandran et al. 2013, Venkatasubramanian 2000). This theory has been applied to explain the recently measured low thermal conductivity of Si nanomeshes (Yu et al. 2010).

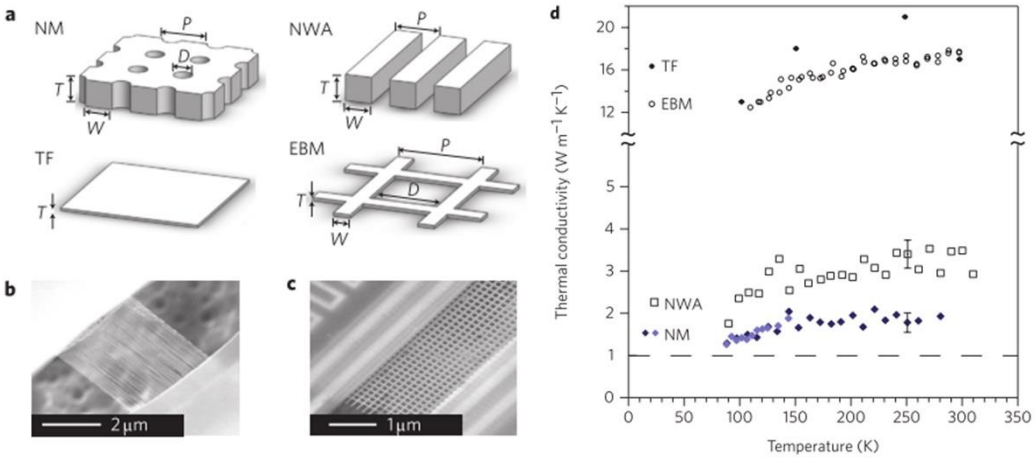

Figure 1.6 (a) Geometry of the two nanomesh films (NM1 and NM2) and three reference systems (TF, EBM and NWA). (b-c) SEM images of suspended nanowires in the NWA device (b) and suspended EBM device (c). (d) Thermal conductivity versus temperature for two nanomesh devices (diamonds) and the three reference devices, and the dash represents the thermal

conductivity of the amorphous Si (Yu et al. 2010).

As shown in **Figure. 1.6**, through fabricating periodic, single-crystal Si nanomesh structures with electron beam lithography (EBL), Yu et al. were able to achieve a room-temperature thermal conductivity of 2 W m^{-1} K^{-1}, which is about a factor of two lower than the already low thermal conductivity of ~3.5 W m^{-1} K^{-1} for patterned Si nanowires of a comparable critical dimension of 20 nm. As the surface-area-to-volume ratio of the nanomesh is even lower than that of the nanowire, the relaxation time related with the phonon boundary scattering of the nanomesh would only be larger; and the authors believed that the possible reason for the ultra-low thermal conductivity could be phonon coherence. It was argued that the holes played the role of Bragg reflectors, and phonons reflected from the successive sidewalls of the nanomeshes would interfere with each other, resulting in phononic band gaps in the dispersion relation, and hence lower phonon group velocity. Later, this phonon coherence picture is applied to explain the measured low thermal conductivities of other Si nanomeshes with various configurations (Alaie et al. 2015, Anufriev & Nomura 2015).

However, detailed analysis suggests that the conditions for phonon coherence to be predominate are very strict (Jain et al. 2013). Jain et al. argued that coherent phonon modes will emerge only if (i) phonons scatter specularly off the pore sidewalls to keep their phase information; (ii) phonon-phonon scattering probability is low when travelling between consecutive pore interfaces to retain the same frequency. For the first requirement, as there always exists a thin layer of native amorphous oxide (~2 nm) on the surface of silicon, phonons travelling to the surfaces will mostly be diffusively scattered (at 300 K, λ = 1-2 nm), making the quality of the periodicity unfavorable for phonon coherence. As for the second, in order to ensure low phonon-phonon scattering rates, the phonon MFP should be much larger than the characteristic length, and the number of populated phonon modes should be very small, which can both be realized only at low

temperatures. Meanwhile, following the particle feature of phonons in the MC model with bulk properties modified by phonon-boundary scattering, the calculated in-plane thermal conductivity of Si nanomeshes agree well with the experimental results. Therefore, they conclude that it is still valid to treat phonons as particles for thermal transport in nanomeshes with feature sizes greater than 100 nm (Jain et al. 2013).

Later, using MC simulations to solve the Boltzmann transport equation, Ravichandran and Minnich (Ravichandran & Minnich 2014) showed that taking into account the surface amorphous layer of 3.5 nm thick, the simulation results purely based on a particle picture of phonons could match the experimental data of Yu et al. (Yu et al. 2010). However, the thickness of native oxide on the silicon surface is usually only ~2 nm, significantly less than the required 3.5 nm to achieve a good fit. On the other hand, we note that the nanomeshes of Yu et al. have a large surface-area-to-volume ratio, which is in the regime where significant acoustic softening could occur; and as such, some additional reduction could be due to reduced Young's modulus and related phonon dispersion change and reduced phonon group velocity.

More recently, in order to elucidate the contribution from phonon coherence and phonon backscattering to the thermal conductivity reduction in Si nanomeshes, Lee et al. fabricated and measured thermal conductivity of Si nanomeshes with periodic and aperiodic pore arrangements (Lee et al. 2017). As the surface-area-to-volume ratio of these two groups of the nanomeshes are kept the same to ensure the same boundary scattering effects, they could isolate the wave-related coherence effects by comparing the measured thermal conductivity of periodic and aperiodic nanomeshes. Shown in **Figure 1.7**, the thermal conductivity of two nanomshes are very close (within 6% measurement uncertainty), and more importantly, the measured data can both be well explained based on the MC ray-tracing simulation combined with Boltzmann Transport Equation

(BTE) particle model. This leads to the conclusion that phonon coherence is unimportant for thermal transport in Si nanomeshes with periodic length larger than 100 nm and at temperatures above 14 K, and phonon backscattering is responsible for the thermal conductivity reduction.

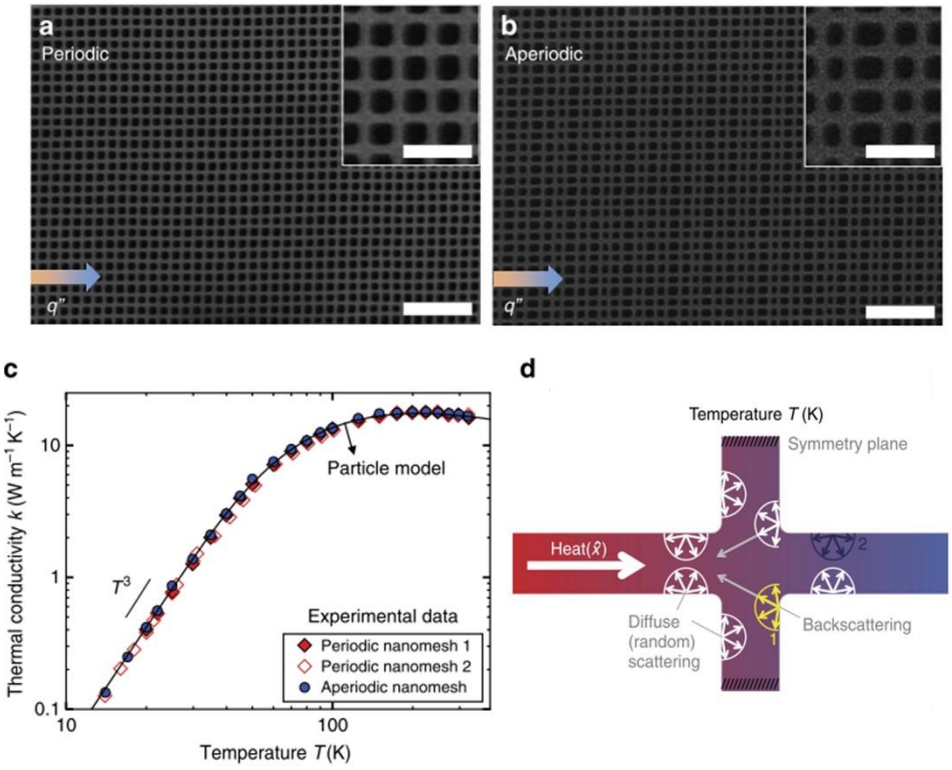

Figure 1.7 (a) SEM image of a periodic Si nanomesh with a controlled periodicity. (b) SEM image of an aperiodic Si nanomesh, in which the pitch in the transport direction varies by up to ±20% (80–120 nm). Scale bars in a,b 200nm (inset) and 600nm (main). (c) Experimental data (points) and the BTE particle model with diffuse surfaces (line) show excellent agreement for κ(T) of two periodic and one aperiodic nanomeshes. (d) Illustration of phonon backscattering for diffuse surfaces (Lee et al. 2017).

In addition to Si nanomeshes with aligned holes, Tang et al. measured thermal conductivity of holey Si thin films with similar porous structure but with staggered holes (Tang et al. 2010). An ultralow thermal conductivity of ~1.7 W/m-K was obtained at room temperature, which was attributed to the necking effect by the authors (Tang et al. 2010). As the neck length of the nanopores is smaller than the phonon MFP, compared with a straight nanowire, phonons travelling in the holey Si would experience more scattering by reflecting from the nanohole sidewalls; and

therefore, it would be trapped and become non-propagating heat carriers. As a result, they concluded that this would create a local negative temperature gradient opposing the linear temperature gradient along a free channel, thus lowering the thermal conductivities of the holy Si thin films (Tang et al. 2010).

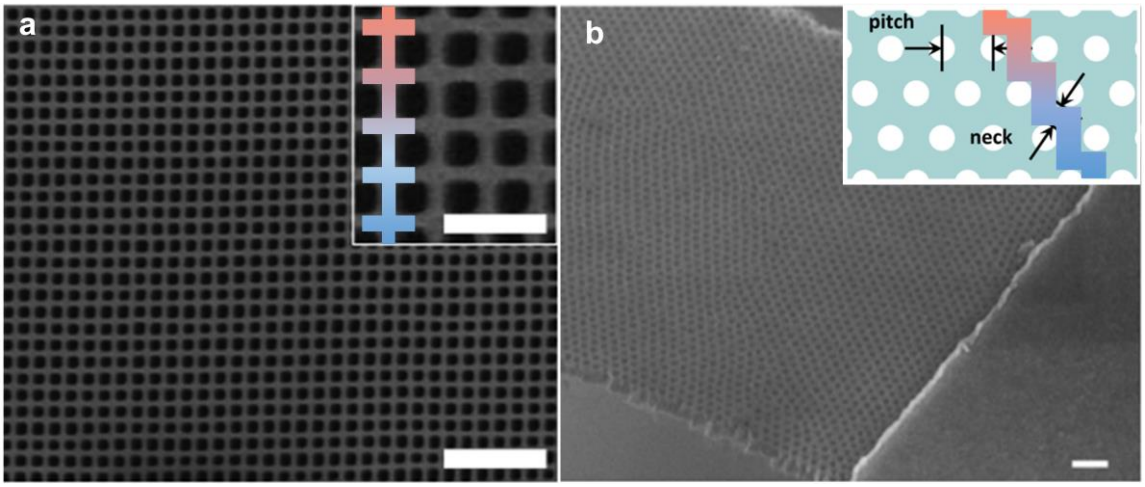

Figure 1.8 (a) SEM image of a periodic Si nanomesh with a controlled periodicity of 100 nm. The inset image shows that the fishbone nanoribbons could be regarded as the building blocks for nanomeshes with aligned hole arrangement. Scale bars are 200nm (inset) and 600nm (main) (Lee et al. 2017). (b) Tilted SEM image shows the holey structure of the nanomesh ribbon, and the inset shows the kinked nanoribbons as the building blocks for nanomeshes with staggered hole arrangement. Scale bar is 200 nm (Lim et al. 2016).

To further unveil the thermal conductivity reduction mechanisms, efforts have been paid to investigate phonon transport in the building blocks of the nanomeshes. Shown as in **Figure 1.8**, the fishbone and kinked nanowires can be regarded as the building blocks of nanomeshes with aligned and staggered square holes, respectively. Si fishbone nanowires were prepared through top-down fabrication with fins attached to a backbone ribbon (Maire & Nomura 2014, Nomura & Maire 2015). Extracting the thermal conductivity using an effective width, it was shown that the thermal conductivity of the fishbone nanoribbon is significantly lower than the corresponding straight nanoribbon, which was attributed to the reduced phonon group velocity in the fishbone wire due to phonon coherence effects and zone folding (Nomura & Maire 2015). However, as

discussed above, phonon coherence requires very strict conditions and its effects have only been observed unambiguously in superlattices with nearly perfect interfaces between the alternating layers (Ravichandran et al. 2013).

Different from the fishbone structures with only two surfaces attached with fins, Termentzidis et al. modeled the thermal conductivity of SiC nanowires with periodic diameter modulations using MD simulations (Termentzidis et al. 2013). Moreover, instead of using an effective width, they extracted the thermal conductivity of a diameter modulated nanowire based on the sections of the smaller diameter. Using this approach, the modeled thermal conductivity is shown to be even ~10% lower than a pristine nanowire with diameter the same as the narrower sections. Besides the phononic band structure change owing to the geometrical modulation, the authors also attributed the lower thermal conductivity to the constriction thermal resistance due to the phonon reflection when the cross-section area reduces (Termentzidis et al. 2013).

Apart from fishbone nanowires, another type of nanowires, e.g. wires with kinks or curvatures, have also been synthesized in controllable manners, and demonstrated for different applications (Jiang et al. 2012, Qing et al. 2014, Tian et al. 2009). The effects of kinks on thermal transport were first studied numerically by Jiang et al. using NEMD through constructing Si nanowires with periodic kinks (Jiang et al. 2013). Their results show that compared with the corresponding straight nanowire, at 300 K, the thermal conductivity could be reduced by more than 20% with a single kink and reaching a maximum reduction of up to ~70% with 11 kinks (Jiang et al. 2013). Detailed MD simulations show that two mechanisms should be responsible for this effect: (1) the interchanging effect between the longitudinal and transverse phonon modes through the kink, and (2) the pinching effect for the twisting and transverse phonon modes at the kink, which comes from the different phonon wave vector directions for the same phonon mode at each side of the

kink. Another numerical study reported by Xiong et al. investigated thermal conductivity of Si nanowires of a twinning superlattice structure with turning angle of 109.4°, leading to a zig-zag configuration with many kinks along the wire (Xiong et al. 2014). Their modeling results yield a similar level of thermal conductivity reduction of up to 65%, and the phonon mode analysis reveals that the minimal thermal conductivity arises due to the disappearance of favored atom polarization directions (Xiong et al. 2014), which is consistent with the physical picture of Jiang et al. (Jiang et al. 2013).

Experimental demonstration of the kink effect on thermal transport only became available very recently. Through systematic experimental measurements of the thermal conductivity of straight and kinked boron carbide nanowires with different diameters and carbon concentrations (Zhang et al. 2017), Zhang et al. found that a single-crystalline, defect-free kink in a boron carbide nanowire could pose a thermal resistance up to ~30 times than that of a straight wire segment of equivalent length, ~7 times more pronounced than that from MD simulation of kinked Si nanowires (Jiang et al. 2013), which eventually led to up to 36% thermal conductivity reduction at 300 K. Based on MC simulation, Zhang et al. attributed this remarkable kink resistance to the combined effects of backscattering of highly focused phonons and required mode conversion at the kink (Zhang et al. 2017). The physical explanation corresponds well with the understanding of phonon transport in holey Si thin films with staggered hole arrangements.

This argument is further supported by the findings that the structural defects in the kink, instead of posing resistance, could actually assist phonon transport through the kink and reduce its resistance as shown in **Figure 1.9**. This counter-intuitive experimental observation is explained by that for boron carbides, the strong elastic anisotropy helps to align phonons along the wire axis; and for the highly focused phonons to enter the opposite leg of a kink, they have to undergo

scatterings to make the turn. As such, more scattering events induced by the defects in the kink will help to change the phonon propagation direction and reduce the kink resistance (Zhang et al. 2017). An important point here is that we could take the advantage of phonon focusing to design materials with desirable properties.

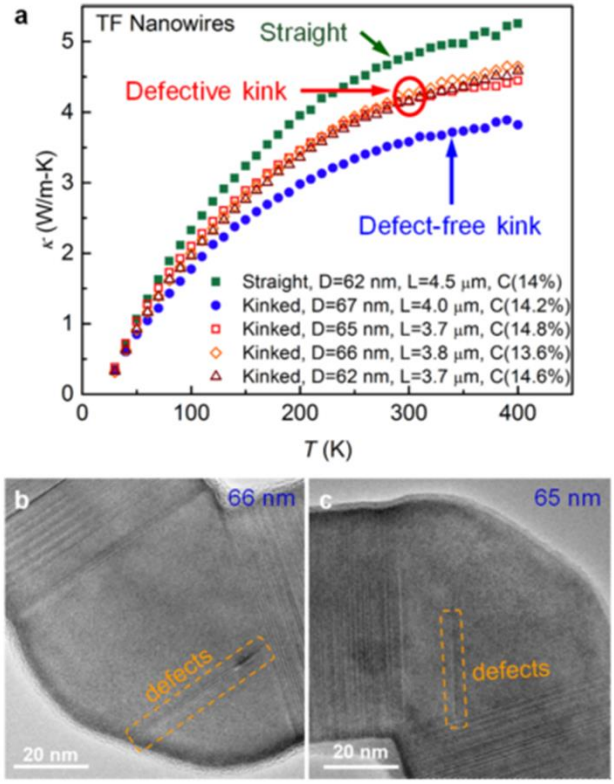

Figure 1.9 (a) Thermal conductivity of boron carbide nanowires that are straight, with defect-free kinks, and with defective kinks, respectively. (b,c) TEM images show the defects in the kinks of kinked boron carbide nanowires (Zhang et al. 2017).

1.5 Dimensional Crossover

In the literature, nanowires are often referred to as one-dimensional (1D); however, in most cases this designation is purely from a geometric consideration, but not in the physical sense since phonons with wave vectors along all directions are excited. As such, at what diameter true physical dimensionality transition occurs and the consequence of this transition on thermal conductivity is

an interesting question. In fact, the divergent thermal conductivity of truly momentum-conserved 1D system is a classical problem in physics (Li & Wang 2003, Zaslavsky 2002). Even though no solid experimental observation of thermal transport in truly physically 1D nanowires has been reported, theoretical efforts over the past several decades have demonstrated intriguing thermal transport behavior in ultra-thin nanowires.

Early mathematical models considering 1D periodic lattices of point-like atoms interacting with their neighbors through non-linear forces, such as 1D Fermi-Pasta-Ulam and diatomic Toda lattices, have shown a diverging thermal conductivity as the chain length increases, also known as superdiffusive thermal transport (Crnjar et al. 2018, Lepri et al. 2003). However, these simplified models are based on relatively simple interatomic potentials; and recently, efforts have been made to accurately describe the interatomic interactions through calculating the realistic force fields. As such, atomistic simulations have been conducted on various 1D materials, such as carbon nanotubes (Liu et al. 2012, Zhang & Li 2005), polymer chains (Crnjar et al. 2018, Henry & Chen 2008), and thin silicon nanowires (Donadio & Galli 2010, Ponomareva et al. 2007, Zhou et al. 2017).

Carbon nanotubes (CNTs) are one of the promising nanomaterials coming to the spotlight of research after being discovered in the 1990s (Iijima 1991). In addition to the electronic and optical properties, thermal transport in CNTs has also attracted tremendous attention (Kim et al. 2001, Yang et al. 2014). Although electrons could also serve as heat carriers, it has been demonstrated that even for metallic nanotubes, electrons give limited contribution to thermal transport in SWCNTs (Yamamoto et al. 2004), which makes the SWCNTs ideally suitable for MD investigations to understand heat conduction in low dimensional systems. Using MD simulations, Zhang and Li found that the modeled thermal conductivity of SWCNT diverged with the length of

the system as $\kappa \sim L^{\beta}$, where the exponent β depends on the temperature and SWCNT diameter (Zhang & Li 2005). The authors further performed energy diffusion simulation along SWCNTs to understand the physical mechanism of the observed length dependent thermal conductivity. The results showed that at low temperatures, as the atomic vibrations are very small, the Tersoff potential can be approximated by a harmonic one, and phonons transport ballistically. However, with increasing temperature, the anharmonic terms become significant, which eventually results in superdiffusive phonon transport (Liu et al. 2012, Zhang & Li 2005).

In addition to CNT, Si nanowire is another material system that have been theoretically investigated for the divergent thermal conductivity. For example, using NEMD, Ponomareva et al. showed that the modeled thermal conductivity of Si nanowires reduces as the diameter decreases from 7.7 to 3.4 nm because of the enhanced surface scattering of phonons (Ponomareva et al. 2007). However, as the wire diameter further reduces, the thermal conductivity starts to increase rapidly. This is explained by the phonon confinement effect. It will shift the excited longest wavelength phonons to higher frequency, resulting in a larger amount of energy carried by the longer wavelength phonons and an increase in the thermal conductivity for small sized nanowires (Ponomareva et al. 2007). More recently, Zhou et al. performed systematic EMD simulations of Si nanowires using all Tersoff, environmental-dependent interatomic potential (EDIP) and Stillinger-Webber (SW) interatomic potentials (Zhou et al. 2017). Their results suggest that for nanowires with diameters smaller than ~2 nm, thermal conductivity increases rapidly with decreasing diameter and can reach a value that is more than ten-fold of the bulk value as the nanowire diameter becomes smaller than 1 nm (Zhou et al. 2017). Detailed analysis shows that as the nanowire diameter drops below 2 nm, the phonon dispersion alters significantly with enlarged energy gaps between the acoustic and optical branches (Zhou et al. 2017). This leads to drastically

lower Umklapp scattering rate and most scattering events are momentum-conserved normal scattering process. However, the authors concluded that the residue Umklapp scattering would result in converged thermal conductivity.

In a separate effort, Yang et al. studied length dependent thermal conductivity of a ~1.6 nm diameter Si nanowire using NEMD simulations (Yang et al. 2010). It was found that the modeled thermal conductivity diverges with the length as $\kappa \sim L^{\beta}$ at 300 K, but their results show that the length dependence of the thermal conductivity is different in different length regimes. Specifically, the thermal conductivity increases linearly with the length ($\beta \sim 1$) for $L < 60$ nm, as L further increases, the divergent exponent β reduces to 0.27. This is because for nanowire with length shorter than the phonon MFP, the interactions among phonons are weak, and phonons transport ballistically, like in harmonic lattice. However, as the length increases to be larger than the phonon MFP, phonon-phonon scattering becomes significant (Yang et al. 2010). Their results are consistent with previous theoretical model for 1D lattice with strong phonon couplings in the system, where the thermal conductivity diverges with wire length as $\kappa \sim L^{0.33}$ (Wang & Li 2004).

In summary, while extensive theoretical analyses and numerical modeling have been done on thermal transport of physically 1D systems, direct experimental observation of the thermal behavior during the dimensionality transition process is still lacking and it will be very exciting to see direct experimental evidence of material thermal behavior during this process.

1.6 Summary

In the past two decades, motivated by the potential technological applications and fundamental scientific interest, extensive studies on thermal transport through various kinds of nanowires have been carried out, which has led to significant advance in our understanding on phonon dynamics at surface and interfaces as well as thermal transport through nanostructures.

Classically, phonon boundary scattering is shown to cause a dramatic thermal conductivity reduction compared with their bulk counterparts. Through synthesizing thin nanowires/nanotubes with characteristic size below 20 nm, novel size effects beyond the phonon boundary scattering have been observed to further reduce the thermal conductivity. Meanwhile, morphology engineering, such as rough nanowires, nanomeshes as well as fishbone and kinked nanowires, is also shown to be effective to tune the thermal conductivity.

However, although ultra-low thermal conductivity values have been achieved in various nanostructures, the underlying thermal conductivity reduction mechanisms have not been fully understood. For example, it still remains unclear whether phonon boundary scattering can solely account for the reduced thermal conductivity in Si nanostructures with a characteristic dimension of 20 nm or less, and how free surfaces and van der Waals interfaces affect phonon transport differently in Si nanostructures. Moreover, while significant progress has been achieved on quantitative understanding of the other phonon scattering mechanisms, the role of electron-phonon scattering remains largely less well-understood, mainly due to the lack of direct experimental evidence.

In the following chapters, we employed a well-established suspended micro-bridge method to extract the thermal transport properties of individual Si nanoribbons and double Si nanoribbons with composite van der Waals interface. We also measured thermal and electrical conductivity of the same $NbSe_3$ nanowire to study the effects of electron-phonon scattering on phonon transport. The dissertation is organized as follows.

In chapter 2, we discussed the implementation of the micro-bridge method with enhanced measurement sensitivity and discussed the effects of several different factors on the measurement results. The sample preparation and measurement mechanisms will also be covered.

Using the measurement setup, and taking the advantage of three-point bending test with atomic force microscopy (AFM), chapter 3 details the thermal conductivity and elastic property measurements on two groups of Si nanoribbons with thickness of either ~30 nm or 20 nm. Results show that while the measured thermal conductivity for the ~30 nm thick ribbons can be well explained by the classical size effect, the thermal conductivities for the ~20 nm thick ribbons deviate from the prediction remarkably, and size effects beyond phonon boundary scattering must be considered.

In chapter 4, we prepared and measured double silicon nanoribbons bonded via van der Waals interactions and with a layer of amorphous silicon dioxide (a-SiO_2) sandwiched in-between, the results show that thermal conductivity of the ribbon bundle can indeed be higher than that of the corresponding single ribbons, indicating that thermal phonons can ballistically transmit through the composite van der Waals interfaces with a thin a-SiO_2 layer. For an annealed double ribbon sample with high interfacial adhesion energy and an oxide thickness of ~5.1 nm, we observed ~11% thermal conductivity enhancement at 300 K, indicating that thermal phonons can ballistically penetrate through an a-SiO_2 layer of more than 5 nm.

In chapter 5, by taking advantage of the unique features of charge density waves, we demonstrate the effects of electron-phonon scattering on the lattice thermal conductivity of the quasi-one-dimensional van der Waals crystal $NbSe_3$ nanowires. The variation of charge carrier concentration upon the onset of charge density waves results in distinct signatures in the extracted lattice thermal conductivity, which cannot be recaptured without considering electron-phonon scattering.

Chapter 6 provides a summary of the key conclusions from this dissertation.

Chapter 2

Sample Preparation and Experimental Setup

Over the past two decades, various techniques have been developed to measure the thermal properties of individual one-dimensional nanostructures, including the commonly used suspended micro-bridge approach based on the microfabricated devices (Li et al. 2003b, Shi et al. 2003), and its variations (Boukai et al. 2008, Bui et al. 2012), as well as the joule heating method (Lu et al. 2001, Pop et al. 2006). As the joule heating method is applicable only for electrically conducting materials, the suspended microdevice-based thermal-bridge method is more commonly used. This suspended microdevice was pioneered by Kim et al. (Kim et al. 2001) and Shi et al. (Shi et al. 2003) for measuring thermal conductivity as well as thermoelectric properties of individual carbon nanotubes, which was also used by Li et al. for the thermal conductivity measurements of Si nanowires (Li et al. 2003b).

Later, this suspended platform has been successfully applied to study the thermal transport properties of various other individual one-dimensional nanostructures, such as polymer nanofibers (Ma et al. 2015, Zhong et al. 2014), molecular chains (Kodama et al. 2009), single- and multi-walled carbon nanotubes (Yang et al. 2011a, Yu et al. 2005), contacts and interfaces between individual nanostructures (Yang et al. 2011b, 2014), and more recently, Chang et al. (Chang et al. 2007, Lee et al. 2013) further extended the capability of this suspended platform to study phonon transport in nanowires under strain/buckling. These studies not only advance our understanding of the fundamental physics on energy transport in highly confined nanostructures, but have also shown broad implications for thermal management of nanoelectronic circuits, thermoelectric power generation as well as the design of thermal interface materials.

The conventional, 4-point measurement scheme of the suspended platform is limited to a noise equivalent thermal conductance of ~300 pW/K, as demonstrated by Shi et al. (Shi et al. 2003). There are two major noise sources for the conventional measurement scheme: one is the radiation dominated background thermal conductance, and the other is the temperature fluctuation of the sample holder in the cryostat (~100 mK). In order to overcome the latter limitation, Wingert et al. recently developed a new measurement scheme with detectable thermal conductance down to 10 pW/K (Wingert et al. 2012). This is achieved through introducing a Wheatstone bridge set-up using a reference device at the sensing side in the measurement platform. As the reference device is also placed on the sample holder in the cryostat, it experiences the same temperature fluctuations with the measurement device. Thus, through common mode rejection, the effects of sample holder temperature fluctuation, one of the major noise source in the 4-point measurement scheme, can be effectively canceled out. Herein, we successfully incorporate this scheme into our measurement setup and this chapter mainly focuses on the implementation of our experimental approach.

2.1 Measurement Devices

As shown in **Figure 2.1**, the measurement device consists of two adjacent thermally isolated low stress silicon nitride (SiNx) membranes (18.2 μm × 27.1 μm), which are supported by six 0.5 μm thick, 416 μm long and 2.2 μm wide SiNx beams. A 30 nm thick and 500 nm wide platinum resistance thermometer (PRT) thin film serpentine is patterned on each SiNx membranes, which also serves as a microheater by joule heating. To prevent the electrically conductive samples from shorting the heater coils and hence disturbing the measurement circuits, a layer of 200 nm thick low temperature silicon oxide (LTO) is deposited to cover the serpentine Pt lines. The PRT is connected with 1.2 μm wide Pt leads on the long SiNx beams to 400 μm × 500 μm platinum contact pads located on the substrate, allowing for four-probe measurement of resistance of the

PRT. For simultaneous measurements of electrical transport properties, one or two additional platinum electrodes can be patterned on each membrane, facilitating characterizations of electrical conductivities and Seebeck coefficients of the samples. In addition, the substrate can be etched away, allowing for transmission electron microscopy (TEM) characterization of the nanostructure sample assembled on the membranes.

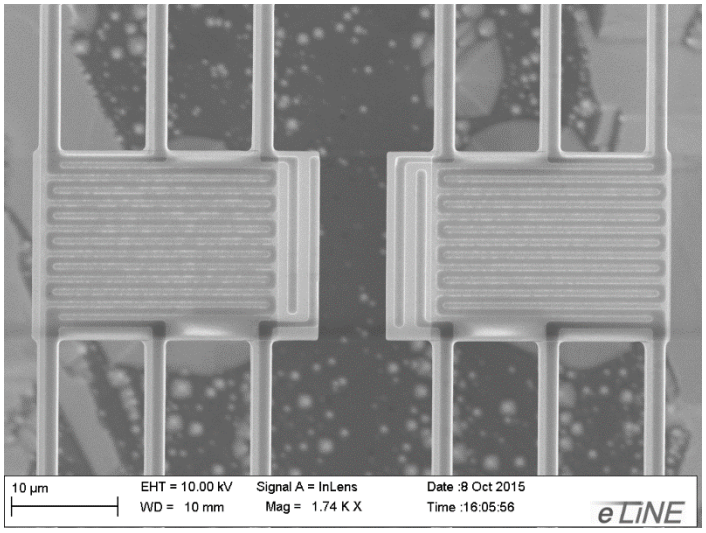

Figure 2.1 An SEM micrograph of the suspended microdevice with electrodes and integrated microheaters/thermometers made from Pt lines.

2.2 Sample Preparation

2.2.1 Sample Fabrication Using Top-down Approach

One key issue in the study and application of nanowires is how to assemble individual atoms into such a unique 1D nanostructure in an effective and controllable way. A range of routes to nanowire production have opened up over the past several decades as a result of advances in nanowire fabrication techniques. These nanowire fabrication routes can usually be categorized into two paradigms, bottom-up or top-down. The vapor-liquid-solid (VLS) mechanism (Hobbs et al. 2012), and its analogues (Cheze et al. 2010, Heitsch et al. 2008, Holmes et al. 2000), is the most

commonly used bottom-up method for nanowire production. The VLS method relies on a vapor phase precursor of the nanowire material, which is absorbed by a liquid phase seed particle, from which the unidirectional nanowire growth proceeds. The choice of an appropriate seed material has the benefit of allowing control over the diameters of the nanowires produced, while the seed material can also significantly affect the crystalline quality of the nanowire. The benefits of bottom-up approach over top-down processing are that it can provide high density of nanowires with high crystalline quality (Hobbs et al. 2012). However, unlike the top-down method, the bottom-up approach is usually difficult to achieve excellent control over the placement and feature size of the nanowire samples. As such, to produce nanowires with irregular shape and complex morphologies, such as kinked and fishbone nanoribbons, it is more desirable to adopt the top-down nanofabrication method.

In this dissertation, all of the Si nanostructures are fabricated using the electron beam lithography (EBL) technique, one of the most widely adopted top-down fabrication method. The fabrication starts with a 6″ (150 mm) diameter SOI wafers (p-type boron doped Si (100) with a dopant density of $0.7–1.5\times10^{15}$ cm^{-3}, Simgui Technology Co., Ltd.) with a 140 nm thick top silicon device layer and a 500 nm buried oxide (BOX) layer. In the fabrication process, the SOI wafer first went through a timed dry oxidation process to oxidize a targeted thickness of the device silicon layer, after which the resulted silicon oxide layer was removed with buffered oxide etch (BOE 6:1). The thickness of the remaining silicon device layer was measured with an ellipsometry method. Then, the wafer was cut into 30×30 mm pieces for subsequent patterning processes.

For straight Si nanoribbon fabrication, the SOI wafer piece was first spin-coated a PMMA thin layer, which was then patterned through electron beam lithography. After developing, a layer of Cr thin film was coated onto the PMMA layer through thermal evaporation (Angstrom Resistive

Evaporator). The lift-off process was applied to transfer the pattern from PMMA layer to Cr, which was subsequently served as a hard mask for the reactive-ion-etching (RIE, Oxford PlasmaPro) process. After Si etching, we first remove the Cr mask using Cr etchant (Transene Company, Inc.), and the Si nanoribbons are thus anchored on two separated Si islands. Finally, wet buffered oxide etching (Sigma Aldrich, 6.38% HF) was used to remove the underneath BOX and release the ribbons into freestanding structures, as shown in **Figure 2.2**.

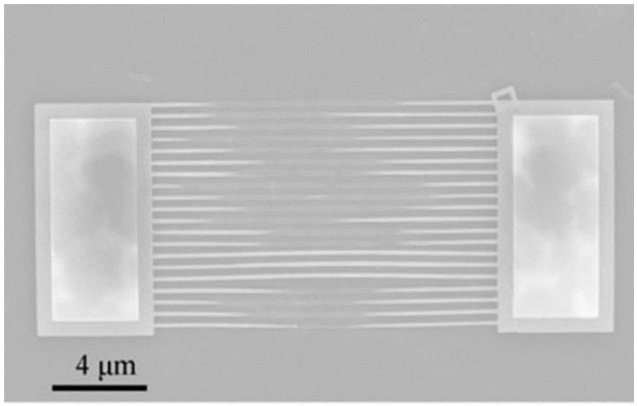

Figure 2.2 A SEM micrograph showing the as-fabricated straight Si nanoribbons.

However, in order to pattern Si nanoribbons with more complex surface morphologies, such as fishbone or kinked structures, we need to pay more attention in the electron beam lithography process. For nanostructures with tightly arranged features of widely varying sizes, the proximity effect can cause particularly strong interference in electron beams. During an exposure, beam broadening due to electron scattering in the material causes both overexposure and underexposure of individual nanostructures, especially when high accelerating voltages (> 10 keV) are involved.

Figure 2.3 shows the electron scattering process within a sample. When the primary electrons penetrate the resist, they are scattered forward (FE) due to interactions with the resist electrons, which causes the first beam broadening. After the electrons penetrate to the substrate below it,

some of them will be scattered back from the lattice atoms of the substrate, broadening the beam again. These backscattered electrons (BE) are responsible for most of the proximity effect.

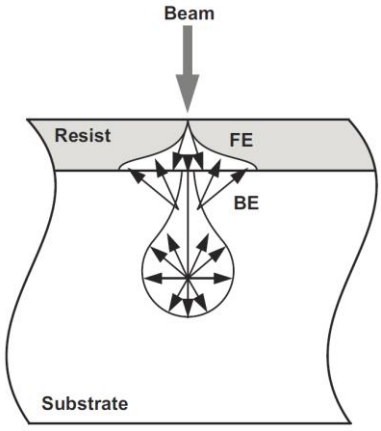

Figure 2.3 Scattering process during electron beam exposure of a sample (Raith Software 2008).

For example, if we want to pattern a structure with surface configuration shown in **Figure 2.4a**, and the dose distribution is set to be uniform over the entire structure, owing to the interference of primary and backscattered electrons, two types of proximity effects, namely the inter-shape and intra-shape proximity, would occur (Chang 1975). The intra-shape proximity arises at the corners of the structures, because less backscattered electrons would cause underexposure. On the other hand, the inter-shape proximity effect arises when the distance between two neighboring structures is below a certain minimum, which causes overexposure due to the mutual exposure of the neighboring elements. As such, the actual energy distribution will deviate from the energy distribution prescribed in the design, and the resulted pattern is shown as **Figure 2.4c**.

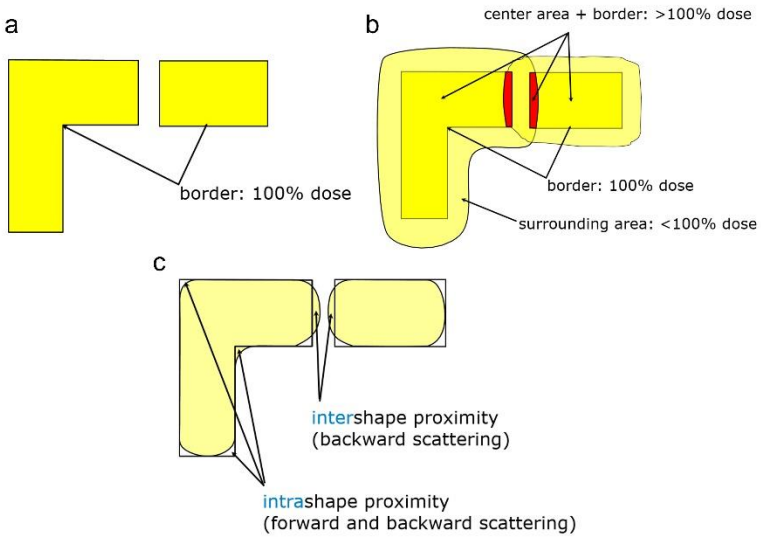

Figure 2.4 Schematic illustration of proximity effect. (a) A assigned pattern with uniform dose distribution. (b) The resulting dose distribution caused by interference effects of forward and backscattered electrons. (c) The resulted pattern caused by the proximity effect (Raith Software 2008).

To cope with this challenge, care should be taken to obtain the optimum patterning parameters. First, to achieve less rounding of corners, e.g. less intra-shape proximity effect, higher accelerating voltage should be adopted (20 KeV). Also, to minimize forward scattering in resist and less beam broadening, thin resist layer should be used (50 nm thick). Finally, to ensure the target energy distribution of a design as precisely as possible to the actual energy requirement of individual structures, we need to perform proximity effect correction (PEC). In order to set the dose factors to individual parts, before the correction, we need to simulate the broadening of the electron beam in the concrete material situation, e.g. by means of a Monte Carlo simulation, and thus to determine the energy distribution deposited along the electron trajectory. Normally, the parameters of a proximity function are obtained by fitting the simulated or measured energy distribution in resist. As the comprehensive parameters needed for correction are stored in a special dataset in NanoPECS^{TM} software, the PEC in this dissertation was carried out by selecting individual

elements in the GDSII editor of the lithography software and applying a corresponding proximity dataset to it (Raith Software 2008).

Figure 2.5a is a fishbone pattern after proximity effect correction, where the color tones indicate an inhomogeneous input energy distribution across the element group. This distribution corresponds to the actual energy requirement: in the blue areas, the energy deposition is lowest due to the large proximity effect between individual elements; while the energy deposition is highest in the red areas at the edge of the element groups, where the intra-shape proximity effect is strongest. Furthermore, the patterns are broken down into many small fracturing shapes shown in **Figure 2.5b**. Zoom-in view in **Figure 2.5c** shows the small fracturing shapes, which would allow for the required energy dose to be assigned as precisely as possible to the actual requirements. To demonstrate the effectiveness of PEC, we collected the SEM micrographs for the PMMA layer after developing, and **Figure 2.5d&e** present the resulted patterns without and with PEC, respectively. Without PEC, as the energy dose at the corners are much smaller than in center, they are largely underexposed, leading to the resulted fishbone close to a straight ribbon without fins attached at the two sides, as shown in **Figure 2.5d**. However, after compensating the proximity effect through PEC, the fins at the two sides receive higher energy dose, which makes the resulted structure closer to our designed pattern as in **Figure 2.5e**. With the pattern successfully transferred to the PMMA layer, the rest of the fabrication processes for the fishbone and kinked Si nanostructures are the same as that of the straight Si ribbons.

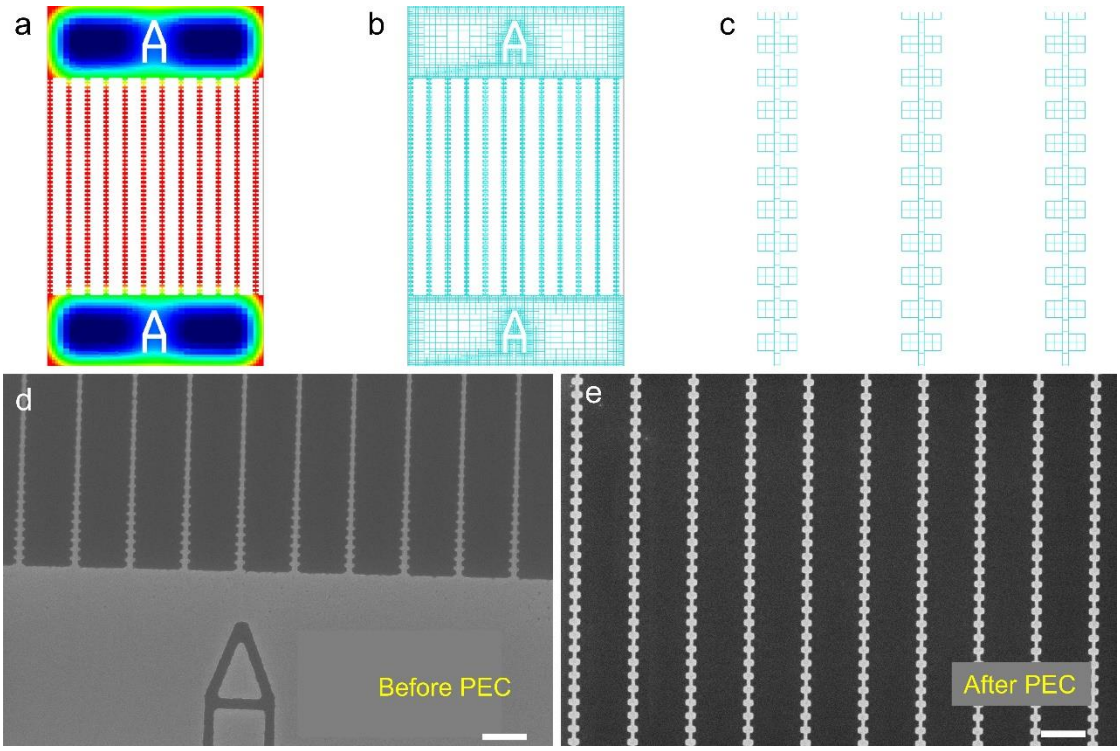

Figure 2.5 Proximity effect correction (PEC). (a) Energy distribution of the fishbone pattern after proximity effect correction using NanoPECS^{TM} software. (b) The fishbone pattern after PEC showing that it is broken into small fracturing shapes. (c) Zoom-in view of the fracturing shapes. SEM micrographs of the PMMA layer after developing, showing the quality of fishbone structures (d) without PEC, and (e) after PEC. Scale bar in (d&e) are 1 μm.

2.2.2 Sample Transfer

Several methods have been developed to place a nanowire across the two suspended membranes of the microheater device. One method involves dispersing the nanowires in a solvent and drop casting the suspension onto a wafer containing many suspended devices. Occasionally, one nanowire would be placed to bridge the two membranes. However, this method requires a nanowire suspension with sufficiently high nanowire density to achieve a good assembly yield. In this dissertation, we used a tungsten probe (The Micromanipulator Co. model 7X) with a tip radius of ~0.1 μm attached to a micromanipulator to manually pick up the nanowire and place it across the device. The whole process is performed under a 100×, long working distance (6.5 mm)

objective lens mounted on a Nikon optical microscope. Shown in **Figure 2.6** is a picture of the home-built micromanipulator stage underneath an optical microscope.

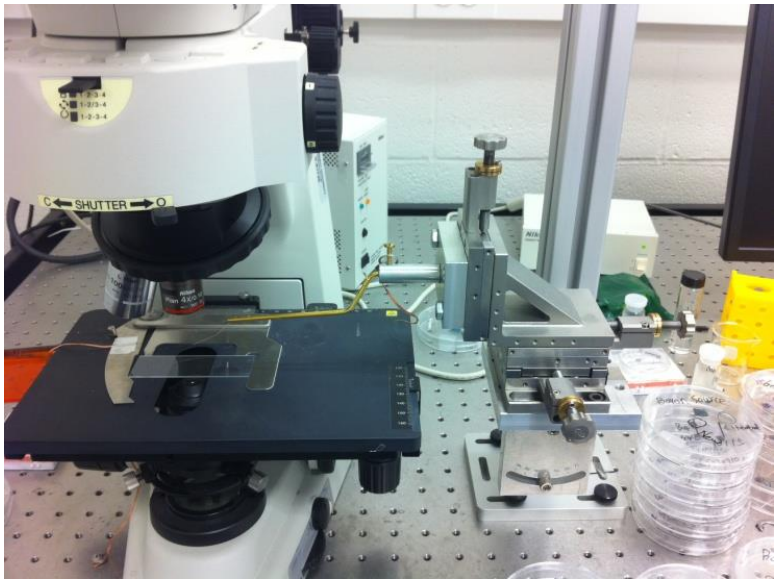

Figure 2.6 A photograph of the in-house assembled micromanipulator with a Nikon microscope (Nikon ECLIPSE 50i) used to place the individual nanowires at desired locations.

Using this method, we first disperse a small amount of samples in solutions, such as reagent alcohol or isopropanol alcohol (IPA), and form a suspension using ultrasonic sonication. A few drops of the suspension are then casted onto a piece of polydimethylsiloxane (PDMS). The PDMS is chosen to be the substrate because of its softness and flexibility, which reduces the risk of damaging the sample as well as the very sharp tip. In addition to drop-casting, PDMS stamping can also be used to transfer the nanostructures.

For Si nanostructures fabricated using the top-down approach as described above, we adopted the stamping process to transfer the samples from the SOI wafer piece to the PDMS surface. As depicted in **Figure 2.7a-b**, using this method, the PDMS stamp is first placed on top of the sample substrate, and the nanostructures on the substrate would adhere to the PDMS surface via van der Waals interaction. During the peeling off process, as the separation energy for the nanostructure-

substrate interface, $G_{substrate}$, is typically a constant, however, owing to the viscoelastic behavior of the elastomer, the adhesion energy between PDMS stamp and the substrate, G_{PDMS}, is strongly dependent on the peel off rates, as shown in **Figure 2.7c** (Meitl et al. 2006). Thus, as the delamination speed increases, G_{PDMS} increases relative to $G_{substrate}$ until the elastomer–nanostructure interface becomes strong enough to break the nanostructure–substrate interface. To ensure a high transfer throughput, a quicker delamination speed is desired, and shown in **Figure 2.7c**, the separation speed of 5 cm/s corresponds to a $G_{PDMS} \sim 4000$ mJ/m^2, which is higher than most of the van der Waals bonding strength.

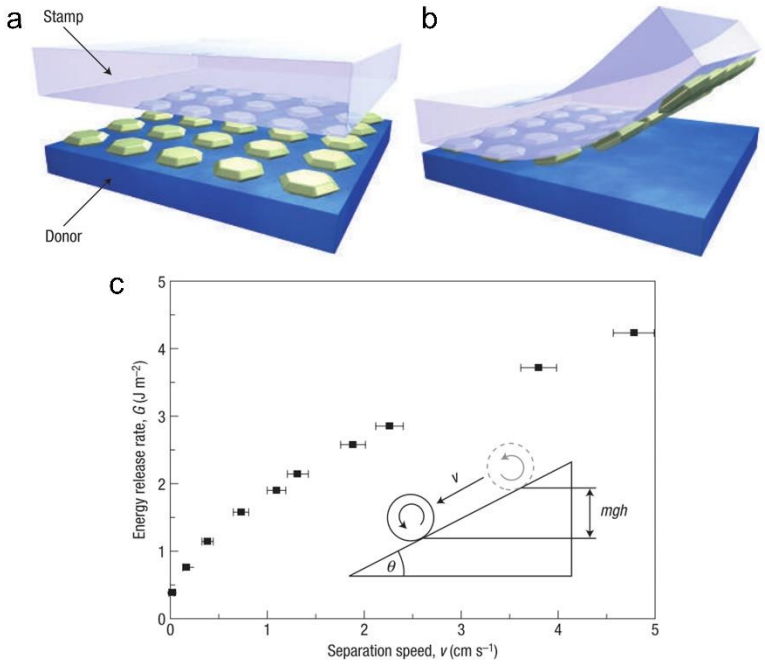

Figure 2.7 Schematic illustration of the generic process flow for transfer printing solid objects. (a) Laminating a stamp against a donor substrate, (b) quickly peel-back stamp and grab objects off of the donor, (c) the adhension enenrgy between the PDMS stamp and the donor substrate (energy release rate) is shown to be strongly dependent on the separation speed (Meitl et al. 2006).

After the samples are transferred to the PDMS substrate, we can use a sharp tungsten probe to pick up a single nanowire and place it between the two suspended membranes. **Figure 2.8a** shows a Si fishbone nanoribbon situated between the two suspended membranes. Compared with

the drop-casting method, sample transfer using a microprobe is cleaner and leaves no solvent residue on the nanowire surface. Moreover, the individual nanostructures transferred using this approach can be placed with desirable locations and orientations. Shown in **Figure 2.8b** is the zoom-in view of this fishbone nanoribbon sample, which exhibits very good structural quality.

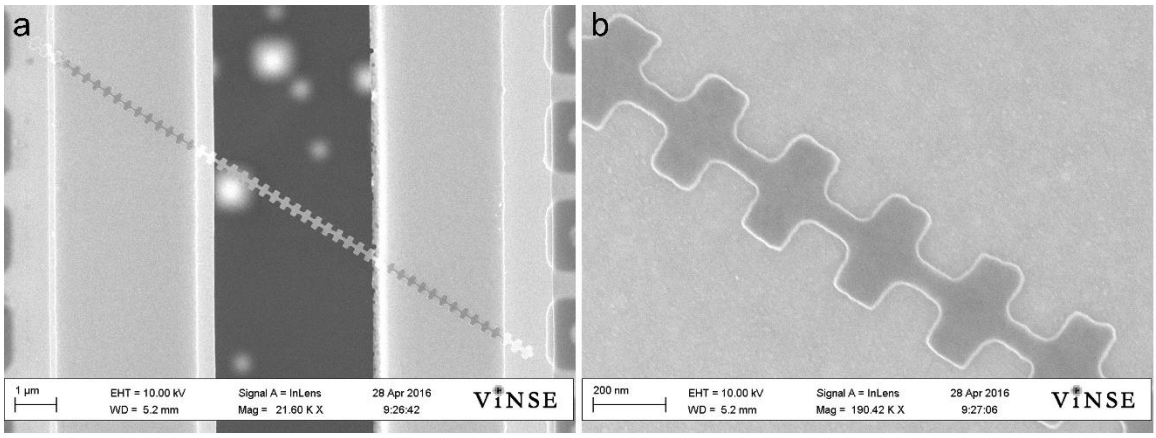

Figure 3.8 (a) An SEM micrograph of a Si fishbone nanoribbon transferred to bridge the two membranes of the microdevice. (b) Zoom-in view showing the quality and edge sharpness of the fabricated Si fishbone nanoribbon, where the backbone width is measured as 67 nm and fin width is 305 nm.

Another challenge in the sample preparation process is to make a good electrical contact between the nanowire and the Pt electrodes, as the presence of native oxide on the surface of a nanowire would prevent direct electric contact. Mavrokefalos et al. (Mavrokefalos et al. 2009) have shown that annealing in a forming gas containing 5% hydrogen in nitrogen was able to reduce the surface oxide of a Bi_2Te_3 nanowires, and the ohmic electrical contact is proved to be established at the nanowire/electrodes contact without any metal deposition. However, this method is ineffective for other materials (Weathers & Shi 2013). Instead, electron beam induced deposition (EBID) of Pt/C composite have been used to form electrical contact for a variety of suspended nanowires (Pettes & Shi 2009, Tham et al. 2006, Zhou et al. 2007). Meanwhile, owing to the increased contact area between the nanowire sample and the Pt electrodes by the metal deposition,

the thermal contact could also be greatly improved. Shown in **Figure 2.9** is a SEM micrograph of a $NbSe_3$ nanowire bridging the four electrodes on the microdevice with local deposition of Pt/C at the contact using EBID.

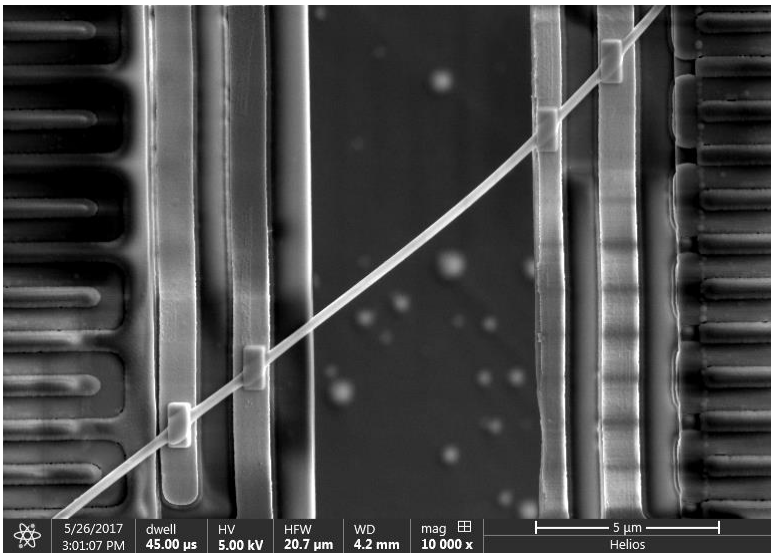

Figure 2.9 A SEM micrograph of a $NbSe_3$ nanowire bridging the four electrodes on the microdevice with local deposition of Pt/C at the contact using EBID.

2.3 Measurement Setup

Figure 2.10 shows the schematic diagram of the experimental setup for measuring the thermal conductance of the sample. During the measurement, the microdevice is placed in a variable-temperature cryostat. The vacuum of the cryostat can achieve a level of less than 10^{-6} mbar using a turbomolecular pump (Edwards E2M1.5). Two lock-in amplifiers (Stanford Research SR850) are used to monitor the voltage change of the PRTs on the heating and sensing membranes, respectively.

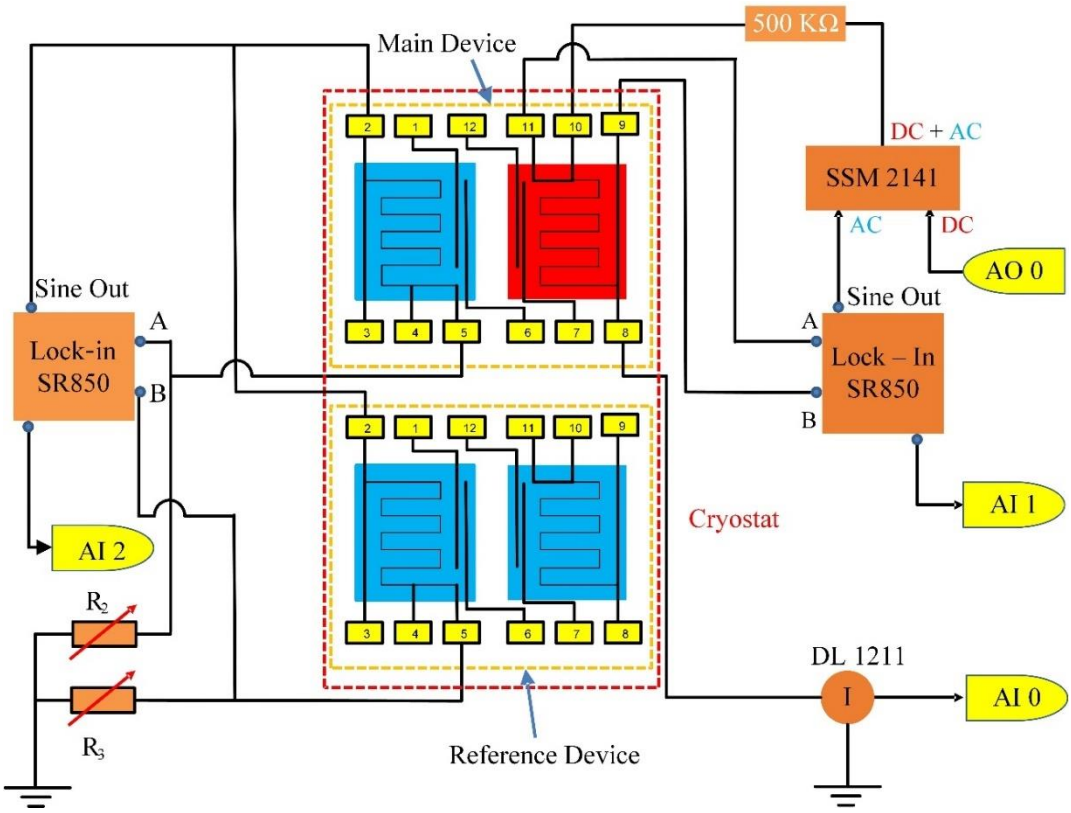

Figure 2.10 Schematic diagram of the common mode measurement setup.

For thermal measurement, a small sinusoidal alternating current (AC) signal i_{ac} from the heating side lock-in amplifier is coupled with a DC heating current source I ($i_{ac} << I$) through an integrated differential amplifier (Analog Devices SSM2141). To achieve a constant current condition under each designated DC heating voltage, the coupled current source is connected with a large resistor (505 KΩ) in series before reaching the heating side thermometer R_h. During the measurement, a sweeping DC current is applied to the platinum coil on heating membrane to generate Joule heating, and the temperature rise of the two SiNx membranes are monitored accordingly. The temperature change induces resistance change for both the PRTs on heating and sensing side (R_h and R_s), which leads to changes on the AC output voltages that are measured by the lock-in amplifier using the 4-point method. The output of the lock-in amplifier is fed into a

data acquisition (DAQ) board (National Instruments PCI-6052e). Meanwhile, at the heating side, the DC heating current is measured by a high accuracy current preamplifier (DL Instruments Model 1211).

To implement the Wheatstone bridge circuit, the sensing side thermometer R_s is connected with an on-chip reference Pt resistor $R_{s,ref}$. $R_{s,ref}$ is situated right aside of the measurement device (<5 mm) to minimize the effects of variation in ambient temperature over the area of the chip. Then, both R_s and $R_{s,ref}$ are connected with two precision resistor R_2 and R_3 (Extech 3804400) sitting in ambient environment, which can be tuned to balance the bridge.

Figure 2.11 shows the thermal circuit of the measurement setup. When a DC current I passes through the PRT on the heating membrane, it produces certain amount of Joule heat, $Q_h = I^2R_h$. The PRT on each membrane is connected to the contact pads by four Pt leads, allowing for 4-point resistance measurement. The resistance of each Pt lead is R_L, which is about the same as R_h. Thus, a Joule heat of $2Q_L = 2I^2R_L$ is dissipated in the two Pt leads that supply the DC current to the heating PRT.

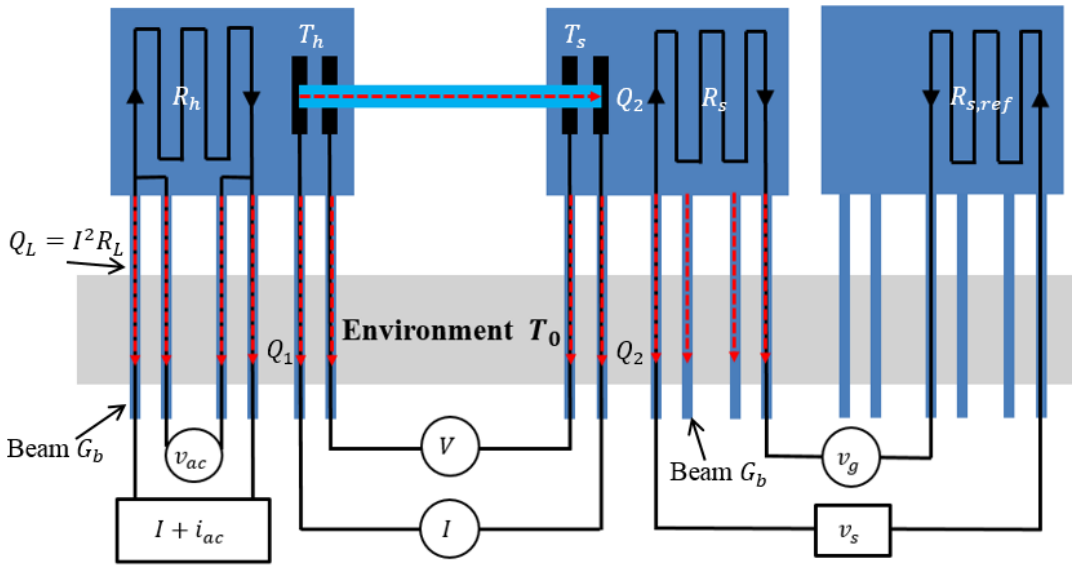

Figure 2.11 The thermal circuit of the common mode measurement setup.

We assume that the temperature of the heating membrane is raised to a uniform temperature T_h. This assumption can be justified because the internal thermal resistance of the membrane is much smaller than that of the long narrow beams thermally connecting the membranes to the silicon chip at temperature T_0, as verified by the finite element analysis by Moore et al. (Moore & Shi 2010). A certain amount of heat Q_2 is conducted through the sample from the heating membrane to the sensing side, raising the temperature of the latter to T_s. In high vacuum with a small ΔT_h ($\equiv T_h - T_0 < 5K$), the heat transfer between the two membranes by air conduction and radiation is negligible compared to Q_2, as discussed below. The heat transferred to the sensing side, Q_2, is eventually dissipated to the substrate (silicon chip) through six beams supporting the sensing membrane, while the rest of the heat i.e. $Q_1 = Q_h + 2Q_L - Q_2$, is conducted to the environment through other six beams on the heating side.

The six supporting beams on each side are designed to be identical. If the radiation and residual air molecules conduction/convection heat loss from the membranes and the six supporting beams to the environment are negligible compared to the conduction heat transfer through six beams, the total thermal conductance of the six suspending beams can be written as $G_b = 6k_lA/L$, where k_l, A, and L are the thermal conductivity, cross sectional area, and length of each beam, respectively. We can then obtain the following equation from the thermal resistance circuit shown in **Figure. 2.11**:

$$Q_2 = G_b(T_s - T_0) = G_s(T_h - T_s), \tag{2.1}$$

where G_s is the sample thermal conductance. The inverse of G_s, that is, R_s, consists of both the intrinsic thermal resistance of the sample R_i and the contact thermal resistance between the sample and the Pt electrodes R_c, which is

$$R_s = R_i + R_c. \tag{2.2}$$

Here, R_i can be expressed as $R_i = L_n/A_n k_n$, k_n, A_n and L_n are the thermal conductivity, cross sectional area, and the suspended length between the two membranes of the nanowire sample, respectively. R_c is the contact thermal resistance at the sample/Pt electrodes interface. Because the temperature rise ΔT_h is carefully controlled to be small (~5 K), G_s, G_b and G_c are assumed to be constant as the heating current is ramped up.

Based on the thermal resistance circuit, G_b and G_s can be further expressed as a function of ΔT_h and ΔT_s ($\equiv T_s - T_0$), Q_h, and Q_L,

$$G_b = \frac{Q_h + Q_L}{\Delta T_h + \Delta T_s}, \tag{2.3}$$

and

$$G_s = G_b \frac{\Delta T_s}{\Delta T_h - \Delta T_s}, \tag{2.4}$$

where Q_h and Q_L can be calculated from the current and voltage drops across the heating side PRT and Pt leads. ΔT_h and ΔT_s are derived from the measured resistance change of the two PRTs during heating and their temperature coefficients of resistance (TCR = (d$R(I=0)$/dT)/R).

The temperature rise of the sensing membrane, ΔT_s, is obtained from the Wheatstone bridge output voltage change. As shown in **Figure 2.12**, the bridge circuit consists of sensing side resistor R_s of the measurement device, a reference device resistor $R_{s,ref}$ and two additional precision resistors, R_2 and R_3, connected in parallel. The sensing side lock-in amplifier measures the bridge output voltage v_g, defined as the voltage difference between the two branches, v_A and v_B respectively:

$$v_g = v_A - v_B = \left(\frac{R_2}{R_s + R_2} - \frac{R_3}{R_{s,ref} + R_3} \right) v_s . \tag{2.5}$$

Eqn. (2.5) can be rearranged to calculate the R_s as a function of the output voltage, where all of the other parameters are known:

$$R_s = \frac{R_2}{\frac{v_g}{v_s} + \frac{R_3}{R_1 + R_3}} - R_2 \,. \tag{2.6}$$

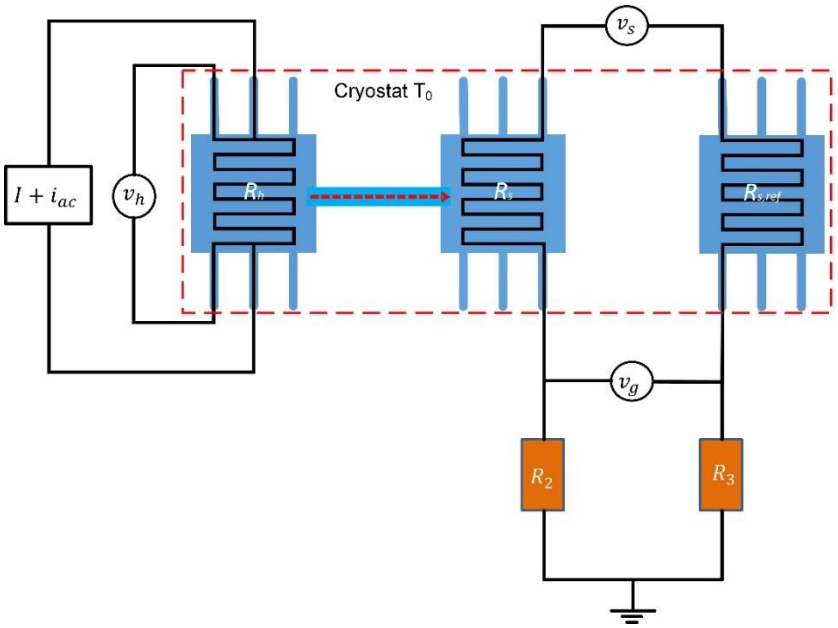

Figure 2.12 The simplified electrical measurement circuit (the Wheatstone bridge circuit).

However, from Eqn. (2.6), the calculated electrical resistance is the total resistance of the sensing side resistor, which includes the resistance of the sensing side PRT, R_c as well as the resistance of two supporting beams, $2R_b$. The temperature is uniform over the sensing side membrane (T_s) but varies linearly from T_s to the ambient temperature T_0 along the two supporting beams. As such, the sensing side total electrical resistance can be expressed as

$$R_s + \Delta R_s = 2\left[R_b + \frac{dR_b}{dT}\left(\frac{T_s - T_0}{2}\right)\right] + R_c + \frac{dR_c}{dT}(T_s - T_0)\,, \tag{2.7}$$

where ΔR_s is solely due to the temperature change:

$$\Delta R_s = \left(\frac{dR_b}{dT} + \frac{dR_c}{dT} \right) (T_s - T_0) . \tag{2.8}$$

Therefore, the sensing side electrical resistance change can be regarded as a uniform temperature change over the membrane as well as along the length of a single beam. From this, we are able to define an effective change in resistance per temperature difference, which is found to be

$$\frac{dR_{s,eff}}{dT} = \frac{dR_s}{dT} \times \frac{R_b + R_c}{2R_b + R_c} . \tag{2.9}$$

Therefore, similar to the heating side, the temperature rise of the sensing side resistor can be calculated as

$$\Delta T_s = \frac{\Delta R_s}{\frac{dR_{s,eff}}{dT}} . \tag{2.10}$$

In order to measure additional thermoelectric parameters, (i.e. electrical conductivity and Seebeck coefficient) of the nanowires, as mentioned above, a layer of Pt/C composite can be deposited through EBID on top of the sample-electrode contact to reinforce the electrical contact. For nanowires with a thin layer of native oxide on the surface, prior to EBID, the electrical contact is enabled by using electron beam induced etching (EBIE) to remove the oxide layer. For amorphous sheath that cannot be taken away by EBIE, focused ion beam (FIB) could be used to do the locally etching. However, special care should be taken when performing the ion milling, as it will also destroy the measured nanowire sample when not properly protected. Alternatively, BCl_3 plasma etching could be used for native oxide removal to enable the electrical contact (Weathers & Shi 2013).

The electrical resistance of the nanowire sample is measured by the four-probe method. However, for samples of very large electrical resistance (>1 MΩ), as the input impedance of SR560 is around 100 MΩ, the non-negligible current passing through the voltage amplifier results in the measured resistance to be lower than its actual value. To cope with this challenge, we applied an instrumentation amplifier of extremely large input impedance (>1 GΩ) before the voltage amplifier (SR560) (Werheit et al. 2009).

The Seebeck coefficient can be measured from the temperature difference of the two membranes and the induced voltage difference across the two inner electrodes contacting the nanowire sample, i.e., $V_{TE}=(S_s-S_{Pt})(T_h-T_s)$ (Mavrokefalos et al. 2007, Poudel et al. 2008, Werheit et al. 2009). During the Seebeck coefficient measurement, the relay is closed to avoid the unwanted heating of the devices caused by the small current for electrical resistance measurement, shown in **Figure 2.13**.

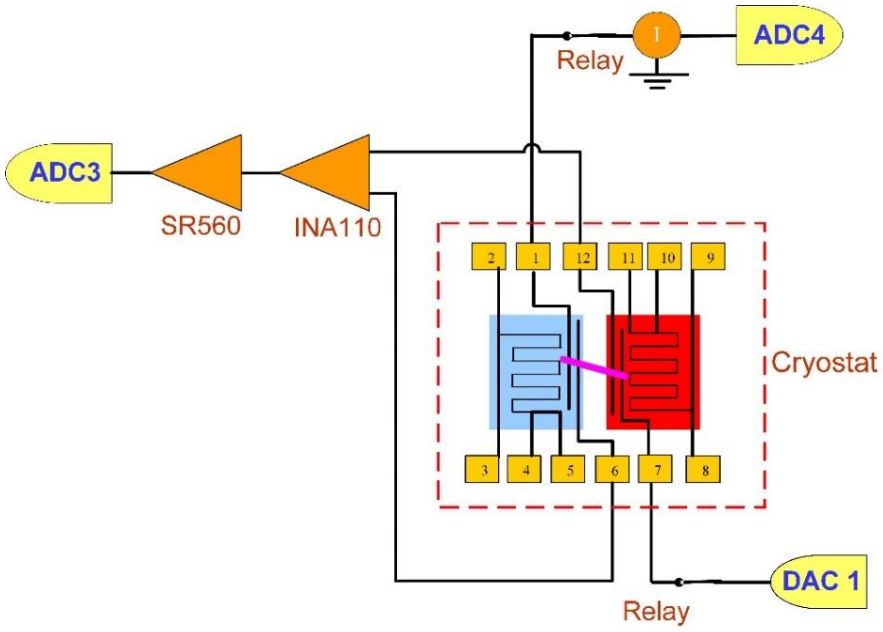

Figure 2.13 Illustration of the additional Seebeck and four-probe electrical resistance measurement setup when the circuit is connected (Relay closed).

2.3.1 Effects of Radiation Shields

In our heat transfer model of the experimental set-up, we consider that all dissipated Joule heat is conducted to the substrate through the supporting beams, while the radiation heat transfer is assumed to be negligible. This assumption is examined by Moore et al. through finite element analysis to model the temperature distribution considering the radiation heat transfer between the device and the surrounding environment (Moore & Shi 2010). They found that owing to the radiation heat transfer, temperature profiles along the long supporting beams becomes non-linear, and the membrane temperatures are significantly different from the sample stage temperature when the global temperature is considerably higher/lower than the room temperature. Detailed analysis shows that this difference could be tens of kelvin at 800 K. Even though it does not necessarily cause incorrect measurements, the non-linearity will cause errors in the measured temperature coefficient of resistance (TCR) of the thermometers, which eventually propagate into the extracted thermal conductance of the beams and samples (Moore & Shi 2010). However, they suggest that this significant radiation heat loss could be minimized with an additional radiation shield mounted directly onto the sample stage, which ideally shares the same temperature of sample holder, and the effects of the radiation heat transfer from the measurement device to the outer environment is also experimentally observed by other groups (Lee et al. 2016b, Zheng et al. 2013).

For our measurement setup (Janis, CCS 400), the temperature of the sample holder is controlled by a Lakeshore 335 temperature controller. The temperature sensor used for this control locates at the heat station, as shown in **Figure 2.14a**. Because the microdevice used for thermal conductivity measurements is glued on a double in-line package (DIP), and the DIP has a distance away from the location of the temperature sensor in the temperature control loop, which may result in the device temperature deviating from the set temperature. As such, to rigorously determine the

device temperature and also to confirm the effectiveness of the additional radiation shield, we measured the local temperature of the DIP with and without the inner radiation shield, and compared it with the setting temperature of the temperature controller. Shown as in **Figure 2.14b**, the local temperature of DIP is measured by a calibrated silicon diode sensor (Janis DT-670B-CU-HT) with accuracy of ±0.1 K, and it is mounted onto the DIP by the copper tape.

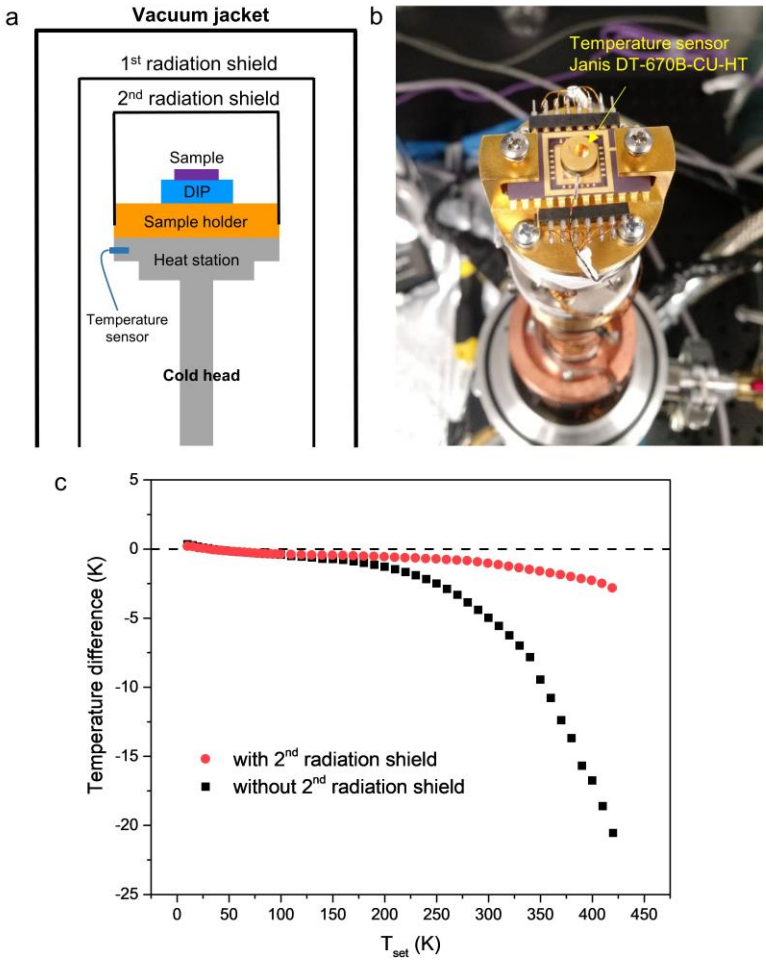

Figure 2.14 (a) Schematic drawing showing the inside of the cryostat. (b) A picture showing the approach of mounting the additional thermal sensor on the DIP. (c) Temperature difference between the measured local temperature and the setting temperature with and without the inner radiation shield mounted on the sample holder.

The difference between T_{DIP} and T_{set} is defined as T_{DIP} - T_{set}, which is plotted in **Figure 2.14c**. Above 30 K, the DIP temperature is lower than the set value, and difference increases as

temperature ramps up. At 420 K, T_{DIP} with two radiation shields is 2.8 K lower than T_{set}, while T_{DIP} with only one radiation shield is 20.6 K lower than T_{set}. Below 30 K, T_{DIP} is higher than T_{set}. This trend agrees with our expectation, and can be explained based on the thermal radiation between the vacuum jacket and the first radiation shield, as well as between the first and inner radiation shield. We note that the first radiation shield is mounted directly onto the coldhead while the inner radiation shield is mounted on the heating stage; thus at high T_{set}, the radiation heat transfer is always from the inner to the 1st radiation shield. However, at very low temperatures, as the vacuum jacket is close to room temperature, the radiation heat transfer to the first radiation shield will make its temperature slightly higher than the cold head temperature. As a result, the radiation heat transfer from the 1st to the inner radiation shield results in the device temperature higher than the setting values.

To further confirm the effectiveness of the inner radiation shield, we conducted the thermal conductivity measurements on the same silicon nanoribbon sample with and without the inner radiation shield. The measured electrical resistance of the heating and sensing membrane is very close for these two different configurations at low temperatures. However, without the inner radiation shield, as temperature increases, radiation heat transfer from the device to the environment becomes non-trivial, causing the temperature of the Pt thermometer to be lower than the setting temperature of the heating stage. This leads to a 4.2% and 3.7% difference of the measured resistance at 420 K for the heating and sensing membranes, respectively, compared with the case that has the inner radiation shield mounted.

As mentioned above, this seemingly small difference, however, renders an error in the derived TCR, and eventually an non-negligible error in the derived temperature rise for the heating and sensing membranes (Moore & Shi 2010, Shi et al. 2003). The overall effects on the measured

thermal conductance is shown in **Figure. 2.15**, where the measured sample thermal conductance for the case with double radiation shields starts to be higher than that for a single radiation shield at 150 K. The difference increases as the temperature ramps up and eventually results in a 23% difference in the measured sample thermal conductance at 420 K with a higher value for the double radiation shield case. Importantly, the temperature dependence is also quite different at higher temperature, which renders a great challenge in modeling the thermal conductivity. In fact, we cannot obtain a good fitting for the experimental data obtained without the inner radiation shield.

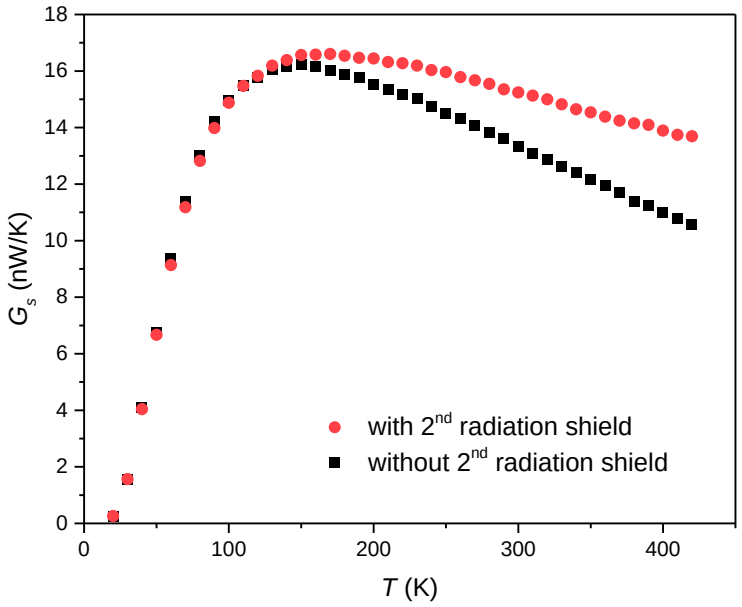

Figure 2.15 Comparison of measured sample thermal conductance of a 33 nm thick, 138 nm wide Si nanoribbon with and without the inner radiation shield.

2.3.2 Background Thermal Conductance and Cancellation

The enhanced resolution of bridge-based thermal measurements also involves the background conductance between the suspended beams as well as the two membranes. In fact, Zheng et al. demonstrated that the background thermal conductance only increases marginally after increasing the vacuum level from 10^{-6} mbar to 10^{-4} mbar (Zheng et al. 2013), indicating the dominant contribution of the radiation heat transfer. Although the temperature difference between the two

membranes is controlled to be small (ΔT_h-ΔT_s < 5 K), however, when dealing with very small thermal conductance (G_s) that is on the same order of magnitude as the background thermal conductance G_{bg}, the background heat transfer effect must be taken into account.

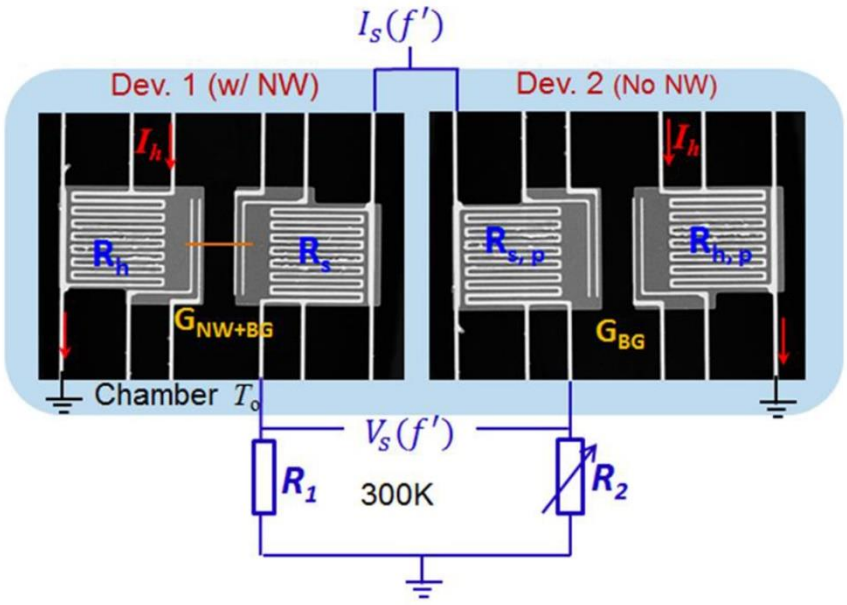

Figure 2.16 Schematic of the canceling bridge scheme for background thermal conductance subtraction (Zheng et al. 2013).

This background signal was subtracted by Zheng et al. through constructing a cancelling bridge circuit (Zheng et al. 2013). As shown in **Figure 2.16**, using this cancelling scheme, they could measure the conductance difference between a device with a nanowire sample (device 1) and a blank pair device (device 2) without nanowire. In the cancelling circuit, an identical heating current is applied to the heating sides of both device, and the temperature rise difference on the sensing sides of the two devices is directly measured using a Wheatstone bridge. They assume that the devices are almost identical and the background conductance are the same in these two devices. Thus, the measured thermal conductance is the intrinsic sample thermal conductance (i.e., $G_{NW} = G_{NW+BG_1} - G_{BG_2}$).

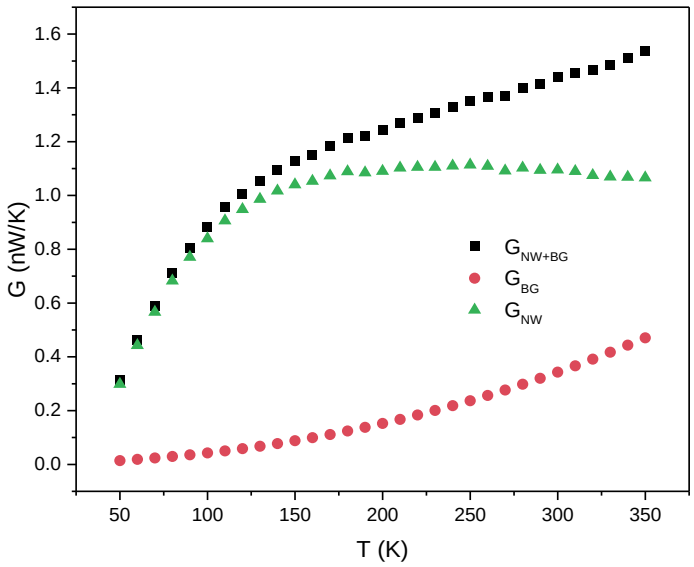

Figure 2.17 Measured total thermal conductance, G_{NW+BG}, background thermal conductance, G_{BG}, and the sample thermal conductance after the background subtraction, G_{NW}, for the 20 nm thick, 46 nm wide Si nanoribbon sample.

In addition to this cancelling bridge scheme, to subtract the contribution from the background thermal conductance, we could also measure an empty device with no nanowire bridging the two membranes. As the microheater devices were fabricated from the same batch, sharing nominally identical structures and dimensions, it is reasonable to assume that all devices with the same gap distance have approximately the same G_{bg}. The measured G_{bg} data were fitted to a 4th order polynomial function, and was subsequently subtracted from measured thermal conductance of the sample. Shown in **Figure 2.17** are the measured total thermal conductance, G_{NW+BG}, background thermal conductance, G_{BG}, and the sample thermal conductance after the background subtraction, G_{NW}, where the measured sample is a 20 nm thick, 46 nm wide Si nanoribbon. We can see that at 350 K, the background thermal conductance (~ 500 pW/K) is nearly half of the intrinsic thermal conductance of this thin nanoribbon sample (~ 1000 pW/K). In this case, it's imperative to cancel

out the contribution from the background radiation heat transfer to get the intrinsic thermal conductivity of the measured sample.

2.7 Summary

In this chapter, we discussed in details the experimental measurement approach including the experimental set-up, sample preparation, and data analysis. To fabricate nanostructures with irregular surface configuration using electron beam lithography, proximity effect correction has to be adopted to precisely assign the dose distribution and thus compensate for the electron beam interference effects. In addition, we have demonstrated that the effects of the radiation heat transfer from the measurement device to the surrounding environment can be nullified through adopting an additional radiation shield directly mounted on the sample stage. With the improved measurement scheme, we have further measured the thermal conductance of a 20 nm thick, 46 nm wide Si nanoribbon and the corresponding parasitic background conductance signal of a blank device. This indicates that for samples with very small conductance, the background signal would become a significant percentage of the measurement and therefore cannot be neglected.

Chapter 3

Thermal Conductivity of Individual Silicon Nanoribbons - Acoustic Softening Effect

Thermal transport in nanostructures is critical for many important applications including thermoelectrics (Boukai et al. 2008, Hochbaum et al. 2008, Lim et al. 2016, Majumdar 2004, Shi 2012, Tang et al. 2010), device thermal management (Li et al. 2005, Pop 2010), and nanocomposites (Jeng et al. 2008, Mingo et al. 2009). While significant progress has been made in the past two decades (Kim et al. 2001; Li et al. 2003a,b; Volz & Chen 1999b), several key issues related to size effects on thermal transport through nanostructures are still not fully understood. For example, although the classical size effect or Casimir limit, i.e., the reduction of effective phonon mean free path from boundary scattering, has been able to successfully explain many observations (Ju & Goodson 1999, Liu & Asheghi 2005), it fails to predict the thermal conductivity of silicon and germanium nanowires with critical dimensions less than 22 nm (Mingo et al. 2003). Therefore, exploring phenomena beyond those governed by the classical size effect is still of great interest.

The thermal conductivities of silicon nanostructures including films and nanowires have attracted a great deal of attention because of the importance of silicon in the semiconductor industry (Boukai et al. 2008, Hochbaum et al. 2008, Ju & Goodson 1999, Li et al. 2003b, Liu & Asheghi 2004). Through measuring the thermal conductivities of 74-240 nm thick silicon thin films, Ju and Goodson first pointed out that the intrinsic phonon mean free path of silicon could be as long as 300 nm at room temperature (Ju & Goodson 1999). Later, Li et al.(Li et al. 2003b) measured different diameter silicon nanowires, and found that the thermal conductivity of a 22 nm diameter wire showed an interesting temperature dependence and analyses also indicated that the thermal conductivity values were significantly lower than that predicted based on the classical size

effect (Dames & Chen 2004, Mingo et al. 2003). More recently, the thermal conductivities of thin silicon nanowires and nanotubes were measured (Chen et al. 2008, Wingert et al. 2015), which confirmed that for wire diameters below 30 nm, mechanisms beyond phonon-boundary scattering could play important roles. However, shown as in **Figure. 3.1**, a measurement of 20 nm thick silicon thin film suggested that the measured thermal conductivity could still be accounted for using the classical size effect (Liu & Asheghi 2004, 2005). As such, it is still necessary to explore the conditions for novel size effects beyond the Casimir limit to occur.

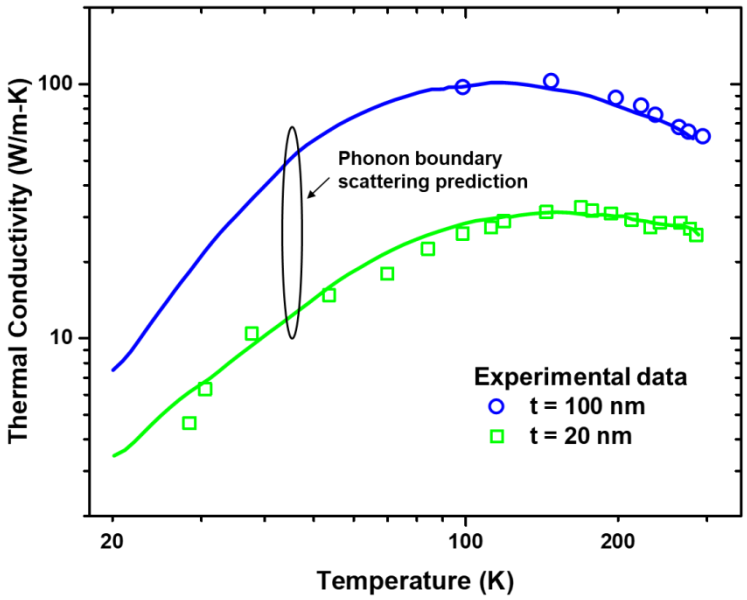

Figure 3.1 Measured thermal conductivity of 20 and 100 nm thick Si thin films, where the thermal conductivty is shown to be well captured by the classical size effects (Liu & Asheghi 2004, 2005).

In this chapter, we will discuss on measurements of the thermal conductivity of silicon nanoribbons of a thin (~20 nm) and a thick (~30 nm) group. Modeling and analysis disclose that for the thin ribbons, factors beyond the classical size effect have to be considered, which indicates that as the nanostructure dimension gets below a critical value, more complex size effects than phonon-boundary scattering will play a significant role.

3.1 Sample Preparation

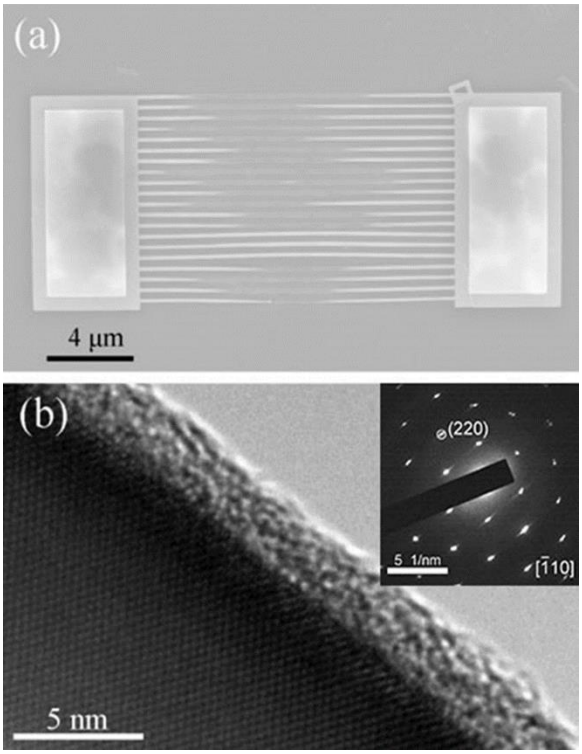

Figure 3.2 (a) An SEM micrograph of the as-fabricated silicon nanoribbon array. (b) An HRTEM micrograph of an individual silicon nanoribbon. The inset in (b) shows a SAED pattern of the nanoribbon taken along [$\bar{1}10$] zone axis.

Figure 3.2 shows a scanning electron microscopy (SEM) micrograph of the as-fabricated nanoribbon array and a high-resolution transmission electron microscopy (HRTEM) micrograph of an individual nanoribbon. The ribbon was patterned along the <110> direction as shown in the selected area electron diffraction (SAED) image in the inset of **Figure 3.2(b)**. For thermal measurement, the nanoribbon arrays were first transferred to a piece of polydimethylsiloxane (PDMS) by a stamping process. Then an individual ribbon was cut from the anchors, picked up by a sharp probe, mounted on an in-house assembled micromanipulator, and laid between two side-by-side suspended membranes integrated with microheaters/thermometers. After sample

preparation, the thermal conductivity of individual nanoribbons was measured using the well-established thermal bridge method.

3.2 Thermal Conductivity Measurements

In order to increase the measurement sensitivity, a Wheatstone bridge circuit was adopted through introducing a blank device, which helps to reduce the noise from the temperature fluctuations of the sample holder (Wingert et al. 2012). The measurements were performed in a high-vacuum cryostat system ($<10^{-6}$ mbar) with two radiation shields to minimize the radiation heat transfer effects. Thermal radiation from the devices, in addition to contributing to the background conductance, causes more complex effects to the temperature measurements of the heating and sensing membranes (Moore & Shi 2010). Results show that for these silicon nanoribbons, the difference between the measured thermal conductivities with and without an inner radiation shield directly mounted on the sample holder could be as large as 23% at 420 K; and more importantly, this difference can lead to an erroneous temperature dependence for the thermal conductivity above 150 K, which causes difficulties in theoretical modeling of the experimental results.

To eliminate the effects of residual thermal conductance from the background, we measured a blank device of identical configuration. The extracted background conductance (G_{bg}) was then subtracted from the measured sample thermal conductance. To examine the contact thermal resistance between the ribbon and suspended membranes, we conducted measurements for the same sample three times with different suspended lengths between the two membranes, as shown in **Figure 3.3(a-c)**. Based on the equivalent thermal resistance circuit shown in **Figure 3.3(d)**, the total thermal resistance, R_{tot}, should have a linear relationship with the suspended length (L_s) between the two membranes, which is indeed the case as shown in the inset of **Figure 3.3(e)**. The

R_{tot} versus L_s plot also indicates that the contact thermal resistance is marginal in the extracted thermal conductivity, as long as the measurement is conducted with a relatively long suspended length. This is confirmed by **Figure 3.3(e)** showing the measured effective thermal conductivity from three separate measurements and the extracted intrinsic thermal conductivity of the ribbon sample.

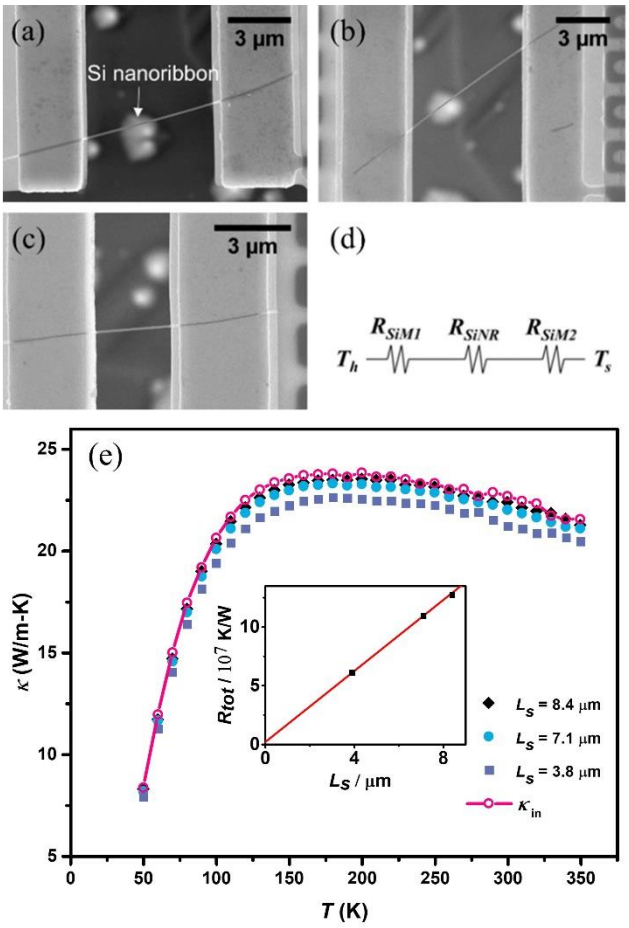

Figure 3.3 (a-c) SEM micrographs of the same Si nanoribbon sample with different suspended lengths between the two membranes, and (d) the corresponding thermal resistance circuit. The suspended length of the silicon nanoribbon between the two membranes is measured as (a) 7.1 μm (b) 8.4 μm (c) 3.8 μm, respectively. (e) Extracted intrinsic thermal conductivity of the Si nanoribbon together with the effective ones evaluated from each single measurement. The inset shows the linear relationship between R_{tot} and L_s at 300 K.

The difference between the intrinsic thermal conductivity and the effective one with a ribbon length of 7.1 μm is less than 2.5%. As such, in our measurements, we make sure that the suspended

ribbon length is larger than 7.0 μm for the thicker ribbons and 6.8 μm for the thinner ribbons, respectively, and neglect the effects of contact thermal resistance. Note that this is very different from our previous report on multi-wall carbon nanotube (MWCNT) (Yang et al. 2011a), which has a line contact with the membrane and the contact makes a significant contribution to the measured total thermal resistance. The silicon nanoribbons, on the other hand, make a flat contact of much larger area with the suspended membranes, leading to a negligible contact thermal resistance.

For silicon nanoribbons, it is nearly inevitable to have thin amorphous oxide layers on their surface, which makes the actual cross-sectional area of the silicon core smaller. Our silicon nanoribbons also possess an oxide layer of ~1.5 nm, as determined through measuring the thickness at single and double nanoribbon segments of a two ribbon stack after hydrofluoric acid etching. The TEM micrograph of **Figure 3.2(b)** indicates an oxide thickness slightly larger than 2 nm; however, this amorphous layer is on the side wall of the silicon nanoribbon, which includes the effects of non-perfectly vertical side-walls from the reactive ion etching. To account for the effects of this oxide layer, we subtract the contribution of the amorphous shell based on an oxide thickness of 1.5 nm on each surface and the thermal conductivity of silicon oxide using the parallel resistance model. Based on the extracted thermal conductance of the crystalline silicon core, the thermal conductivity of the silicon nanoribbon is derived with the core dimension, which is also used as labels in the figures.

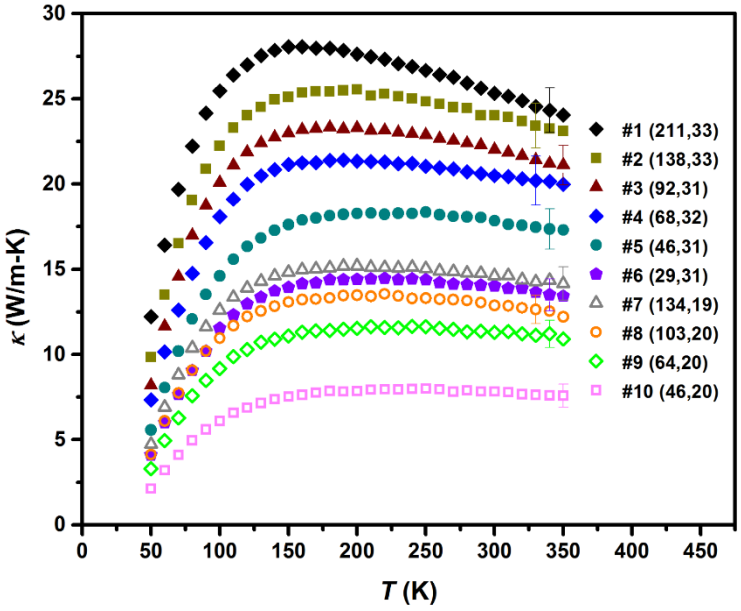

Figure 3.4 Measured thermal conductivities of silicon nanoribbons. The legend indicates the width and thickness (Si core dimensions) of the cross section for the measured samples.

Figure. 3.4 plots the measured thermal conductivity of different nanoribbons over a temperature range of 50–350 K. In general, the measured thermal conductivities are much lower than the corresponding bulk value (Ho et al. 1972), which can be attributed to the strong phonon-boundary scattering. Moreover, as the ribbon size reduces, the signature of Umklapp scattering becomes less distinguishable.

3.3 Thermal Conductivity Modeling of Si Nanoribbons

To examine whether size effects other than boundary scattering occur in these ribbons, we modeled the thermal conductivity of the measured samples by combining the Callaway model with the Fuchs-Sondheimer (FS) reduction function (Callaway 1959, Holland 1963, Josell et al. 2004, Sondheimer 2001). The FS function has been widely used to study electron transport by considering the classical size effect through including scattering at the surfaces of metallic thin films and thin wires (Josell et al. 2004, 2009; Steinhögl et al. 2002). In this approach, the bulk

relaxation time $\tau_{j,bulk}$ for phonons of mode j is modified by a reduction function F as $\tau_{j,r} = F\tau_{j,bulk}$ (Chambers 1950, Sondheimer 2001). For wires of rectangular cross-section, Chambers derived an integral expression for the reduction function based on kinetic theory: $F(w,h,l_j) = 1 - \sigma\langle w,h,l_j\rangle - \sigma\langle h,w,l_j\rangle$ (Chambers 1950), where σ is given by

$$\sigma\left\langle w,h,l_j\right\rangle = \left(\frac{6}{4\pi\cdot wh}\right)\cdot\int_0^w dx\int_0^h dy\int_{-\arctan\left(\frac{y}{w-x}\right)}^{\arctan\left(\frac{h-y}{w-x}\right)} d\varphi\int_0^\pi \sin\theta\cos^2\theta\exp\left(\frac{x-w}{l_j\sin\theta\cos\varphi}\right)d\theta\,. \quad (3.1)$$

Here w and h are the width and height of the cross section respectively, and l_j is the carrier mean free path in bulk media. The integration is over all directions of azimuthal angle θ, radial angle φ, and from all locations in the cross-sectional area. In this expression, a completely diffusive boundary condition is assumed at the surface, and the carrier mean free path is reduced as a result of the diffusive scattering on the surface.

Taking into account the nonzero specularity parameter p for the surface scattering, the reduction function can be modified as (Josell et al. 2004):

$$F\left(w,h,l_j,p\right) = \left(1-p\right)^2\sum_{k=1}^{\infty} kp^{k-1}F\left(w,h,l_j,p=0\right). \quad (3.2)$$

The dependence of specularity parameter on the phonon wave length is accounted for following Soffer's model: $p(q) = \exp(-4q^2\eta^2)$ (Soffer 1967), where q is the amplitude of the wave vector, and η is the surface roughness. Note that Equation (3.2) is strictly valid only when the specularly scattered phonons travel equal distance between successive scattering events (Josell et al. 2004), which is not exactly the case for ribbons of rectangular cross section. As such, using Equation (3.2) could introduce some inaccuracy; however, given that the specularity parameter is quite small and the difference in phonon travel distance is not significant, Equation (3.2) should be an acceptable approximation.

Combining the reduction function with the Callaway model then yields (Callaway 1959, Holland 1963)

$$\kappa = \frac{1}{6\pi^2}\sum_j \int_q F(v_j(q)\times\tau_j(q))\frac{\hbar^2\omega_j(q)^2}{k_B T^2}\frac{\exp(\frac{\hbar\omega_j(q)}{k_B T})}{(\exp(\frac{\hbar\omega_j(q)}{k_B T})-1)^2} v_j(q)^2\tau_j(q,T)q^2 dq\,, \qquad (3.3)$$

where $\hbar$ is the reduced Plank constant; k_B is the Boltzmann constant; T is temperature; and $v_j(q) = \partial\omega_j/\partial q$ is the phonon group velocity. $\omega(q)$ is phonon frequency, and a 4th order polynomial fitting to experimental dispersion relation of bulk silicon was adopted (Brockhouse 1959, Nilsson & Nelin 1972). The summation is over all different phonon modes j. For Si, the phonon scattering lifetime τ is dominated by Umklapp, defects, and boundary scattering, which are determined as $\tau_{j,Umklapp}^{-1} = BT\omega_j(q)^2\exp(-C/T)$, $\tau_{j,defects}^{-1} = D\omega_j(q)^4$, and $\tau_{j,boundary}^{-1} = v_j(q)/E$, respectively. The total relaxation time is calculated using the Matthiessen's rule as follows: $\tau_{j,bulk}^{-1} = \tau_{j,Umklapp}^{-1} + \tau_{j,defects}^{-1} + \tau_{j,boundary}^{-1}$. The constants B, C, D, and E are determined by fitting Equation (3.3) to measured bulk Si data (Ho et al. 1972, Hopkins et al. 2009).

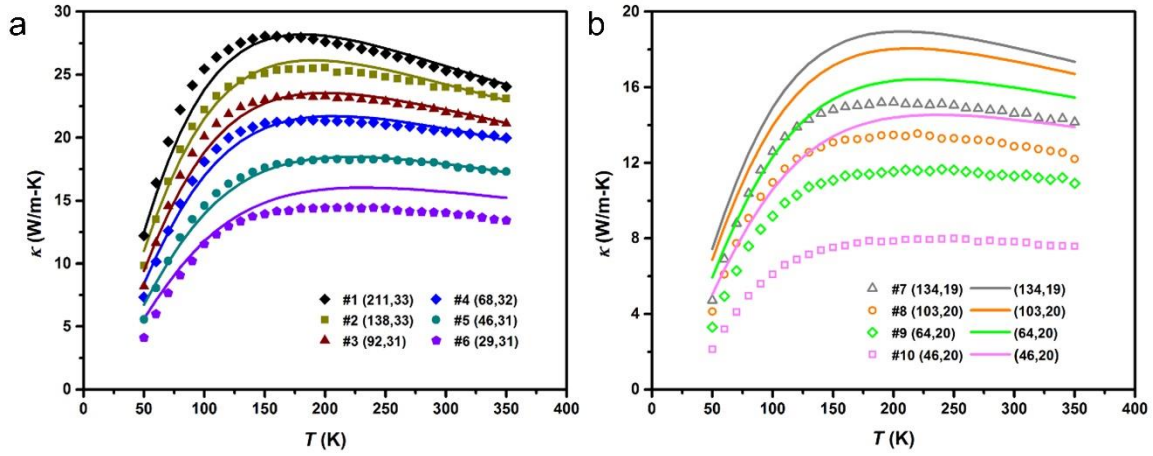

Figure 3.5 (a) Comparison between the modeling and experimental results. For thick Si nanoribbons, the modeled k (solid lines) agrees well with the experimental data except for the sample of smallest dimension. (b) For thin Si nanoribbons, the calculated k is significantly higher than measured values and the overestimation increases as the ribbon width reduces.

Several factors need to be considered in modeling the thermal conductivity of the measured Si nanoribbons. First, the ribbons are fabricated from doped SOI wafers, which means they should have a higher impurity level. Moreover, the reactive ion etching process could also introduce some damage due to ion bombardment to the sidewall. In addition, since these ribbons have flat top and bottom surfaces from the polished wafer, the surface roughness may be quite low, and the specularity parameter might not be zero. As such, we treat the factors for defect scattering, D, and surface roughness, η, as two fitting parameters, while keeping B, C and E, which are adopted from fitting the bulk, unchanged. The best fitting for the thick group Si nanoribbons was obtained with the following parameters $B = 1.45\times10^{-19}$ sK^{-1}, $C = 142$ K, $D = 3.5\times10^{-45}$ s^3, $E = 2\times10^{-3}$ m, $\eta = 0.18$ nm. While this fitted surface roughness value is very small, it is reasonable given that the atomically smooth silicon surface for the silicon wafer. In fact, in a recent work on silicon nano-membranes, the measured RMS surface roughness using atomic force microscope (AFM) is even smaller, only 0.12 nm (Schroeder et al. 2015). As shown from **Figure 3.5a**, the modeling results fit the experimental data of the ~30 nm thick ribbons very well other than the ribbon with the smallest dimension (29 nm wide and 31 nm thick), and the thermal conductivity decreases continuously as the ribbon width reduces. In many studies of phonon transport, the lowest dimension, instead of the Casimir length, is used to evaluate the size effects. Our results show that even with a thickness as small as 31 nm, lateral dimension can still lead to a significant difference in thermal conductivity, which is true even when the width/thickness aspect ratio is larger than 7.

For the thin group nanoribbons, however, applying the same fitting parameters as the thick group led to unacceptable modeling results, as shown in **Figure 3.5b**. While the modeling results correctly predict that the thermal conductivity reduces as the lateral dimension shrinks, the absolute values from the modeling are significantly higher than the experimental data. The

overestimation is smaller for wider ribbons (~24% at 300 K) and increases for narrow ribbons, reaching ~83% for the 46 nm wide ribbon. As such, these measurements with nanoribbons of systematically varied dimensions, indicate that for 20 nm thick nanoribbons, their thermal conductivity cannot be explained based on the classical size effect. This further confirms the observation for ultrathin nanowires (Chen et al. 2008, Li et al. 2003b); and similar to thin nanowires, the critical transition dimension is also around 30 nm and the deviation from the classical size effect can be clearly seen for 20 nm thick ribbons.

To examine the variation of the thermal conductivity versus the Casimir length (L_C), we solve for the L_C of these nanoribbons as $L_C = 2\sqrt{wt}/\sqrt{\pi}$ (Hippalgaonkar et al. 2010, Lü et al. 2003), where *w* and *t* are the width and thickness of the ribbon, respectively. **Figure 3.6** plots the thermal conductivities of various silicon nanostructures including the measured nanoribbons versus the Casimir length (Boukai et al. 2008, Hippalgaonkar et al. 2010, Hochbaum et al. 2008, Li et al. 2003b, Liu & Asheghi 2005). For our samples, the thermal conductivities of both the thicker and thinner ribbons have a linear relationship with the Casimir length. However, the thermal conductivity values for the two groups are different at the same Casimir length, and the two groups demonstrate distinct slopes.

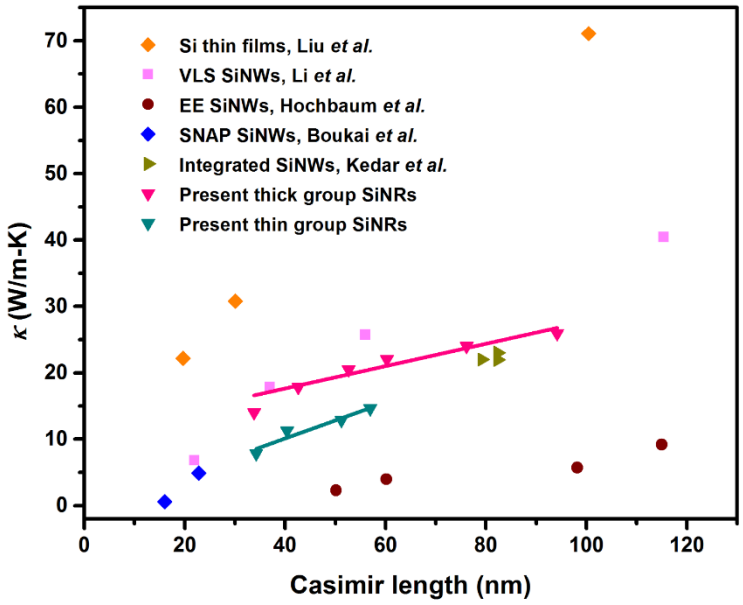

Figure 3.6 Room temperature (300 K) thermal conductivities of various silicon nanostructures as a function of Casimir length (L_C) (Boukai et al. 2008, Hippalgaonkar et al. 2010, Hochbaum et al. 2008, Li et al. 2003b, Liu & Asheghi 2005). As shown in the figure, the slope of thermal conductivity versus Casimir length is different for the thick and thin Si nanoribbons.

3.4 Young's Modulus Measurement for Si Nanoribbons

As demonstrated recently for ultrathin silicon nanotubes (Wingert et al. 2015), as the critical dimension gets smaller, more atoms will be affected by the surface and the mechanical properties of the materials can be different from that of the bulk (Sadeghian et al. 2011, Shim et al. 2005, Zhu et al. 2009). Important for thermal transport is the Young's modulus, which is related to the speed of sound as $v = \sqrt{E/\rho}$, in which E and ρ are the Young's modulus and density, respectively. If the speed of sound is different, according to the thermal conductivity expression derived from the kinetic theory, $\kappa \sim Cvl$ (C: specific heat and l: phonon mean free path), the thermal conductivity can be different and show a different slope versus the Casimir length in the regime where the mean free path is dominated by the Casimir length.

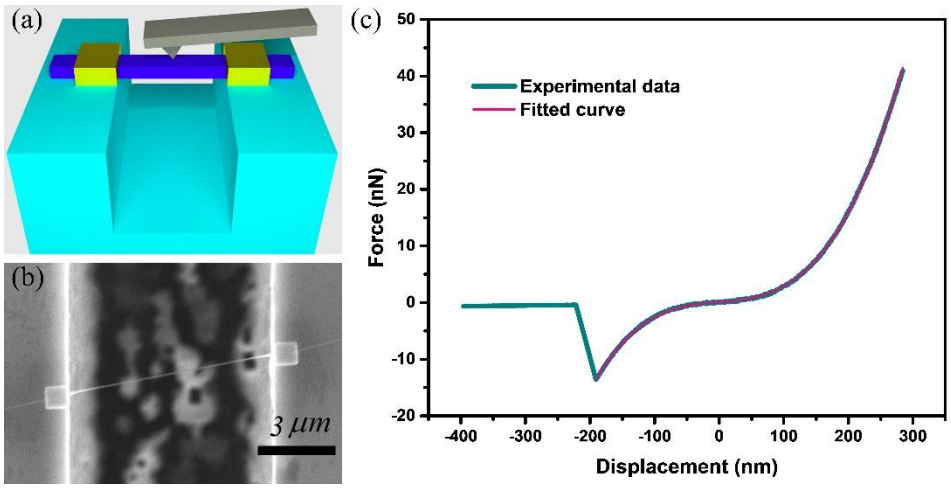

Figure 3.7 (a) Schematic drawing showing the three-point bending test scheme. (b) SEM micrograph of the measured nanoribbon sample (34 nm thick, 32 nm wide) suspended over a 7 μm wide Si trench with both ends clamped by a layer of Pt through EBID. (c) Measured F-D curve (blue) and fitted curve (red) according to the analytical model for the measured Si nanoribbon shown in (b) with a suspended length of 8.4 μm.

To confirm whether the difference between the thinner and thicker ribbons are from the effects of reduced Young's modulus, we experimentally tested the Young's modulus of the ribbons using a three-point bending test with an atomic force microscope (AFM, Bruker Dimension Icon). For this study, we transferred silicon nanoribbons to bridge a 7 μm wide trench etched on a silicon chip, after which a layer of Pt was applied through electron beam induced deposition (EBID) to clamp both ends of the ribbon, as shown in the inset of **Figure 3.7**. Before each measurement, the sensitivity of the cantilever is calibrated by tapping it on the hard Si substrate and the spring constant is extracted through a thermal tune process. By scanning the Si nanoribbon using AFM, we can locate its middle point across the trench.

We then performed the bending test at its middle point to obtain the force-deflection (FD) curve shown in **Figure 3.7(c)**, from which the Young's modulus of the sample was extracted through fitting the FD curve using a theoretical model of a suspended elastic string with fixed ends

(Bellan et al. 2005, Calahorra et al. 2015, Li et al. 2014a). The force F exerted to the middle point of the ribbon can be expressed as a function of the deflection, $u(L/2)$, as:

$$F = \frac{192EI}{L^3} u\left(L/2\right) f\left(\alpha\right), \tag{3.4}$$

where E is the effective Young's modulus of the sample, I is the area moment of inertia and L is suspending length of the ribbon sample. When the deflection is greater or comparable to the ribbon thickness, tensile forces due to stretching become significant, and $f(\alpha)$ is

$$f\left(\alpha\right) = \frac{\alpha}{48 - \dfrac{192\tanh\left(\sqrt{\alpha}/4\right)}{\sqrt{\alpha}}}. \tag{3.5}$$

For displacements that are more than 10 times larger than the sample thickness, $f(\alpha)$ can be approximated within 2% difference using:

$$f_{app}\left(\alpha_{app}\right) = 1 + 2.412\times10^{-2}\alpha_{app} - 1.407\times10^{-6}{\alpha_{app}}^2, \tag{3.6}$$

where

$$\alpha_{app} \equiv \frac{L^2T_0}{EI} + \frac{6\varepsilon\left(140+\varepsilon\right)}{350+3\varepsilon}, \tag{3.7}$$

and T_0 is the residual tension, $\varepsilon = u^2S/I$, and S is the ribbon cross-sectional area. The bending tests were repeated three times for each sample with reproducible results. In fact, this fitted Young's modulus is an effective value, E_{eff}, of the composite structure that consists of a Si core, E_{core}, and a SiO_2 shell, E_{shell}. As such, to consider the effects of the oxide shell, a revised core-shell composite model was adopted to obtain the Young's modulus of the silicon core (Calahorra et al. 2015, Chen et al. 2006):

$$E_{eff}I_{eff} = E_{shell}I_{shell} + E_{core}I_{core}, \tag{3.8}$$

where I_{shell} and I_{core} are area moment of inertia of shell and core, respectively.

Because of the importance of surface atoms, we plot the Young's modulus as a function of the surface-area-to-volume ratio (*S/V*), as shown in **Figure 3.8**. The bending test yields the Young's modulus along the <110> direction and the measured Young's modulus for the thick group Si nanoribbons except for the 29 nm wide one is very close to the bulk value of $E_{110} = 170$ GPa (Calahorra et al. 2015, Zhu et al. 2009). However, for the 29 nm wide, 31 nm thick ribbon and for ribbons in the thin group, the extracted Young's moduli are significantly less than the bulk value and in fact, there exists a general trend of lower Young's modulus for larger surface-area-to-volume ratio.

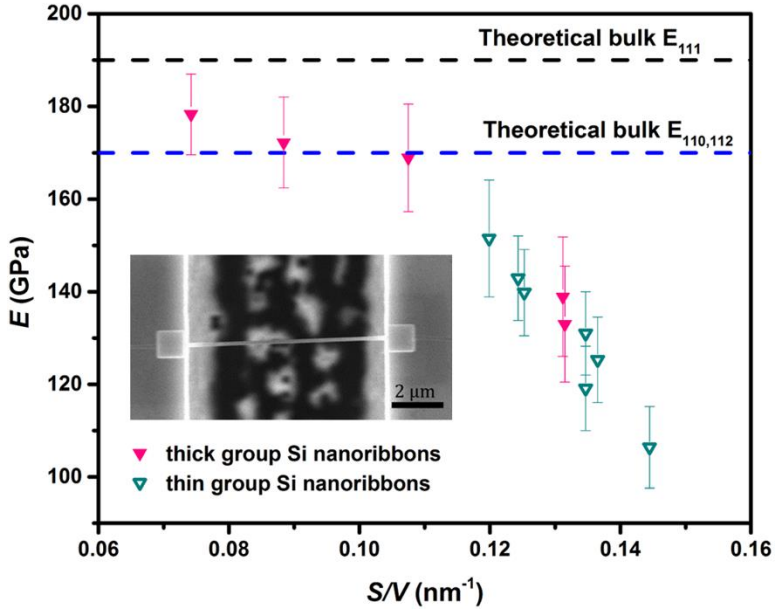

Figure 3.8 Measured Young's modulus of the Si nanoribbons as a function of the surface-area-to-volume ratio. The Young's modulus starts to deviate from the bulk value as the surface-area-to-volume ratio reach ~0.11 nm^{-1}. The inset shows a Si nanoribbon suspended across a trench of 7 μm wide with EBID Pt deposited at the two ends to anchor the ribbon for the Young's modulus measurement.

3.5 Regime Map for Thermal Conductivity versus Surface-area-to-volume Ratio

The Young's modulus measurement strongly suggests that the reduced mechanical properties, and thus the lower speed of sound, could significantly contribute to size effects beyond the classical

Casimir limit for the 20 nm thick silicon nanoribbons. The lower than bulk Young's modulus for the 29 nm wide, 31 nm thick ribbon could also explain the relatively poor fitting in **Figure. 3.5a** for this sample. Note that our observation is different from that of Liu and Asheghi (Liu & Asheghi 2004), which suggested that the thermal conductivity of 20 nm thick silicon thin films could still be predicted by the classical size effect. Two possible reasons can account for the difference: (1) for their measurements, a >70 nm thick CoFe film layer was deposited on top of the silicon layer, which is different from the free-standing ribbons we measured; and (2) the width of their thin film (not available in Liu & Asheghi 2004) could be much larger, which could render the deviation of the Young's modulus from the bulk small.

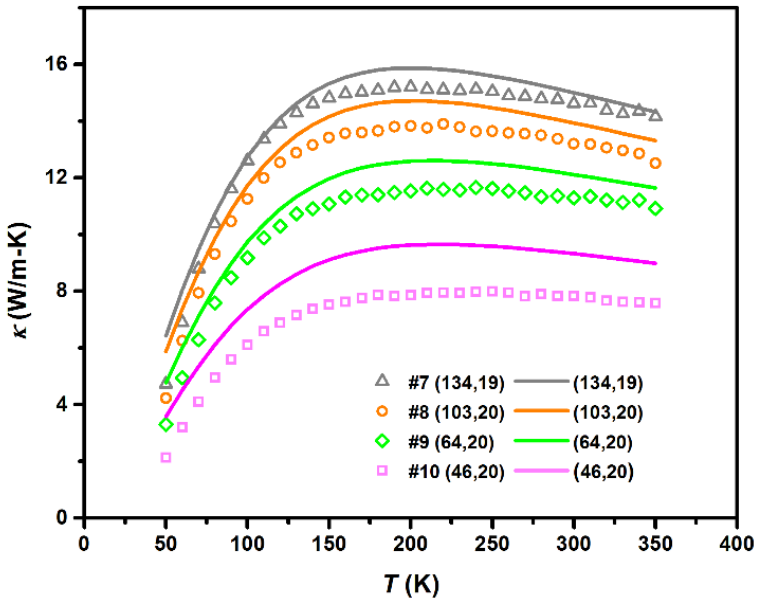

Figure 3.9 The comparison of measured thermal conductivity and modeled results after considering the elastic softening effects for thin group Si nanoribbons.

The deviation of the modeling results for thinner ribbons is to show that without taking into account the elastic softening effects on phonon transport, we cannot obtain satisfactory prediction for the thin group ribbons. In order to consider the elastic softening effects, we further modified the model by scaling down the phonon group velocity using the measured reduced Young's

modulus (E) for the thin group Si nanoribbons. As the speed of sound v is related to Young's modulus as $v = \sqrt{E/\rho}$, where ρ is the density, we use a scaling factor for the phonon group velocity as $\sqrt{E_{SiNR}/E_{bulk}}$. As shown **Figure. 3.9**, after scaling the phonon group velocity and keeping all other fitting parameters unchanged, the modeled thermal conductivity for thin group Si nanoribbons are much closer to the measured data. In fact, the maximum overestimation of the modeled result for the 20 nm thick and 46 nm wide sample decreases from 83% to 19%. The remaining difference could be due to the simple scaling approach, as the speed of sound doesn't depend on frequency, while phonon group velocity changes remarkably versus phonon frequency. As such, for higher frequency phonons, the scaling factor might not be very accurate.

Figure 3.6 shows that even at the same Casimir length, the thermal conductivity of different silicon nanostructures could be quite different, which suggests that in addition to the Casimir length, other parameters, such as the cross-section aspect ratio, could play a significant role. One parameter that is related to both the Casimir length and the cross-section aspect ratio is the surface-area-to-volume ratio (*S/V*), defined as $2(w + t)/(wt)$ for a rectangular cross-section. If we term the cross section area as *A* and aspect ratio as *c*, *S/V* can also be expressed as $2(\sqrt{c} + \sqrt{1/c})/\sqrt{A}$. Note that the Casimir length is proportional to $\sqrt{A}$, which is thus inversely related to *S/V*. Since *S/V* should be an important factor in the phonon-boundary scattering process, we plot the thermal conductivity of various silicon nanostructures versus the surface-area-to-volume ratio (Ju & Goodson 1999, Li et al. 2003b, Liu & Asheghi 2005, Wingert et al. 2015, Yu et al. 2010), as shown in **Figure 3.10**. Interestingly, the thermal conductivities of all different silicon nanostructures dominated only by the classical size effect follow the general trend of inversely proportional to *S/V*. This type of plot has been presented for nanoparticle composites Si/Ge nanowires (Jeng et al.

2008), and periodically patterned Si nanostructures (Anufriev et al. 2016), in which a similar trend has been observed.

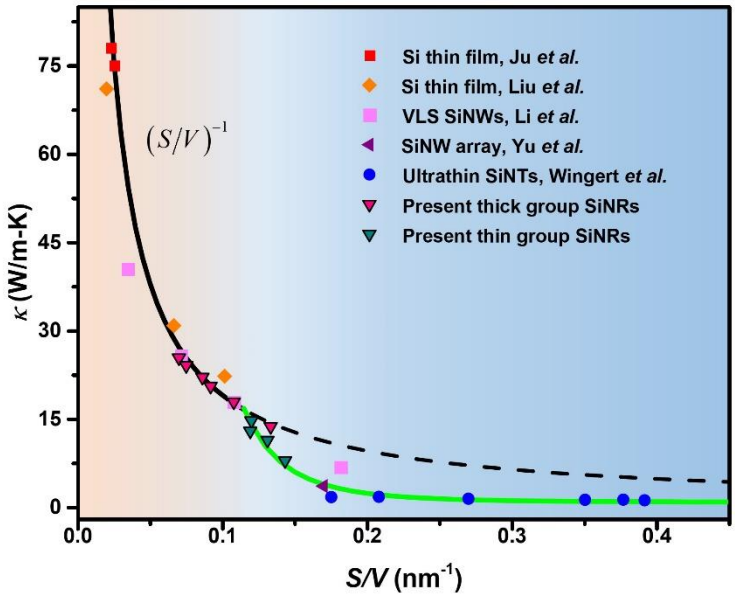

Figure 3.10 Room temperature (300 K) thermal conductivities of various silicon nanostructures versus their surface-area-to-volume ratio (*S/V*), which clearly shows two regimes where size effects beyond phonon-boundary scattering are important or not (Ju & Goodson 1999, Li et al. 2003b, Liu & Asheghi 2005, Wingert et al. 2015, Yu et al. 2010).

Importantly, this inverse relation does not hold for the thin group silicon nanoribbons, the 22 nm diameter silicon nanowire (Li et al. 2003b), the thin Si nanowire array (Yu et al. 2010), and the ultrathin silicon nanotubes (Wingert et al. 2015), suggesting again that other than the classical size effect, at sub 30 nm scale, other effects such as reduced Young's modulus, could play a significant role. In fact, the data for thin nanoribbons and ultrathin silicon nanotubes provide insights into how the thermal conductivity of silicon nanostructures changes as sizes get into the regime beyond the classical size effect. Note that while previously published theoretical modeling claimed that the measured thermal conductivity of the 22 nm silicon nanowire was lower than the prediction based on the classical size effect (Mingo et al. 2003), it is in fact higher than the trend derived above. The reason could be that the background conductance is not excluded in the

measurement for the 22 nm wire. The total measured thermal conductance of the 22 nm diameter wire at room temperature is around 1 nW/K, and the background thermal conductance at room temperature is usually around ~300-400 pW/K for the suspended micro-devices. As such, subtracting the background conductance could lead to significantly lower thermal conductivity. In comparing **Figure 3.8** and **Figure 3.10**, the deviation of the measured Young's modulus from the bulk value and the deviation of the thermal conductivity from the classical size effect both occur at approximately the same *S/V* value, which provides strong support to the important role of Young's modulus in thermal conductivity reduction of silicon nanoribbons as the critical dimension reduces to less than ~30 nm.

3.6 Conclusion

In summary, the thermal conductivities of two groups of silicon nanoribbons of ~30 nm and ~20 nm thick, respectively, have been measured and modeled. Results show that while the classical size effect can account for the thermal conductivity reduction for most of the thicker ribbons other than the narrowest one (29 nm wide), it fails to predict the thermal conductivity of the thinner ribbons. Measurements of the Young's modulus of the ribbons suggest that in the thinner ribbons, the speed of sound could be significantly reduced, which can lead to size effects beyond phonon-boundary scattering. It is also found that while the dependence of the thermal conductivity on the Casimir length for different silicon nanostructures could be quite different from each other, the plot of thermal conductivity versus the surface-area-to-volume ratio clearly delineated two regimes where the effects beyond the classical size effect must be considered or not. This study provides new evidence for size effects beyond the Casimir limit and could guide nanoengineering of thermal conductivity in a new regime.

Chapter 4

Thermal Transport through Double Si Nanoribbons with Composite van der Waals Interface

Amorphous silicon dioxide (a-SiO_2) has been an indispensable component as dielectric materials in silicon-based microelectronic devices (Ferain et al. 2011, Koh 2001, Nguyen et al. 2009, Thompson et al. 1998, Timp et al. 2000). The low thermal conductivity of a-SiO_2 and the thermal boundary resistance at the interfaces between SiO_2 and other thin film layers are of major concerns in device thermal management (Chen et al. 2012, Deng et al. 2014, Hurley et al. 2011). In fact, aggressive miniaturization of microelectronic devices has reduced the thickness of gate oxide down to a mere 1.5 nm in metal-oxide-semiconductor field-effect transistors (MOSFETs) (Momose et al. 2003). As such, thermal transport through thin a-SiO_2 layers is of fundamental importance for cooling of microelectronic devices, yet the detailed transport mechanisms remain an issue of debate (Braun et al. 2016, Cahill et al. 1992, Goodson et al. 1994, Graebner et al. 1986, Hu et al. 2015, Larkin & McGaughey 2014, Lee & Cahill 1997, Regner et al. 2013).

Classically, according to the amorphous limit model proposed by Einstein, heat conduction in greatly disordered materials, such as a-SiO_2, is treated as random walks of independent oscillators (Einstein 1911), which corresponds to a mean free path (MFP) approximately the same as the interatomic distance (i.e., <1 nm) (Kittel 1949). However, this physical picture has been kept challenged and reaffirmed over the past decades, in the efforts to develop a modern understanding of thermal transport through a-SiO_2 (Wingert et al. 2016b).

For example, measurements of the effective cross-plane thermal conductivities of thin a-SiO_2 layers indicated a thickness dependence up to 10 nm at room temperature, which was attributed to contributions from long wavelength phonons that could transport ballistically through the a-SiO_2 films and experience phonon-boundary scattering (Goodson et al. 1994). However, later studies

argued that the observed thickness dependence could be due to the thermal boundary resistance between the a-SiO_2 layer and its substrate but not the reduced phonon MFP in a-SiO_2 layers from boundary scattering (Griffin et al. 1994, Lee & Cahill 1997).

More recently, efforts have been made to distinguish the contributions of different vibrational modes (i.e., propagons, diffusons, and locons) to thermal transport in a-SiO_2 (Wingert et al. 2016b). Both experiments and numerical modeling have been conducted, and the results indicate that thermal transport in a-SiO_2 is dominated by diffusons while propagons only make a marginal contribution (Braun et al. 2016, Hu et al. 2015, Larkin & McGaughey 2014, Regner et al. 2013). For example, using time domain thermoreflectance (TDTR) technique, the measured cross-plane thermal conductivity of a 3 nm thick a-SiO_2 film remains bulk-like at room temperature, suggesting negligible contribution from propagons (Braun et al. 2016). Meanwhile, based on molecular dynamics (MD) simulations, it has been argued that diffusons are the dominant energy carriers in a-SiO_2 with less than 6% contribution from propagons to its thermal conductivity (Larkin & McGaughey 2014).

One subtle point that has not been explicitly discussed is the potential difference between energy transport in bulk a-SiO_2 and through a-SiO_2 thin films in contact with crystalline materials; while the latter is in fact more relevant to cooling of microelectronic devices. Even though the concept of thermal phonons might not be appropriate for describing vibrational modes in bulk a-SiO_2, phonons from crystalline materials can propagate through a-SiO_2 films in contact with them. This difference, however, is not important if the penetration depth of thermal phonons in a-SiO_2 is approximately the same as the interatomic distance. We note that phonon transmission through Si/a-SiO_2/Si sandwiched structures has been studied using wave packet simulations (Deng et al. 2014, Liang et al. 2017); and the results suggested that a large portion of phonons with frequencies

up to 1.4 THz, which contribute more than 20% to the thermal conductivity of silicon (Esfarjani et al. 2011), could still ballistically penetrate through a 10 nm a-SiO_2 layer. However, no convincing experimental demonstration of this prediction has been reported.

To date, nearly all measurements of thermal transport through a-SiO_2 films have been carried out in the cross-plane direction, using either the three-omega method or TDTR (Goodson et al. 1994, Hu et al. 2015, Lee & Cahill 1997, Regner et al. 2013). One challenge associated with the cross-plane approach is the dual effects of phonon-boundary scattering, which leads to both reduced effective phonon MFP and thermal boundary resistance; while decoupling these two factors at a nanometer scale is tricky. Therefore, it could be difficult to draw solid conclusion on the ballistic phonon penetration depth through a-SiO_2.

Measurement of in-plane thermal conductivity, on the other hand, could provide valuable information about ballistic phonon transmission through interfaces. For example, comparison of the in-plane thermal conductivities of single and double boron nanoribbons stuck together via van der Waals (vdW) interactions helped to determine the percentage of phonons that could ballistically pass through the vdW interface (Yang et al. 2011b). In the regime where intrinsic phonon MFP is much larger than the nanoribbon thickness, if phonons can ballistically transmit through the interface between two ribbons, the effective phonon MFP in the double ribbon will be extended, leading to an enhanced thermal conductivity for the double ribbon. Therefore, comparison of the in-plane thermal conductivities of single and double silicon nanoribbons with a layer of a-SiO_2 on their surfaces could help to determine the ballistic penetration depth of phonons through a-SiO_2.

In this chapter, we will show that the thermal conductivity of double silicon nanoribbons with a layer of a-SiO_2 sandwiched in between can indeed be higher than that of corresponding single

ribbons, indicating that thermal phonons can ballistically transmit through composite vdW interfaces with a thin a-SiO_2 layer. For an annealed double ribbon sample with high adhesion energy between the two ribbons and an oxide thickness of ~5.1 nm, we observed ~11% thermal conductivity enhancement at 300 K, indicating that thermal phonons can ballistically penetrate through an a-SiO_2 layer of more than 5 nm.

4.1 Double Si Nanoribbon Sample Preparation

To prepare double ribbon bundles, we used a sharp probe to pick up one ribbon and stacked it on top of another one sitting on a polydimethylsiloxane (PDMS) substrate. Through careful alignment with the microprobe, these two ribbons, bonded together by vdW interactions, can overlap with each other almost perfectly. The resulting double ribbon was then transferred to a microdevice for subsequent thermal measurement (Shi et al. 2003, Wingert et al. 2012, Zhang et al. 2017).

Figure 4.1a shows a scanning electron microscopy (SEM) micrograph of a double ribbon sample after it was transferred to the measurement device and placed between the two suspended membranes with integrated resistance heaters/thermometers. **Figure 4.1b** presents an atomic force microscopy (AFM, Bruker Dimension Icon) image of the denoted section in **Figure 4.1a**, which clearly demonstrates the different heights of the overlapped and non-overlapped ribbon segments, confirming nearly complete overlapping of the two ribbons. Based on the AFM and SEM measurements, the dimensions of the silicon core in each ribbon are 18 ± 1 nm thick and 140 ± 2 nm wide after subtracting a 2.5 nm thick a-SiO_2 layer on each surfaces.

To investigate how the a-SiO_2 layer affects ballistic phonon transport through the Si/a-SiO_2/Si sandwiched structure, we prepared multiple double ribbon samples with different a-SiO_2 thicknesses at the interface. To achieve this, a well-aligned double ribbon bundle was first

transferred from the PDMS substrate to a petri-dish (polystyrene, Fisher Scientific). The sample was then immersed in a drop of buffered oxide etchant (BOE, 6.38% HF, Sigma-Aldrich) for 2 mins, after which the double ribbon sample was rinsed with reagent alcohol (Fisher Scientific). To minimize the oxidization effects on the HF-etched double ribbons after being transferred to the measurement device, it was either stored in a high vacuum chamber (<10^{-6} mbar) or immediately loaded into the cryostat for thermal measurement. On the other hand, to achieve thicker interfacial oxide layers, ribbon bundles were left in the ambient environment (AE) for various durations.

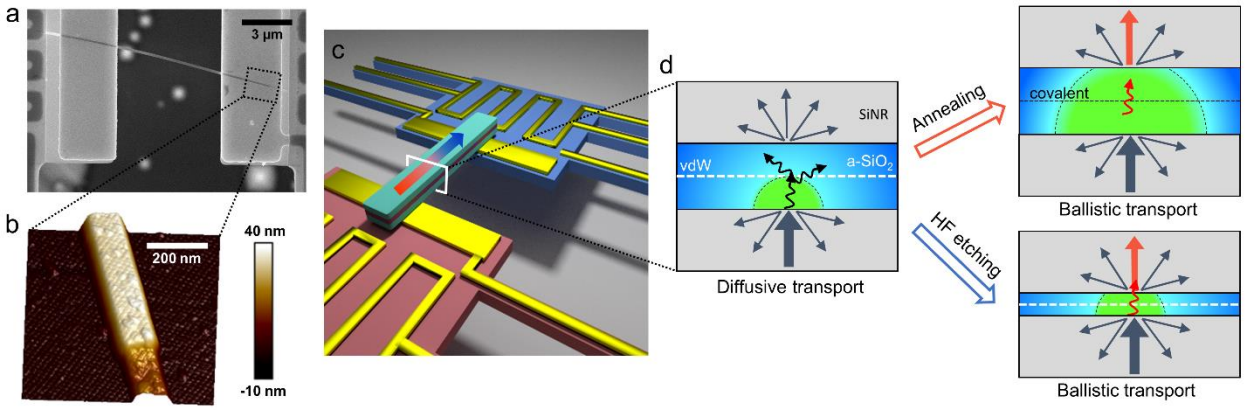

Figure 4.1 (a) An SEM micrograph showing the double Si nanoribbon after being transferred to the measurement device. (b) Zoom-in view showing the AFM scanning result at one end of the double ribbon sample, where the edge of one Si nanoribbon is fully overlapped with the other ribbon. (c) A schematic illustration showing the in-plane thermal conductivity measurement for a double Si nanoribbons sample. (d) Illustration of phonon diffusive/ballistic transport through the Si/a-SiO_2/Si composite interface. Phonons could ballistically transport through the composite interface after the double ribbon is annealed at high temperature or the interfacial a-SiO_2 layer thickness is reduced.

After thermal measurement, each ribbon sample was transferred using a sharp probe attached to a micromanipulator from the microheater device to a flat Si substrate and subject to atomic force microscopy (AFM, Bruker, Dimension Icon) studies using the tapping mode. Shown in **Figure 4.2** is the 3D profile of (a) a single Si nanoribbon without etching, (c) an etched double ribbon bundle with minimum air exposure (DN#3), (e) an etched double ribbon bundle stored in ambient

environment for 4 days (DN#7), and (g) an etched double ribbon stored in ambient environment for 60 days (DN#8).

From the AFM results, we can clearly see that in the double ribbon bundle, the two individual ribbons are aligned extremely well and overlap with each other nearly perfectly along the axial direction. This provides us a great platform to study the ballistic phonon transport behavior in vdW bonded double Si nanoribbons with an amorphous layer at the interface. To offset the effects of SiO_2 layers in the calculated silicon nanoribbon thermal conductivity, we used the thickness of the silicon core from the high resolution transmission electron microscopy (HRTEM) measurement and subtract the contribution of a-SiO_2 portion from the measured total thermal conductance based on the estimated a-SiO_2 thickness and the bulk thermal conductivity of a-SiO_2.

4.2 HRTEM Characterization of the Amorphous Layer at the interface

In order to understand phonon transport through the interface of vdW bonded Si nanoribbons with a layer of a-SiO_2 sandwiched in-between, it is important to know the thickness of the a-SiO_2 at the interface. This is shown with the HRTEM micrographs in **Figure 4.3**. For HRTEM characterization, the double ribbon samples were transferred from the thermal measurement device to copper grids. For some samples transferred to the Si substrate for AFM scanning or damaged during the transfer process, in order to ensure the same interface morphology as the sample subjected to thermal conductivity measurement, identical samples undergone exactly the same treatment were transferred to copper grids for detailed HRTEM examination.

We observed the interfacial region by manipulating the ribbon bundle using a sharp probe and aligning the ribbons so that the incident electron beam is parallel to the plane of interface, shown as a curved ribbon sitting on a carbon film in **Figure 4.3a**. In order to ensure the best view angle,

we scanned along the ribbon and selected the area where the measured ribbon thickness is closest to the measured data by AFM scanning.

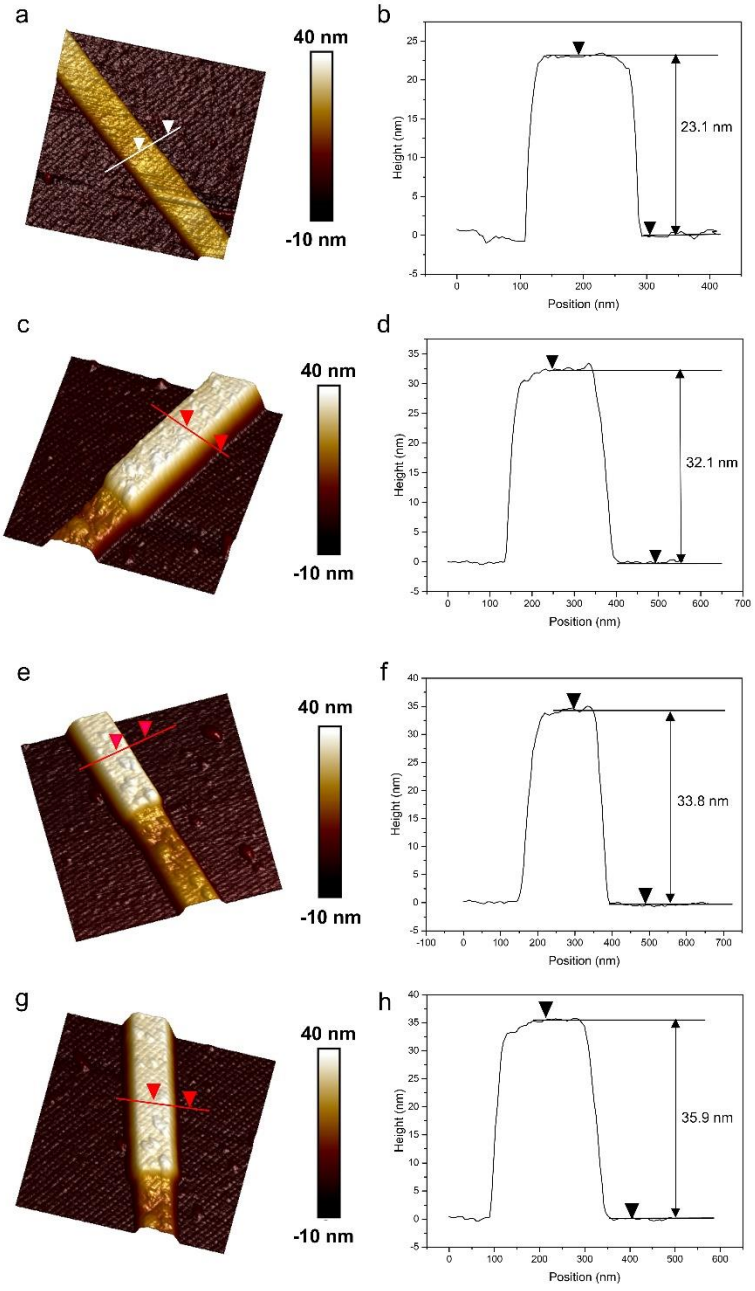

Figure 4.2 (a) AFM images for (a) a single Si nanoribbon without etching, (c) an etched double ribbon bundle with minimum oxygen exposure (DN#3), (e) an etched double ribbon bundle stored in ambient environment for 4 days (DN#7), and (g) an etched double ribbon bundle stored in ambient environment for 60 days (DN#8). (b, d, f, h) The corresponding line profiles along the lines labelled in (a, c, e, g).

Shown in **Figure 4.3b** is a double ribbon sample without buffered oxide etchant (BOE) etching (DN#1), where the Si core thickness of the single ribbon is measured to be 18.2 nm. Without etching, the single Si nanoribbon thickness measured from AFM in **Figure 4.2b** is 23.1 nm, which is very close to the HRTEM measured value after adding the 2.5 nm thick a-SiO_2 layer on the top and bottom surfaces. From **Figure 4.3b**, the interfacial a-SiO_2 layer thickness is also measured as 5.1 nm. These data indicate that the thickness of native oxide on the silicon nanoribbons without etching is 2.5 nm.

Figure 4.3d is the HRTEM image of the BOE etched double Si nanoribbon with minimum oxygen exposure (DN#4), where the interfacial a-SiO_2 layer was determined to be 1.7 nm. Meanwhile, the oxide layer thickness on the top/bottom surfaces is measured to be 1.2 nm. Thus, the oxide layer on the top/bottom surfaces is slightly thicker than the oxide at the interface for each ribbon, which is reasonable as oxidation rate should be quicker on top/bottom surfaces. If we add up the two Si nanoribbon core as well as the interfacial oxide layer thickness and a-SiO_2 layer on top/bottom surfaces, the total thickness is 32.3 nm. For the double ribbon with the same sample preparation process (DN#3), as shown in **Figure 4.2d**, the thickness of the ribbon bundle measured using AFM scanning is 32.1 nm. The 0.2 nm difference is within the measurement uncertainties of these precision instruments under the imaging condition.

Figure 4.3f shows the double ribbon sample etched with BOE and stored in ambient environment for 4 days, where the interfacial oxide layer thickness is measured as 3 nm. It can be seen that, compared with DN#4, the Si core thickness reduces from 14.1 nm to 13.2 nm after 4 day storage in the ambient. Also, from the HRTEM image, the oxide thickness on top/bottom surfaces is measured to be 2 nm. Thus, the total thickness of this ribbon bundle is 33.4 nm. As 1 nm thick silicon would grow into 2.17 nm oxide (Deal & Grove 1965), the a-SiO_2 layer thickness will

increase by 1.9 nm for each single ribbon, which is close to the increased oxide layer thickness measured from HRTEM (1.5 nm). Importantly, for the double ribbon with the same sample preparation process (DN#7), shown in **Figure 4.2f**, the total thickness of the ribbon bundle measured using AFM is 33.8 nm, which is consistent with our HRTEM measured value.

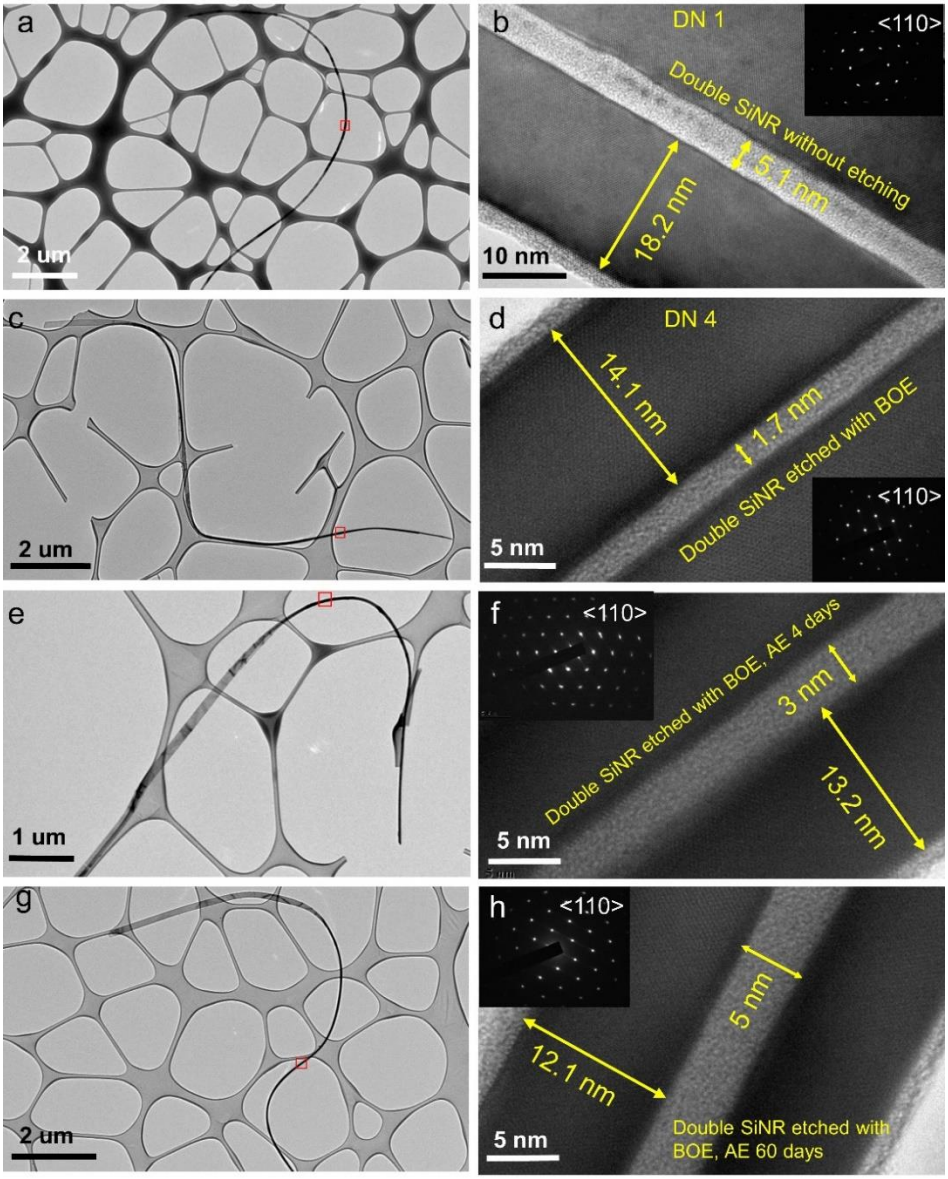

Figure 4.3 (a, c, e, g) Low magnification TEM images of different curved ribbon samples sitting on the carbon film. The red boxes indicate the twisted region of the ribbon, which is selected for HRTEM characterization. (b, d, f, h) HRTEM images showing the interfacial region of different ribbon samples. The insets show that all of the ribbons samples were patterned along <110> crystalline direction.

Figure 4.3h is the HRTEM image of the double ribbon sample stored in ambient environment for 60 days after BOE etching. The interfacial oxide layer thickness is measured as 5 nm while the core thickness is 12.1 nm. Compared with DN#7, the Si core thickness further reduced by 1.1 nm owing to surface oxidation. Meanwhile, after the long time ambient storage, the oxide thickness on top/bottom surfaces increased to 2.5 nm, which is close to that of the ribbon without BOE etching (DN#1). As such, the total thickness of the ribbon bundle measured from HRTEM is 34.2 nm. However, shown as the AFM scanning result of DN#8 in **Figure 4.2h**, which underwent the same sample preparation process, the measured height is 1.7 nm larger than the HRTEM measurement. We believe that this difference is probably caused by the non-optimal focusing during the HRTEM characterization, and thus the thickness measurement of this sample could carry slightly larger uncertainty.

4.3 Thermal Conductivity of Double Si Nanoribbons

For the thermal measurements, we first tested a double ribbon sample with native oxide on the surface (DN#1), i.e., a sample prepared without HF treatment. The thermal conductivity of all measured ribbon samples is extracted based on the dimension of the silicon ribbon core with the nominal contribution of the SiO_2 layers to the measured thermal conductance subtracted. As shown by the high resolution transmission electron microscopy (HRTEM) image in **Figure 4.4a**, the interfacial a-SiO_2 layer is about 5.1 nm thick. The obtained data (**Figure 4.5a**) indicate that the thermal conductivity of this double ribbon is approximately the same as that of a single ribbon, which has the same cross-sectional dimensions as each individual ribbon in the double ribbon sample. This is very different from the results for boron nanoribbons, where the thermal conductivity of double ribbon bundles is ~45% to ~70% higher than that of a single ribbon as temperature drops from 300 to 50 K (Yang et al. 2011b). There are two possible reasons for this

difference. One is the different interface morphology, which includes two aspects. (1) The interfacial adhesion energy of DN 1 could be low as no wetting process was involved in the sample preparation process; and (2), the thicker and denser oxide layer between the two silicon nanoribbons could diffusely scatter most phonons so a negligible amount of thermal phonons could penetrate through ballistically. The other possibility is that, because silicon has a much lower Debye temperature (~645 K) than boron (~2025 K) (Shanks et al. 1963, Yang et al. 2011b), phonons of the same energy have much shorter wavelengths in silicon and are scattered more strongly at the vdW interface between the two ribbons.

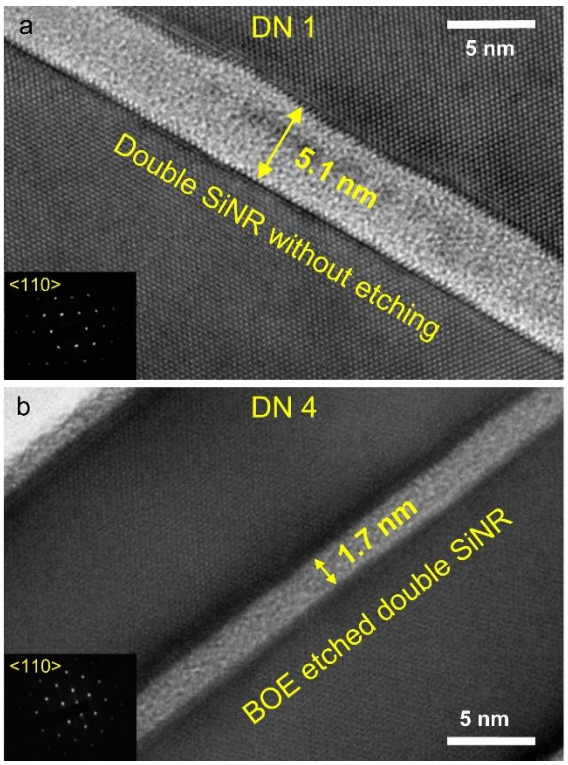

Figure 4.4 (a) An HRTEM micrograph of a double ribbon sample without BOE etching (DN#1), and the interfacial a-SiO_2 layer is measured as 5.1 nm thick. (b) An HRTEM image of a double ribbon after BOE etching and with minimum oxygen exposure (DN#4), where the interfacial a-SiO_2 layer is thinned to 1.7 nm. The insets show that all ribbons were patterned along <110> crystalline direction.

To determine which factor leads to the difference, we measured a double ribbon sample with enhanced adhesion energy. To do so, a well-aligned ribbon bundle (DN#2) was rinsed with deionized (DI) water and left at 450 K in vacuum for 24 h before thermal measurement. It has been demonstrated that for hydrophilic Si wafers annealed at a temperature higher than 150°C, hydrogen bonds will convert into covalent siloxane bonds as depicted by the inset in **Figure 4.5a**, which leads to an interfacial bonding energy of up to 1200 mJ/m^2 (Tong et al. 1994). As shown in **Figure 4.5a**, this treatment boosted the thermal conductivity of sample DN#2 to a value significantly higher than that of DN#1 (11% higher at 300 K). Here, the enhancement is defined as $(k_{double} - k_{single})/k_{single}$, where k_{double} and k_{single} represent the measured thermal conductivities of double ribbon bundles and corresponding single ribbons, respectively. This observation is not as expected since it has been argued that the thermal conductivity of a-SiO_2 remains bulk-like even as the film thickness is reduced to 3 nm (Braun et al. 2016), and that propagons only contribute <6% to the thermal conductivity of a-SiO_2 (Larkin & McGaughey 2014). Our results, however, clearly demonstrate that thermal phonons can ballistically penetrate through over 5 nm thick a-SiO_2 films, as shown schematically in **Figure 4.1c**.

With the effects of interfacial bonding strength confirmed, we now examine how oxide layer thickness affects phonon transport in double ribbon bundles. As described previously, we can vary the a-SiO_2 thickness between the two ribbons through HF etching and re-oxidation for different periods in ambient environment. For BOE treated silicon surface, it has been shown that the surface dangling bonds are terminated by hydrogen and fluorine atoms (Ljungberg, Karin, Anders Söderbärg 1993, Schroeder et al. 2015, Tong et al. 1997, 2003). The subsequent reagent alcohol rinsing and bonding under high vacuum condition caused the surface remain hydrophobic (Jerez-Hanckes et al. 2003).

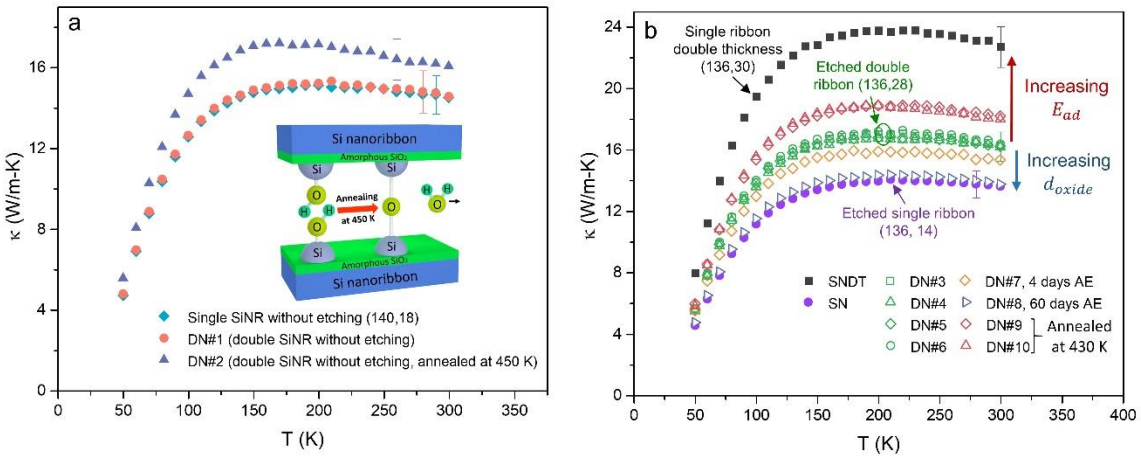

Figure 4.5 (a) Measured thermal conductivity of double Si nanoribbon and single ribbon without BOE etching, as well as a non-etched double ribbon annealed at 450 K. The legend indicates that the silicon core is 140 nm wide and 18 nm thick after subtracting the 2.5 nm thick a-SiO_2 layer on each surface. The inset depicts the formation of covalent siloxane bonds upon high temperature annealing. (b) Measured thermal conductivity of BOE etched double Si nanoribbon samples with various interfacial a-SiO_2 thickness and interfacial adhesion energy. Along with the double ribbons are the measured thermal conductivity of a BOE etched single ribbon as well as a single nanoribbon of double thickness. AE stands for ambient environment, and DN#7&8 are double ribbons stored in ambient for 4 and 60 days after BOE etching.

To better evaluate the thermal conductivity enhancement for the etched double ribbon samples, we also prepared and measured the thermal conductivity of a single Si nanoribbon processed with the same etching procedure. To demonstrate the repeatability, we measured four double ribbon samples (DN#3-6) right after they are processed with HF etch, which yielded essentially identical results, and are considerably higher than that of the single ribbon, as shown in **Figure 4.5b**. The HRTEM micrograph of the interface of these double ribbon samples is shown in **Figure 4.4b**, which displays an a-SiO_2 layer thickness of 1.7 nm, about one-third of the a-SiO_2 thickness in the non-etched sample. The enhanced thermal conductivity of DN#3-6 clearly indicates that a portion of thermal phonons could ballistically penetrate through the vdW interface within 1.7 nm thick oxide layer, which leads to an extended effective phonon MFP in the double ribbon bundles.

To further explore the effects of a-SiO_2 thickness on ballistic phonon transmission through the vdW interface, we left double ribbon samples in ambient conditions for various periods for oxide growth. For sample DN#7, which was left in ambient environment for 4 days, the measured oxide thickness is ~3 nm, and for sample DN#8, which was left in ambient for 60 days, the oxide thickness is 5 nm, the same as that for the non-etched double ribbon sample. The measured data for these samples are also shown in **Figure 4.5b**; and the thermal conductivity for DN#7 is lower than that of DN#3, but still higher than that of the single ribbon. For sample DN#8, the thermal conductivity is essentially the same as that of the single ribbon.

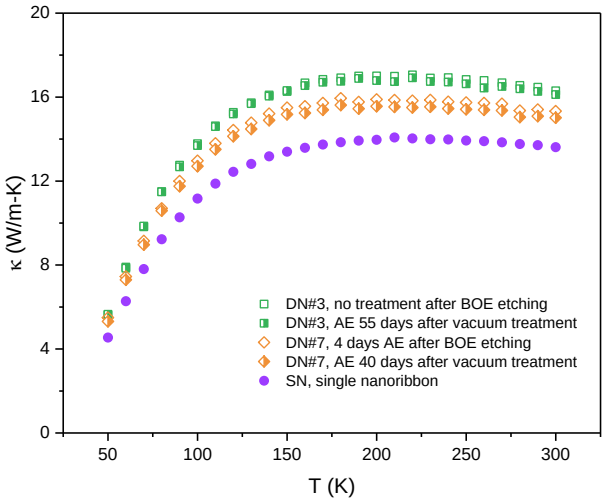

Figure 4.6 Comparison of measured thermal conductivity of double Si nanoribbons before and after various time of atmospheric environment (AE) storage after high vacuum treatment.

An interesting observation is that if we put a double ribbon sample in high vacuum (<10^{-6} mbar) for 24 h, then no further oxidation could occur at the interface even we put the sample back into ambient environment. This is evidenced by the fact that the thermal conductivity of the ribbon bundle, post the high vacuum process, does not show any further decrease even after being left in ambient for >40 days, as shown in **Figure 4.6**. We attribute this to that under the high vacuum, any residual volatile species between the two ribbons will be pumped out of the interface and the

vdW interface becomes gas tight. Previous work on Si wafer bonding experiments showed that in low vacuum condition (a few mbar), the bonding energy for Si wafer pairs significantly increases when compared with the bonding performed in ambient condition (Gösele et al. 1999), and the fracture surface energy can reach 3000 mJ/m^2 at an annealing temperature as low as 150°C (Tong 1999). In fact, nanogaps inevitably exist at the interface due to the surface imperfections, leaving room for trapped gas, which prevents intimate contact between the two surfaces. By treating the double ribbon sample in a high vacuum condition, the trapped gas or volatile residual can be pumped out from the interface. As a result, the interface become gas tight and resistive to further oxidation process. Therefore, the a-SiO_2 layer at the interface will not grow further even after stored in ambient environment for very long time.

Annealing at elevated temperature has also been shown as an effective approach to increase the interfacial adhesion energy for silicon wafers with hydrophobic surfaces (Cha et al. 1994, Tong et al. 1994). To examine if annealing can influence ballistic phonon transport in ribbon bundles with hydrophobic interfaces, we treated HF-etched double ribbon samples in high vacuum and 430 K for 24 h. The measured thermal conductivity of annealed samples (DN#9-10) is further enhanced compared with the ribbon bundles prepared at 300 K (DN#3-6), as shown in **Figure 4.5b**. The further enhanced thermal conductivity for DN#9-10 is because for HF-treated Si surfaces, the surface terminating H is more stable in monohydrides (Si-H) than in dihydrides (Si-H_2); and if annealed at a temperature beyond 150ºC, conversion of Si-H_2 to Si-H results in an increased polarity of the hydride, leading to stronger hydrogen bonding between the surfaces (Cha et al. 1994, Tong et al. 1994). The results of all measured ribbons samples are summarized in Table 1 for comparison.

Table 1. Summary of sample configurations, measured thermal conductivity and enhancement, and extracted interfacial parameters for single and double Si nanoribbons at 300 K.[a]

	Sample #	Oxide thickness (nm)	κ at 300 K (W/m-K)	κ enhancement at 300 K (%)	Adhesion energy (mJ/m^2)	Transmission coefficient at 300 K
Hydrophilic interface	DN#1	5.1	14.6 (±0.92)	0.7		
	DN#2	5.1	16.1 (±1.14)	11	1200*	0.19
	SN		14.5 (±0.95)			
Hydrophobic interface (BOE etched)	DN#3-6	1.7	16.3 (±1.27)	22	115	0.38
	DN#7	3	15.3 (±1.15)	14	85	0.25
	DN#8	5	13.7 (±0.89)	2	25	0.04
	DN#9-10	1.7	17.6 (±1.25)	31	360	0.55
	SN		13.4 (±0.88)			

[a]DN denotes a double Si nanoribbon, and SN denotes a single Si nanoribbon. The interfacial oxide thickness is measured from high resolution transmission electron microscopy (HRTEM). The uncertainty in κ is determined using the method described in Section IV of the Supporting Materials.

*The interfacial adhesion energy is adopted from the Si wafer bonding experiments under the same processing conditions (Tong et al. 1994).

To evaluate the upper limit of the double ribbon thermal conductivity, we also measured the thermal conductivity of a single ribbon of double thickness. In the classical size effect regime, the phonon MFP suppression caused by phonon boundary scattering in thin films and wires are well described by the Fuchs–Sondheimer reduction function (Chambers 1950, Sondheimer 1952), and for a ribbon of double thickness, the theoretical thermal conductivity enhancement is estimated as ~55% at 300 K, which is much less than the experimentally observed ~72% as shown in **Figure 4.5b**. We attribute this difference to the recently discovered acoustic softening effects in thin Si nanoribbons (Yang et al. 2016).

Since the thickness of the measured silicon ribbons is only ~14 nm after HF etching, the effects of a reduced Young's modulus and acoustic softening have to be considered (Wingert et al. 2015, Yang et al. 2016). For the Young's modulus measurement, the measured nanoribbon samples (DN 5&6) were transferred from the thermal measurement device to an 8 μm wide Si trench, and a layer of Pt was locally deposited using electron beam induced deposition (EBID) to clamp both ends of the ribbon sample. Before each measurement, the sensitivity of the cantilever was calibrated by tapping it on the hard Si substrate and the spring constant was extracted through a thermal tune process. By scanning the Si nanoribbon using AFM, we could locate its midpoint across the trench. We then performed a bending test by pressing the AFM tip at the midpoint to obtain a force-deflection (F−D) curve. The Young's modulus of the Si core was extracted by fitting the F−D curve through a core-shell model (Bellan et al. 2005, Calahorra et al. 2015, Yang et al. 2016). Shown in **Figure 4.7**, the measured Young's modulus for the etched single and double Si nanoribbons are 103 and 97 GPa, respectively, which are much smaller than the bulk value (Calahorra et al. 2015). Importantly, the measured values are consistent with our previous measurement on single Si nanoribbons (Yang et al. 2016), which follow the general trend of decreasing values with increasing surface-area-to-volume ratio.

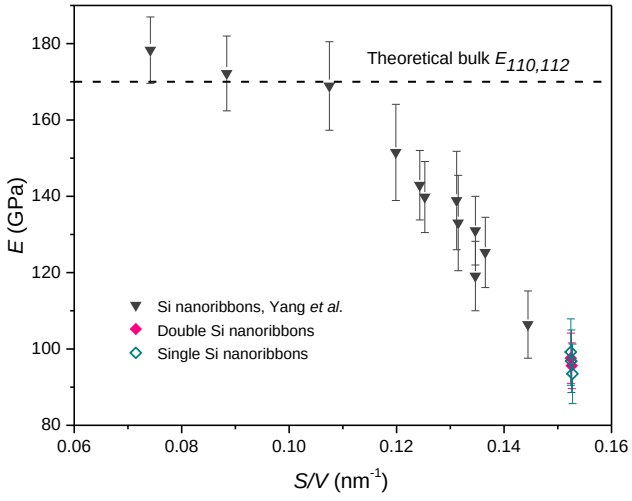

Figure 4.7 Measured Young's modulus of the etched double Si nanoribbons in comparison to that of single Si nanoribbons plotted against the surface-area-to-volume ratio (*S/V*) (Yang et al. 2016).

This reduced Young's modulus would lead to reduced thermal conductivity as the speed of sound is related to the Young's modulus according to $v = \sqrt{E/\rho}$, where E and ρ are the Young's modulus and density, respectively (Yang et al. 2016). Meanwhile, for the single ribbon of double thickness, its Young's modulus is the same as bulk value (Yang et al. 2016); and therefore, other than the classical size effect, the experimentally measured enhancement for the single ribbon of double thickness involves additional contribution from the enhanced elastic stiffness.

4.4 Phonon Penetration Depth in a-SiO_2

To quantitatively understand phonon transport in double ribbon samples prepared under different conditions, we plot the calculated thermal conductivity enhancement in **Figure 4.8a**. For all five groups of samples the enhancement increases as the temperature is reduced, which can be attributed to the higher transmissivity of longer wavelength phonons that are more important at low temperature. For non-annealed samples with 1.7 nm thick oxide (DN#3-6), the thermal conductivity enhancement is ~22% at 300 K. Annealing at 430 K for 24 h boosts the enhancement from 22% to 31%, indicating that a higher adhesion energy at the vdW interface results in a higher transmission coefficient (Losego et al. 2012, O'Brien et al. 2013). On the other hand, as the interfacial a-SiO_2 layer thickness increases from 1.7 nm to 5 nm (DN#3, 7&8), the thermal conductivity enhancement decreases from 22% to 2% at 300 K, while for sample DN#2 with 5.1 nm thick oxide layer but much enhanced adhesion energy, its room temperature thermal conductivity is still 11% higher than that of a single ribbon. These observations collectively suggest that both the oxide layer thickness and the vdW interfacial adhesion energy play important roles in determining ballistic phonon transmission coefficient through the interface.

The spectral phonon transmissivity $t_{\omega,j}$ based on the modified acoustic mismatch model (vdW-AMM) can be written as (Prasher 2009):

$$t_{\omega,j} = \frac{1}{1+\left(\omega_j^{\,2}/4K_A^{\,2}\right)z_j^{\,2}\cos^2\theta}, \tag{4.1}$$

where ω_j is the phonon angular frequency; z_j is the acoustic impedance and is equal to the product of density and phonon group velocity, ρv; j represents different phonon modes; θ is the angle between the interface normal and the phonon propagation direction; and K_A is the spring constant per unit area, which is related to the interfacial adhesion energy E_{ad}, shown as below. Equation (4.1) indicates that the phonon transmission coefficient across the vdW interface decreases as ω increases.

For a pair of atoms interacting through vdW force, the widely used Lennard-Jones potential can be adopted to describe the potential energy, which is given as (Prasher 2009, Schroeder et al. 2015, Yang et al. 2011b):

$$\phi(r) = 4\varepsilon\left[\left(\frac{\sigma}{r}\right)^{12} - \left(\frac{\sigma}{r}\right)^{6}\right], \tag{4.2}$$

where ε is the parameter determining the depth of the potential well and σ is a length scale parameter determined by $\sigma = 2^{-1/6}r_0$, where r_0 is the average distance between nearest-neighbor atoms. Under the harmonic approximation, the spring constant K between a pair of atoms can be expressed as

$$K = \left(\frac{\partial^2\phi}{\partial r^2}\right)_{r=r_0} = \frac{72\varepsilon}{2^{1/3}\sigma^2}. \tag{4.3}$$

In the model described below to fit the thermal conductivity enhancement of the vdW force bonded double Si nanoribbons, the spring constant per unit area K_A is used as a fitting parameter

to characterize the interfacial bonding strength. It is related to K as $K_A = nK$, where n is the number of surface atoms per unit area. Exact information about the surface atoms is needed in order to know n, which is rarely available (Prasher 2009). Therefore, n is approximated as $1/{a_p}^2$, where a_p is the dimension of primitive unit cell.

The Hamaker constant, H, is defined as $H = 4\varepsilon\pi^2 N^2 \sigma^6$, where N is the atom number density, and H is related to the interfacial adhesion energy per unit area, E_{ad}, as

$$H = 16\pi {z_0}^2 E_{ad}, \tag{4.4}$$

where z_0 is the equilibrium distance between two surfaces, expressed as $z_0 = (2/15)^{1/6}\sigma$. By combining the above equations, we can calculate the interfacial adhesion energy using the fitted spring constant per unit area, K_A.

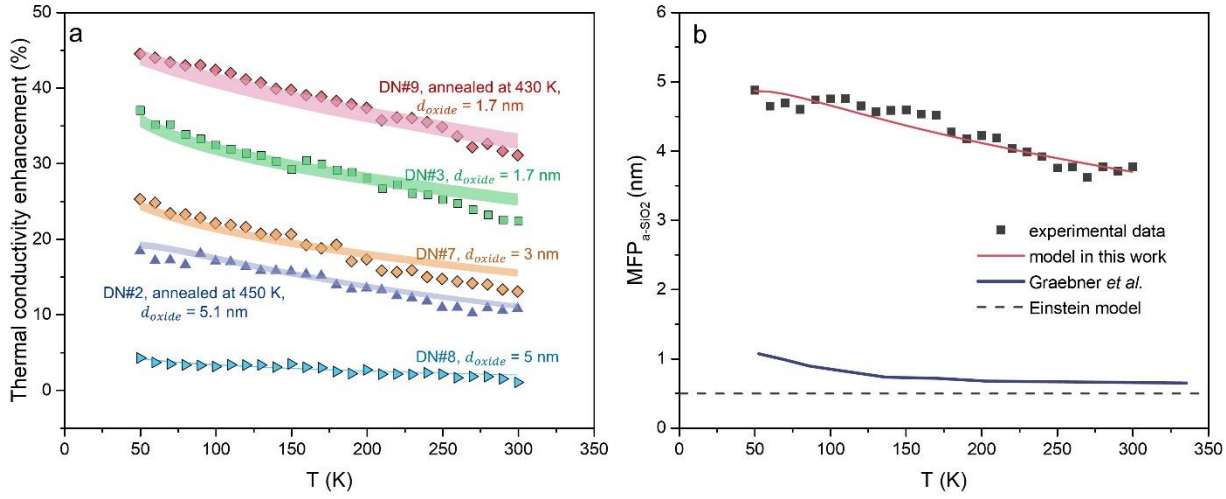

Figure 4.8 The measured thermal conductivity enhancement along with the fitted results of double Si nanoribbons with various oxide layer thicknesses and different interfacial adhesion energy values. (b) The calculated phonon MFP in a-SiO_2, l_{a-SiO_2}, based on the measured thermal conductivity enhancement of DN 2 are plotted along with the fitted results in temperature range of 50-300 K. The fitted l_{a-SiO_2} using the bulk a-SiO_2 thermal conductivity (Graebner et al. 1986) as well as phonon MFP based on Einstein model (Einstein 1911) are also plotted in comparison with the results from this work.

In addition to disturbance from the vdW force, the interfacial a-SiO_2 layer can also diffusely scatter phonons. A simple model for the scattering probability can be written as $1-$

$e^{-\frac{d}{cos\varphi}/l_{a-SiO_2}}$(Chambers 1950, McGaughey & Jain 2012), where d is the oxide thickness; φ is the angle between the interface normal direction and the phonon propagation direction in the a-SiO_2 layer, and l_{a-SiO_2} is the temperature dependent phonon ballistic penetration depth or MFP in a-SiO_2. According to Snell's law, if the direction of the incident phonon from Si ribbon is θ, the refracted phonon direction inside the oxide layer is determined by $sin\varphi = \frac{v_{a-SiO_2}}{v_{SiNR}} sin\theta$, where v_{SiNR} and v_{a-SiO_2} are the speed of sound in Si nanoribbon and a-SiO_2, respectively(Wolfe 2005). v_{SiNR} can be calculated as $v_{SiNR} = \sqrt{E_{SiNR}/\rho_{Si}}$, where E_{SiNR} is the measured Young's modulus, and ρ_{Si} is density of Si. For a-SiO_2, previous measurements show that its Young's modulus remains bulk-like even when the critical dimension reduces to 7.5 nm (Wingert et al. 2016a), and thus we use bulk values to calculate v_{a-SiO_2}.

As to the Si/a-SiO_2 interfaces, wave packet simulations have shown that for phonons of lower than 1 THz frequencies, their transmission coefficients at the interface are 0.98 and 0.95 for longitudinal and transverse phonon branches, respectively (Liang & Keblinski 2016, Liang et al. 2017). These results are comparable with the predictions from the acoustic mismatch model (AMM), which yields the transmission coefficients for longitudinal and transverse phonons as 0.98 and 0.94, respectively (Liang & Keblinski 2016). As such, in our model, we approximate the phonon transmission coefficient at the Si/a-SiO_2 interface as unity and combine its effects into the transmission through the vdW interface by adjusting the fitting parameter, K_A in Equation (4.1).

The mode dependent hemispherical transmissivity ratio ($\Gamma_{r,j}$), representing the portion of all incident phonons on the composite interface that are ballistically transmitted, can be expressed as:

$$\Gamma_{r,j} = \frac{\int_0^{\omega_{m,j}} \int_0^{\theta_c} C_{\omega,j} v_{\omega,j} t_{\omega,j} \sin\theta \cos\theta \times e^{-\frac{d}{\cos(\arcsin(v_{a-SiO_2}/v_{SiNR}\sin\theta))}/l_{a-SiO_2}} d\theta d\omega}{\int_0^{\omega_{m,j}} \int_0^{\theta_c} C_{\omega,j} v_{\omega,j} \sin\theta \cos\theta \, d\theta d\omega}, \qquad (4.5)$$

where $\omega_{m,j}$ is the maximum angular phonon frequency, $C_{\omega,j}$ is the frequency dependent heat capacity per unit volume, and θ_c is the critical angle (which is $\pi/2$ as the speed of sound in Si is higher than in a-SiO_2). The full dispersion relation of bulk Si is adopted in the model (Brockhouse 1959), and acoustic softening effect is taken into account multiplying both the phonon frequency and phonon group velocity using a scaling factor as $\sqrt{E/E_{bulk}}$ (Yang et al. 2016). Thus, based on Equation (4.5), the thermal conductivity enhancement for double silicon nanoribbon bundles can be expressed as

$$\left(\kappa_{double} - \kappa_{single}\right) / \kappa_{single} = \Gamma_r \left(\alpha - 1\right), \tag{4.6}$$

where Γ_r is the average of the ballistic transmission coefficients for the three different acoustic phonon branches, and α is the thermal conductivity ratio of single ribbon of double thickness to that of a single ribbon, which is calculated based on the Fuchs-Sondheimer reduction function.

The two key parameters determining the ballistic phonon transmission coefficient through the interface are the spring constant per unit area at the vdW interface, K_A, and the phonon ballistic penetration depth or MFP in a-SiO_2, l_{a-SiO_2}. However, for sample DN#2, the high adhesion energy leads to a ballistic phonon transmission coefficient at the vdW interface of approximately unity (Prasher 2009). Thus, the thermal conductivity enhancement for DN#2 is dominated by only one parameter, l_{a-SiO_2}. Therefore, using Equation (4.5) and (4.6), we can extract the phonon MFP in the sandwiched a-SiO_2 layer by fitting the thermal conductivity enhancement for sample DN#2, which reduces from 4.9 to 3.7 nm as the temperature rises from 50 to 300 K, as shown in **Figure 4.8b**.

As mentioned previously, the Einstein random walk model suggests an MFP of ~0.5 nm for vibrations in a-SiO_2 (Einstein 1911). This very short MFP is obtained based on a gray model, and

if more detailed analysis considering the frequency-dependent transport, a MFP of ~1.1 nm was extracted at 50 K based on bulk a-SiO_2 thermal conductivity (Graebner et al. 1986). However, this study clearly shows that phonons can ballistically propagate much longer in a-SiO_2, at least in the case when the oxide films are in contact with crystalline materials. In fact, it is remarkable to see the 11% thermal conductivity enhancement for the double ribbon with an interfacial oxide thickness of 5.1 nm, which corresponds to the ballistic phonon transmission coefficient of 19%.

We point out that ballistic phonon transport or propagon contribution to thermal conductivity in amorphous materials highly depends on materials type. For example, it has been recently shown that for amorphous silicon, heat-carrying propagons can transport ballistically up to 10 μm.(Kwon et al. 2017) On the other hand, studies of other types of amorphous materials, such as copper phthalocyanine (CuPc) (Jin et al. 2012) and poly(3-hexylthiophene) (P3HT) (Duda et al. 2013), which are widely used in photovoltaic and thermoelectric applications, indicate that thermal transport are dominated by diffusons. In addition, the phonon MFP of amorphous indium–gallium–zinc oxide (a-IGZO) films (Yoshikawa et al. 2013), a high performance channel material for thin-film transistors (TFTs) was claimed to be 0.35 nm (Yoshikawa et al. 2013), comparable to the distance of neighboring In–In atoms (0.33 nm) (Nomura et al. 2007).

With the phonon MFP in a-SiO_2 determined, we fit the thermal conductivity enhancement of etched double ribbons with various interfacial conditions. Now the only fitting parameter is the spring constant per unit area, K_A. As shown in **Figure 4.8a**, by varying K_A, the fitting result can capture both the trend and magnitude of the thermal conductivity enhancement remarkably well in the whole temperature range. The thickness of the fitting line in **Figure 4.8a** represents the range when a ± 0.1 nm uncertainty is considered for the measured oxide thickness. The extracted adhesion energy (E_{ad}) at the vdW interfaces is 360, 115, 85, and 25 mJ/m^2 for the samples that are

annealed at 430 K (DN#9&10), measured directly after etching (DN#3-6), left 4 days in ambient (DN#7), and left 60 days in ambient (DN#8), respectively. Importantly, the fitted E_{ad} are in good quantitative agreement with the reported values from Si wafer bonding experiments (Jerez-Hanckes et al. 2003, Tong 1999, Tong et al. 1994). For hydrophobic Si wafers rinsed with alcohol and left in an ambient environment until the interface is fully oxidized, the bonding energy was determined to be 30 mJ/m^2 (Jerez-Hanckes et al. 2003), which is very close to that of sample DN 8 in this work. In addition, it has been shown that annealing at elevated temperature or vacuum condition could significantly increase the adhesion energy (Tong 1999, Tong et al. 1994), especially for alcohol treated Si wafers, where evaporation of alcohol could pull two surfaces into intimate contact (Jerez-Hanckes et al. 2003). Thus, for DN#3-7, 9&10, the interfacial adhesion energies are much higher than 30 mJ/m^2. To illustrate the effects of the adhesion energy and the oxide thickness, we plot a contour map in **Figure 4.9**, which presents the calculated room temperature phonon ballistic transmission coefficient as a function of both E_{ad} and d_{oxide}. The circles in the contour denote the fitted E_{ad} based on the measured oxide layer thickness d_{oxide} and the thermal conductivity enhancement.

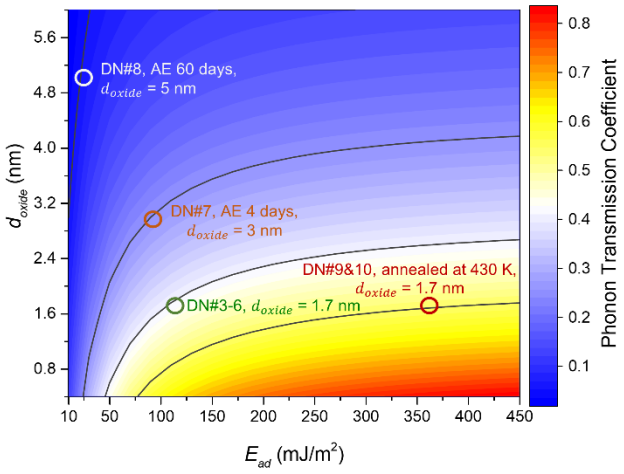

Figure 4.9 The calculated room temperature phonon ballistic transmission coefficient of double

Si nanoribbons versus the interfacial a-SiO_2 layer thickness, d_{oxide}, and the interfacial adhesion energy, E_{ad}. According to the experimentally measured thermal conductivity enhancement of eight different double ribbon samples (DN#3-10) as well as the interfacial oxide thickness measured from HRTEM, the interfacial adhesion energy can be directly fitted from the contour, shown as the different circles.

4.5 Summary

In summary, measurements of the in-plane thermal conductivity of double Si nanoribbons stuck together through vdW interfaces with a layer of oxide in-between disclose a ballistic phonon penetration depth that is nearly one order of magnitude higher than the prediction of amorphous limit model. Interesting effects of various interface treatment on phonon transport through the interface have been demonstrated. This study should help to conclude the lasting debate of ballistic phonon penetration depth in a-SiO_2 and provide important insights into thermal management of nanoelectronic devices. To further understand the phonon transport dynamics in a-SiO_2 layers, more strict theoretical analysis with less assumptions could be carried out, and double ribbons of systematically varied thickness could also be studied.

Chapter 5

Distinct Signatures of Electron-Phonon Coupling Observed in the Lattice Thermal Conductivity of $NbSe_3$ Nanowires

The interaction between electrons and phonons is a fundamental process in solids, and it plays critical roles in various physical phenomena, such as superconductivity (Lanzara et al. 2001), hot carrier transport (Herring 1954), and charge density waves (Peierls 1955, Xi et al. 2015). Indeed, e-ph scattering is a major mechanism of electrical resistance (Ziman 1960); and the effects of e-ph interactions on electronic properties of condensed matters have been extensively studied (Lundstrom 2009, Ziman 1960). However, while it is widely speculated that e-ph scattering could also affect lattice thermal conductivity (Butler & Williams 1978), its contribution is still in debate and quantitative analyses have been largely lacking until recently.

The major challenge in understanding how e-ph interactions contribute to thermal conductivity lies in the either electron- or phonon-dominant thermal transport. For normal metals with typical carrier concentrations greater than 10^{22} cm^{-3}, phonons contribute less than 10% to the total thermal conductivity at all temperatures (Liao et al. 2015). While for semiconductors and insulators, phonons are the predominant heat carriers, and the effect of e-ph scattering is often neglected. However, it has recently been suggested that in various technically important materials, e-ph interactions can significantly reduce lattice thermal conductivity, which are attracting attention to the quantitative analyses of the e-ph coupling effect (Holland 1964, Jain & McGaughey 2016, Liao et al. 2015, 2016; Morelli et al. 1993, Wang et al. 2016, Zheng et al. 2017).

Attempts have been made earlier to measure the thermal conductivity of heavily doped semiconductors and investigate the effects of e-ph coupling on lattice thermal conductivity (Holland 1964, Morelli et al. 1993); however, due to the inherent complexity of phonon scattering

process involving multiple scattering mechanisms, it is extremely challenging to distinguish the contribution of e-ph scattering from other scattering mechanisms, especially at elevated temperatures. As such, the analyses tend to be qualitative. More recently, using a three-pulse femtosecond photoacoustic technique, Liao et al. measured the scattering rate of the 250 GHz phonons in Si membrane to quantify the e-ph interactions on phonon transport (Liao et al. 2016). However, the study is restricted to monochromatic phonons and it also remains unclear whether the dynamically pumped electron-hole pairs have the same phonon scattering rate as normal electrons. To avoid the challenge of experimentally extracting the effects of e-ph scattering, first-principles calculations have been conducted on metals and heavily doped semiconductors (Jain & McGaughey 2016, Liao et al. 2015, Wang et al. 2016). Although recent predictions (Jain & McGaughey 2016, Wang et al. 2016) both pointed out the significance of e-ph scattering on lattice thermal conductivity in some metals, discrepancies do exist between calculations such as for a normal metal Al: while Wang et al. (Wang et al. 2016) suggested that e-ph interactions only led to marginal difference, Jain and McGaughey (Jain & McGaughey 2016) predicted that e-ph scattering could lead to ~20% drop to the Al lattice thermal conductivity. Moreover, Liao et al. (Liao et al. 2015) claimed that up to ~45% reduction of lattice thermal conductivity could be induced by e-ph scattering in heavily-doped silicon, which has been overlooked in most previous studies.

To reconcile these discrepancies, experimental evidence for the contribution of e-ph interactions to lattice thermal conductivity has to be obtained. However, without a distinct signature such as the T^{-1} temperature dependence for Umklapp scattering, it is extremely difficult to distinguish the effects of e-ph interactions from other factors such as defect scattering. In this chapter, we report such distinct signatures of e-ph coupling in lattice thermal conductivity

observed with niobium triselenide ($NbSe_3$) nanowires, which clearly demonstrates the importance of e-ph scattering in lattice thermal conductivity.

$NbSe_3$ belongs to a class of van der Waals (vdW) materials with quasi-one-dimensional (quasi-1D) crystal structures, where covalently-bonded molecular chains are assembled together *via* vdW force. Owing to the restricted dimensionality, the density of free electrons in $NbSe_3$ spontaneously develops a wave-like variation when temperature drops below a critical value (T_{CDW}), which is called charge density waves (CDWs) (Grüner 1988, Peierls 1955, Zhu et al. 2015). The variation of charge carrier concentration upon the onset of CDW modulates the e-ph scattering strength, resulting in unique features in the lattice thermal conductivity.

5.1 $NbSe_3$ Nanowire Sample Preparation

Multi-millimeter long ribbon-like $NbSe_3$ crystals were grown by chemical vapor transport (CVT) method (Liu et al. 2016, Zhang et al. 2018). The mixture of Nb and Se powders in a ratio of 1 : 3.03 was ground to be uniform before loaded into a quartz tube, which was then sealed under vacuum. To grow single crystals, the sealed tube was heated to 800^{o}C and 700^{o}C at the charge and cold end, respectively, in a horizontally placed double zone furnace. After two weeks, $NbSe_3$ crystals formed at the charge end or in the middle of the quartz tube.

The monoclinic room-temperature structure of $NbSe_3$ is depicted in **Figure 5.1**. $NbSe_3$ contains three types of metallic chains (**Figure 5.1b**) according to the strength of the chalcogen-chalcogen bonds in the unit cell. The type-III chains are responsible for the first CDW below T_{CDW1} = 145 K and the type-I chains contribute to the second modulation below T_{CDW2} = 59 K, whereas the type-II chains remain metallic at all temperatures (Van Smaalen et al. 1992). Therefore, $NbSe_3$ does not develop a complete gap at the Fermi level, but remains partially metallic at low temperature (Van Smaalen et al. 1992).

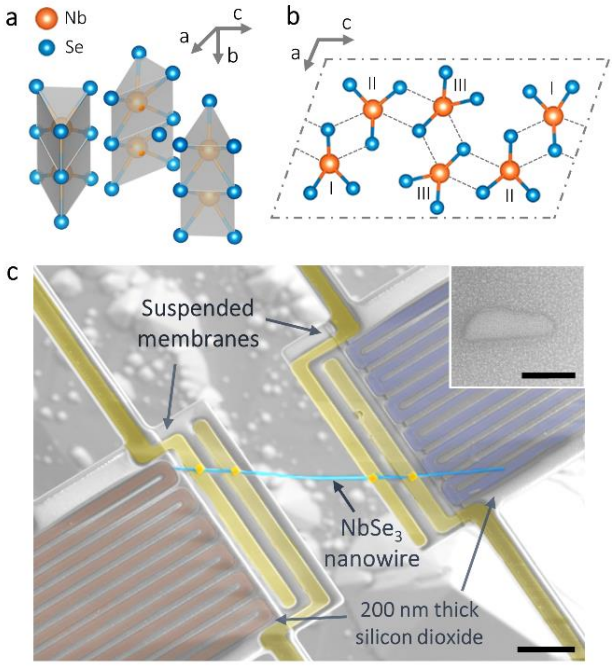

Figure 5.1 Crystal structure of $NbSe_3$ and the suspended microdevice for thermal/electrical measurements. (a) Schematic diagram showing the stacking of the prisms along the *b* axis in $NbSe_3$. (b) A projection of the crystal structure perpendicular to the *b* axis. (c) False-color SEM micrograph showing the measurement device with a $NbSe_3$ nanowire. Pt/C was locally deposited *via* electron-beam induced deposition at the contacts between the nanowire and the four electrodes to enhance thermal/electrical contact. 200 nm thick silicon dioxide covers the Pt serpentine coils on both membranes. (Inset) An SEM image of the cross section of a $NbSe_3$ nanowire. Scale bars: 4 μm (main panel); 100 nm (inset).

$NbSe_3$ nanowires were prepared from bulk crystals using ultrasonic cleaving, and even though the bonding energies along *b*- and *c*-directions in $NbSe_3$ are comparable (Table I), the Nb-Se bonds formed along *c*-direction vary significantly in the bond length (2.73 to 2.95 Å), which results in an easy cleavage (Hodeau et al. 1978). **Figure 5.2** shows a high-resolution transmission electron microscopy (HRTEM) image of an as-prepared $NbSe_3$ nanowire, where the well-aligned molecular chains can be clearly identified and the diffraction pattern shown in the inset indicates the single crystalline nature.

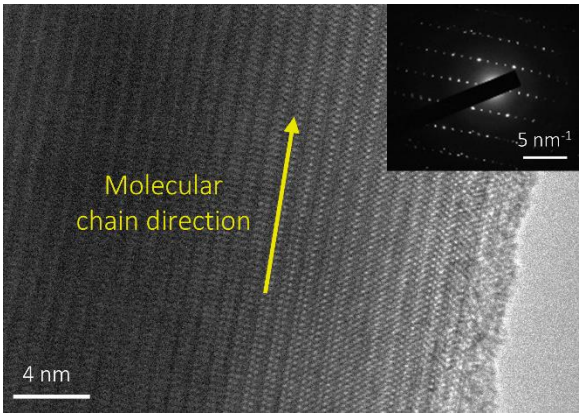

Figure 5.2 An HRTEM micrograph showing the perfectly aligned molecular chains. The diffraction pattern in the inset indicates the single crystalline nature of the as-prepared $NbSe_3$ nanowires.

We measured the electrical and thermal conductivities, as well as Seebeck coefficients of the $NbSe_3$ nanowires using a well-established approach (Shi et al. 2003, Wingert et al. 2012, Zhang et al. 2017). As shown in **Figure 5.1c**, a nanowire is placed between two suspended SiN_x membranes with integrated Pt heaters/resistance thermometers and extra electrodes. For quasi-1D nanowires prepared *via* ultrasonic exfoliation, the cross-sections tend to be of irregular shapes, which we examine directly by cutting open the cross-section using focused ion beam (inset in **Figure 5.1c**) (Zhang et al. 2018).

To obtain the exact cross-sectional area of each tested sample, as shown in **Figure 5.3a**, a $NbSe_3$ nanowire was transferred from the measurement device to a pre-cut piece of Si wafer, with the wire aligned perpendicularly to the edge. Then, a Pt/C composite layer was deposited on top of the nanowire *via* electron beam induced deposition (EBID) as a protection layer, and a focused ion beam (FIB) was used to etch away the part shown in the yellow box, cutting open the cross-section of the nanowire. The final step was to mount the Si piece vertically on an SEM stub for direct observation of the cross section. As shown in **Figure 5.3b**, through imaging with high resolution scanning electron microscopy (HRSEM, Zeiss Merlin), we are able to obtain both the

perimeter (P) and area (A) of the cross section for the examined sample. The hydraulic diameter is then calculated as $D_h = 4A/P$, which is four times of the reciprocal of the surface-area-to-volume ratio (S/V). It has been shown that the hydraulic diameter (D_h), which is four times of the reciprocal of the surface-area-to-volume ratio (S/V), better characterizes the classical size effects in nanowires (Yang et al. 2016, Zhang et al. 2018); and here we use D_h to define the nanowire size.

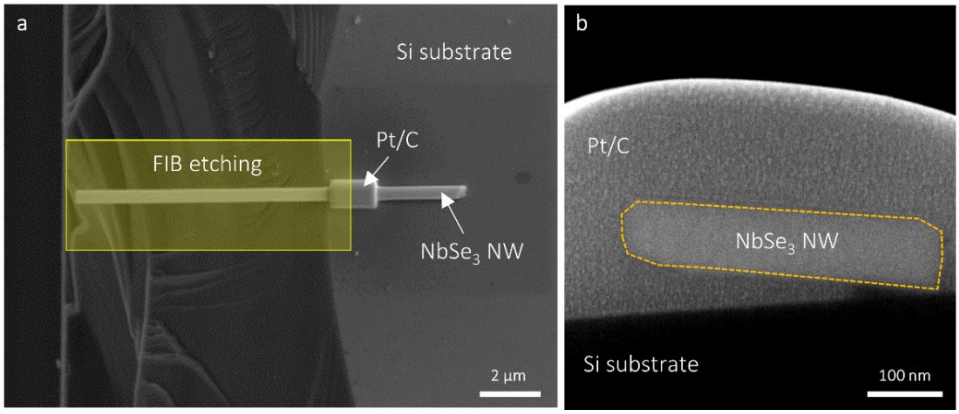

Figure 5.3 Cross section examination for individual $NbSe_3$ nanowires. (a) An SEM image shows the segment of a $NbSe_3$ nanowire (post transport property measurements) transferred and aligned perpendicularly to the edge of a piece of pre-cut Si wafer. Part of the wire is covered with EBID Pt/C composite, and a focused ion beam cutting is performed to remove the part shown in the yellow box. (b) An HRSEM micrograph collected after mounting the Si piece vertically on an SEM stub allowing for direct view of the cross-section of the $NbSe_3$ nanowire.

5.2 Contact Thermal Resistance and Length Dependent Thermal Transport

The contact thermal resistance between the nanowire and two membranes needs to be carefully considered while evaluating the nanowire thermal conductivity. In this work, EBID of Pt/C at the nanowire-electrode contacts was used to enhance the contact thermal conductance by enlarging the contact area. To confirm that we have reduced the contact thermal resistance to a negligible level, as shown in **Figure 5.4a-b**, we performed thermal measurements on the same sample with single EBID deposition and double EBID deposition schemes. **Figure 5.4c** plots the sample thermal conductance for the two measurements, which essentially overlaps with each other,

confirming that the measured nanowire thermal conductivity is not affected by the contact thermal resistance. It is worth mentioning that from the HRSEM image shown in **Figure 5.3b**, EBID will deposit Pt/C encapsulating the nanowire even when the sample is not placed in a flat contact with the substrate, which greatly increases the contact area and minimizes the contact thermal resistance.

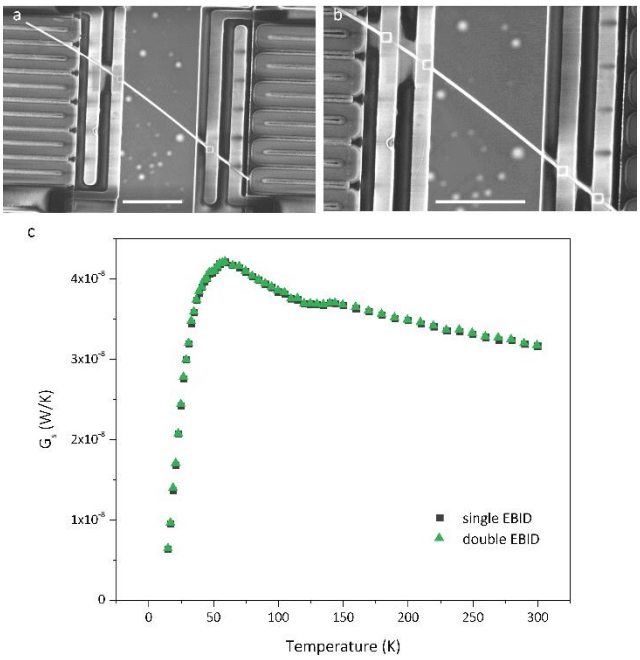

Figure 5.4 Contact thermal resistance characterization. SEM images show a $NbSe_3$ nanowire sample with (a) a single EBID treatment, and (b) double EBID treatments. Scale bars are both 5 μm. (c) The measured thermal conductance of the nanowire sample after the first and second EBID treatment overlaps with each other, indicating that the contact thermal resistance is reduced to a negligible level.

Quasi-1D vdW crystal nanowires could possess significant anisotropic properties, so it is important to evaluate the length dependent thermal transport in $NbSe_3$ and make sure that comparison between different diameter wires is not skewed by the suspended nanowire length. To do so, we performed thermal conductivity measurements on the same nanowire sample (D_h = 75 nm) with different suspended length between the heating and sensing membranes of the measurement device, as shown in the SEM images in **Figure 5.5(a-c)**. **Figure 5.5d** plots the

measured thermal conductivity for the wire with different suspended lengths as 3.3, 6.1 and 9.8 μm. It can be seen in **Figure 5.5e** that the room temperature thermal conductivity increases from 5.48 to 6.27 W/m-K as the suspended wire length increases from 3.3 to 6.1 μm. However, as it further increases to 9.8 μm, κ only increases by 2.8%.

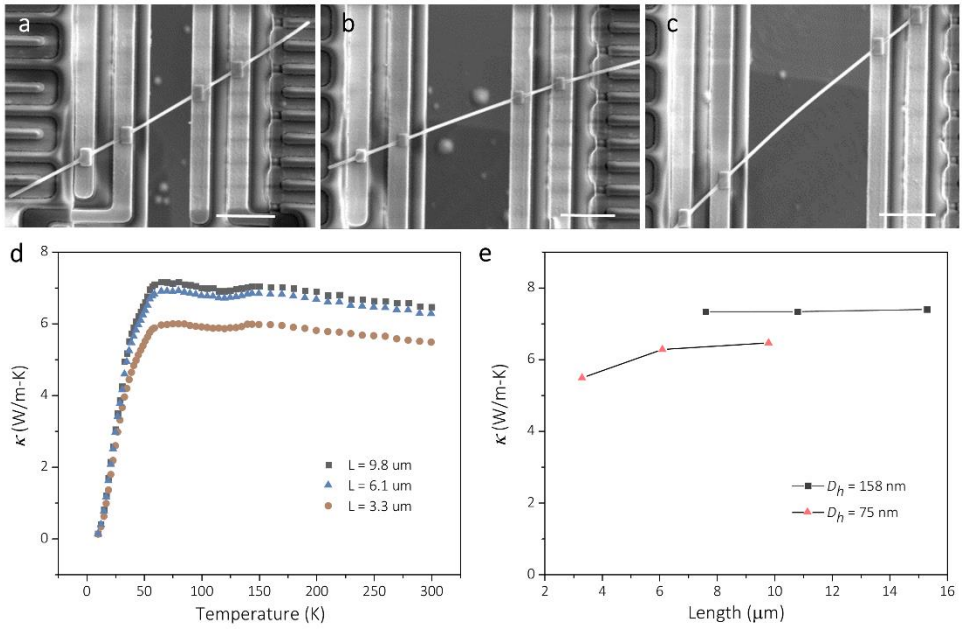

Figure 5.5 (a-c) Three SEM micrographs show the same nanowire with different suspended wire length between the two membranes, where the scale bars are all 3 μm. (d) Measured thermal conductivity for the same nanowire with different suspended lengths as 3.3, 6.1, and 9.8 μm, respectively. (e) Measured room temperature thermal conductivity plotted as a function of suspended length for the 158 and 75 nm diameter $NbSe_3$ nanowires.

To further confirm this, we measured thermal conductivity for another $NbSe_3$ nanowire with a hydraulic diameter of 158 nm, which indicates an essentially constant room temperature κ as L increases from 7.6 to 15.3 μm. This is different from that of TPdS nanowires, where the measured κ exhibits a persistent escalating trend till a length of 13 μm at 300 K (Zhang et al. 2018). We believe that the difference could be attributed to the stronger inter-chain bonding energy for $NbSe_3$, which leads to weaker phonon focusing effects along the molecular chain direction and substantial phonon boundary scattering. Also, as the measured κ approximately saturates at a suspended wire

length of 6.1 μm, we make sure that the suspended lengths of all tested samples are longer than 6 μm, which helps to eliminate any size effects and ensure a meaningful comparison between wires of different hydraulic diameters.

5.3 Distinct Signatures of e-ph Scattering in Lattice Thermal Conductivity

Figure 5.6a shows the measured electrical resistance (R) of a $NbSe_3$ nanowire with D_h = 135 nm. During the electrical resistance measurement, to exclude the effects from CDW sliding, we set the electric field to be much smaller than the measured depinning threshold electric field of the $NbSe_3$ nanowire with the same cross-sectional area (Grüner 1988, Slot et al. 2004). At temperatures above 145 K, R decreases as the temperature reduces, indicating a metallic behavior. However, two evident anomalies are observed at 145 K and 59 K, where R increases abruptly and reaches maxima at 130 K and 43 K, respectively. The amplitudes of the two peaks are 11% (T_{CDW1}) and 30% (T_{CDW2}) of the room temperature resistance, in good agreement with those reported for bulk $NbSe_3$ (Hodeau et al. 1978).

Figure 5.6b displays the Seebeck coefficient, which is similar to that of bulk $NbSe_3$ (Chaikin et al. 1981). Importantly, through applying the parabolic energy band assumption, the Lorenz number, L, can be derived *via* solutions to the Boltzmann transport equation based on the measured Seebeck coefficient (Kim et al. 2015a), which allows for calculation of the electron contribution to thermal conductivity using the Wiedemann-Franz (WF) law. Following the single parabolic band model, the Lorenz number, L, could be obtained using the following equation (Kaibe et al. 1989; Kim et al. 2015b,a):

$$L = \left(\frac{k_B}{e}\right)^2 \left(\frac{(r+7/2)F_{r+5/2}(\eta)}{(r+3/2)F_{r+1/2}(\eta)} - \left[\frac{(r+5/2)F_{r+3/2}(\eta)}{(r+3/2)F_{r+1/2}(\eta)}\right]^2 \right), \qquad (5.1)$$

where k_B is the Boltzmann constant, e is the elementary charge, r is the scattering parameter, $F_n(\eta)$ is the n-th order Fermi-Dirac integral, $F_n(\eta) = \int_0^\infty \frac{x^n}{1+e^{x-\eta}} dx$, and η is the reduced Fermi energy, respectively. The reduced Fermi energy η can be calculated from the following formula using the measured Seebeck coefficient (S):

$$S = \pm \frac{k_B}{e} \left(\frac{(r+5/2)F_{r+3/2}(\eta)}{(r+3/2)F_{r+1/2}(\eta)} - \eta \right). \tag{5.2}$$

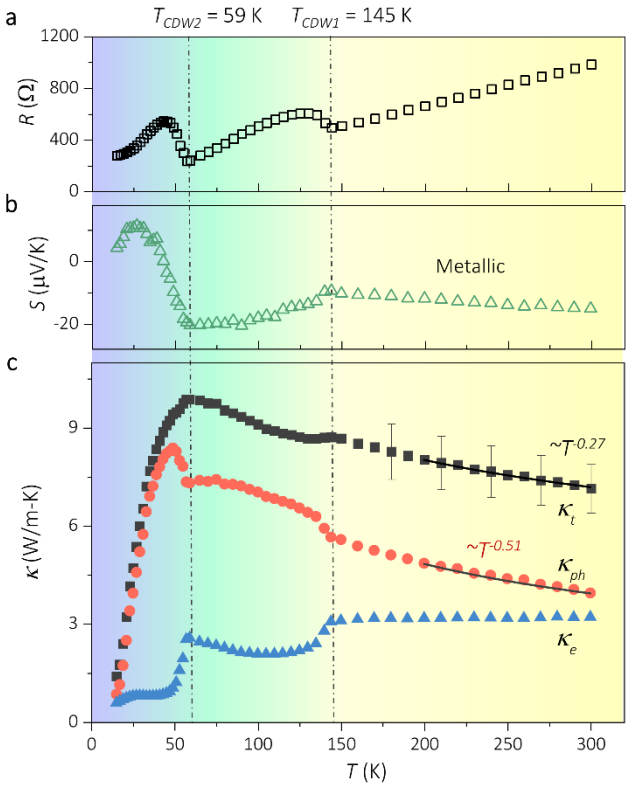

Figure 5.6 Distinct signatures of e-ph scattering in lattice thermal conductivity due to charge density waves. Measured electrical resistance (a), Seebeck coefficient (b), and thermal conductivity (c) of a 135 nm-diameter $NbSe_3$ nanowire in the temperature range of 15-300 K. The suspended length is 8.8 μm. The charge density wave (CDW) phase transition points at 145 K and 59 K have been identified from the measured data. The error bars for selected data points of κ_t are shown in (c). The magnitude of the error bars are smaller than the symbol size for the electrical resistance and Seebeck coefficient, and are not included in (a-b).

By assuming that the carrier relaxation time is limited mostly by phonon scattering (Kaibe et al. 1989, Kim et al. 2015a), we are able to numerically solve L by combining Eqn. (5.1-5.2), and

the obtained Lorenz number for the two $NbSe_3$ nanowires with different transverse dimensions is shown in **Figure 5.7**, where the degenerate limit is also plotted for comparison. The maximum deviation of the extracted L from the degenerate limit, $L_0 = 2.44\times10^{-8}$ WΩK^{-2}, occurs at 59 K with a value of 2.4×10^{-8} WΩK^{-2}, only ~1.6% lower than L_0. Therefore, it is reasonable to adopt L_0 in the WF law ($\kappa_e/\sigma T = L$, σ: electrical conductivity) to calculate the electronic thermal conductivity.

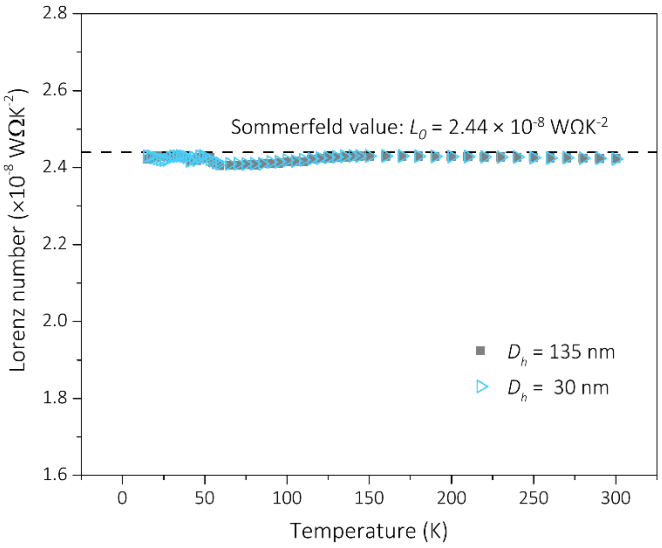

Figure 5.7 Calculated temperature dependent Lorenz number for the two $NbSe_3$ nanowires based on the parabolic band model and the measured Seebeck coefficient, where the Sommerfeld value of Lorenz number (L_0 = 2.44 × 10^{-8} WΩK^{-2}) is also plotted as a dashed line for comparison.

Figure 5.6c plots the measured total thermal conductivity (κ_t) as well as the derived electron and phonon contributions (κ_e and κ_{ph}). An important feature in κ_t is that it exhibits two local maxima at 145 K and 59 K, which correlates perfectly with the onset temperature of the two CDWs. More interesting observations come from κ_e and κ_{ph}. At the two T_{CDW}, κ_e displays abrupt drops, in agreement with the observed reduction in κ_t. It has been shown that the first CDW phase transition removes roughly half of the total charge carriers (n = 3.8 × 10^{21} cm^{-3} at 300 K), and the second leaves only a small part of the Fermi surface ungapped with n = 6 × 10^{18} cm^{-3} (Adelman et al.

1995). As such, the variation in κ_e is a direct result of conduction electron condensation due to CDWs.

More attractively, κ_{ph} presents an unusual temperature dependence with two distinct signatures corresponding to the two CDWs. As shown in **Figure 5.6c**, κ_{ph} displays a trend of $T^{-0.51}$ in the high temperature range. However, with the onset of the first CDW, the normal concave-up curve converts into a concave-down trend; and as the temperature drops to 59 K, a sharp peak appears. The coincidence of the anomalies in κ_e and κ_{ph} at both CDW transitions indicates that the abnormal peaks in κ_{ph} near T_{CDW1} and T_{CDW2} are indeed due to changes in the concentration of free electrons. Importantly, κ_e and κ_{ph} demonstrate exact opposite temperature dependence in the two CDW regimes, which strongly suggests that the abnormal trend in κ_{ph} is due to e-ph scattering. It is important to note that while the error bar from the measurement uncertainty is comparable to the measured total thermal conductivity anomaly at T_{CDW}, it will not affect our conclusion that the distinct signatures in lattice thermal conductivity are due to e-ph scattering. This is because the ~11% uncertainty primarily arises from errors in the nanowire dimensions as a systematic error for all κ_t, κ_e and κ_{ph}. The random errors that could cast doubt on the anomalous peaks is really small with a value of ~2%, much less than the magnitude of the anomalous peaks.

For a normal metallic nanowire, κ_e can be estimated by $\kappa_e = \frac{1}{3} C_e v_F l_e$, where C_e, υ_F, and l_e denote electron specific heat, group velocity (Fermi velocity), and mean free path (mfp), respectively. In the low temperature regime, boundary scattering leads to a constant l_e, and κ_e follows the temperature dependence of C_e as $\kappa_e \propto T$. At high temperatures, e-ph interactions dominate electron scattering with $l_e \propto 1/T$ as temperature rises above the Debye temperature (Θ_D), which yields a nearly constant κ_e (Kim et al. 2016). A smooth transition connects these two limits. The Debye temperature of a material can be calculated based on the measured low temperature

specific heat. The measured specific heat of $NbSe_3$ single crystals in the temperature range between 0.07 and 7.5 K is shown to roughly obey a $\gamma T + \beta T^3$ law, which represents the electronic and phonon contributions, respectively (Biljaković et al. 1991). Thus, the Debye temperature can be calculated from the formula as (Wang et al. 2006)

$$\theta_D{}^3 = \frac{12}{5}\pi^4 r R \beta^{-1}, \tag{5.3}$$

where R is the gas constant, r the total number of atoms in the formula unit (r = 4 for $NbSe_3$). From the fitted low temperature specific heat data, β is obtained as 30 erg $g^{-1}K^{-4}$ (Biljaković et al. 1991). We thus estimate the Debye temperature of $NbSe_3$ as ~200 K, and the obtained κ_e is indeed approximately constant for T > 145 K, which also explains the flatter temperature dependence of κ_t ($T^{-0.27}$) compared to κ_{ph} in high temperature regime. However, this $NbSe_3$ nanowire demonstrates a non-monotonic κ_e in the regime of the first CDW and a much larger slope in the regime of the second CDW, which can only be explained by the electron condensation during the CDW phase transitions.

An important trait of $NbSe_3$ is that its κ_e and κ_{ph} are comparable and as a result, distinct signatures in κ_{ph} appears due to e-ph coupling. Different from $NbSe_3$, for CDW material 1T-TaS_2, even though the measured κ_t displays a sharp drop at the onset of CDW, the reduction is fully attributed to κ_e with marginal change in κ_{ph} (Núñez-Regueiro et al. 1985). Moreover, for some other CDW materials, such as $K_{0.3}MoO_3$ and $(TaSe_4)_2I$ (Kwok & Brown 1989), κ_{ph} does display abnormal peaks but they are attributed to phasons but not e-ph scattering. In this case, the CDW is driven by the conventional Peierls transition involving Fermi-surface nesting and a strong softening in the low-energy phonon spectrum (Kohn anomaly) (Grüner 1988, Peierls 1955, Zhu et al. 2015). However, recent inelastic x-ray scattering measurements on $NbSe_3$ show no sign of

softening in phonon dispersion, and the CDWs in $NbSe_3$ have been attributed to charge redistribution driven by strong e-ph coupling, evidenced by a strong phonon line broadening at the location of CDW wave vector (Requardt et al. 2002). In this case, the phonon group velocity and lattice specific heat do not vary significantly across the CDW phase transition (Brill & Ong 1977, Hodeau et al. 1978, Tomić et al. 1981). For example, the measured Young's modulus E shows a very small anomaly at 145 K, and $\Delta E/E_0$, where ΔE is the difference of the measured E and the extrapolated E_0 according to the pre-transition behavior, is measured to be ~0.09% (Brill & Ong 1977). Moreover, no anomaly or slope change ($\Delta E/E_0 < 0.01\%$) is detected at 59 K (Brill & Ong 1977). Similar results have been observed in the specific heat measurement, where the measured anomaly, defined as $\Delta C/C_0$, is merely 3% and 1% at 145 K and 59 K, respectively (Tomić et al. 1981). Therefore, the unique temperature dependence of κ_{ph} observed in our $NbSe_3$ nanowires must come from the change in phonon mfp, due to changes in e-ph scattering, but not lattice specific heat variations.

5.4 Size Dependent Thermal/Electrical Transport in $NbSe_3$ Nanowires

For $NbSe_3$ nanowires with D_h less than the electron mfp, boundary scattering poses additional resistance to electron transport (McCarten et al. 1989). This is manifested in **Figure 5.8a**, where the room temperature electrical resistivity escalates as D_h reduces. Moreover, as the CDW phase transition temperatures and the presence of abnormal peaks in $R(T)$ do not change for D_h down to 30 nm, the long-range order of CDWs are preserved in the measurement size regime (Grüner 1988, Xi et al. 2015). As shown in **Figure 5.8b**, the higher electrical resistivity corresponds to lower κ_e. The amplitude of κ_e variations during CDW phase transitions also become significantly smaller; and as D_h reduces to 36 nm, the non-monotonic trend disappears. In addition, even though the carrier concentration remains largely unchanged as manifested by the nearly overlapped Seebeck

coefficients for different size nanowires, the enhanced phonon boundary scattering in smaller wires becomes more dominant and the distinct signatures in κ_{ph} induced by CDWs become less significant, as shown in **Figure 5.8c**. The systematic and correlated changes in σ, κ_e, and κ_{ph} *versus* D_h allow for examination of the effects of different factors though modeling.

Figure 5.8d plots κ_t for different diameter wires and despite the anisotropic quasi-1D structure of $NbSe_3$, κ_t still demonstrates a clear size dependence, with the temperature dependence varies from $T^{-0.03}$ to $T^{-0.27}$ for $T > 200$ K as D_h increases. The room temperature thermal conductivity *versus* D_h is plotted in **Figure 5.8e**, which suggests that κ_{ph} saturates at $D_h = 103$ nm while κ_e keeps increasing. This observation is consistent with the common understanding that electrons have a larger mfp than phonons in metals (Jain & McGaughey 2016, Wang et al. 2016). The persistent size dependence of κ_{ph} is somewhat unexpected given the quasi-1D nature of $NbSe_3$. However, as the calculated bonding energy shows (**Figure 5.8f**), the bonding strength along the *c*-direction (1.679 J/m^2) is comparable to that along the *b*-direction (2.962 J/m^2) of the wire axis. This rather strong inter-chain bonding leads to relatively weak phonon focusing and substantial phonon boundary scattering, which is also supported by the fact that the thermal conductivity only increases slightly with the sample length and saturates at a relatively short length of < 6 μm (**Figure 5.5**). Note that to exclude the effects from the ballistic transport of phonons in the measured thermal conductivity, we make sure that the suspended lengths of all tested samples are larger than 6 μm to ensure a meaningful comparison between wires of different hydraulic diameters.

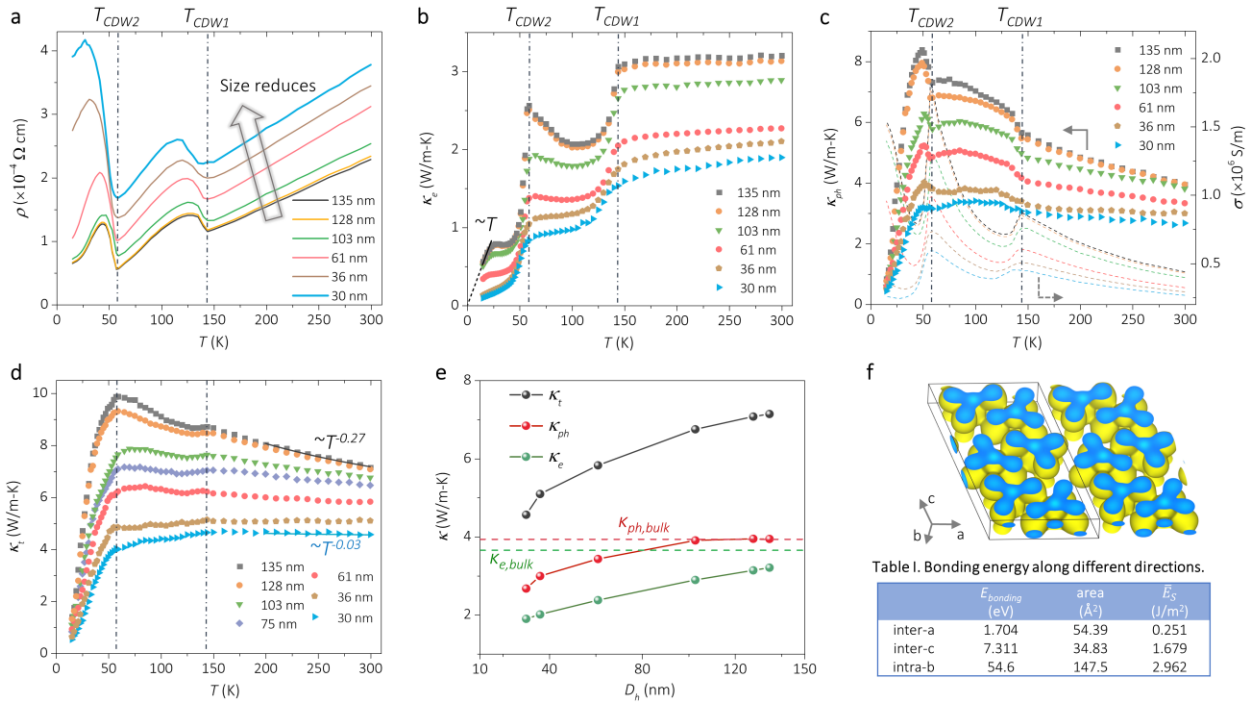

Table I. Bonding energy along different directions.

	$E_{bonding}$ (eV)	area (Å²)	E_S (J/m²)
inter-a	1.704	54.39	0.251
inter-c	7.311	34.83	1.679
intra-b	54.6	147.5	2.962

Figure 5.8 Size dependent thermal/electrical transport in $NbSe_3$ nanowires. (a-b) Measured electrical resistivity and derived electronic thermal conductivity of different size $NbSe_3$ nanowires in the temperature regime of 15-300 K. (c) Extracted lattice thermal conductivity (left axis), and the measured electrical conductivity of different size nanowires (right axis). (d) Measured total thermal conductivity. (e) Room temperature total thermal conductivity, electronic and lattice thermal conductivity plotted as a function of hydraulic diameter. (f) Simulated isosurface of electron density (0.27 e/Å^3), and the table shows the bonding energy along different crystalline directions. Here $E_{bonding}$ is the calculated total bonding energy for each crystal plane, and E_s is the average bonding energy per unit area.

5.5 Theoretical Modeling to Extract the Contribution of e-ph Scattering

To further understand the effects of e-ph interactions, we combine first-principles calculations with phenomenological models. The Vienna *ab initio* simulation package (VASP) is prepared for the DFT calculation (Kresse & Furthmüller 1996). An energy cut-off of 280 eV is chosen for the plane wave basis sets in the projector augmented wave (PAW) method. The exchange correlation interaction is treated with the general gradient approximation (GGA) in the Perdew-Burke-Ernzerhof (PBE) parametrization (Kresse & Joubert 1999). A 2×3×2 supercell is employed for the second-order and third-order calculations. The second order IFCs (inter-atomic force constants) of

each atomic structure are obtained using density functional perturbation theory (DFPT) (Gonze & Lee 1997) and the phonopy code (Togo et al. 2008). Only interactions up to the second nearest neighbors are considered in the third-order calculations. Based on the DFT result, the phonon dispersion (**Figure 5.9**) can be obtained by solving the phonon BTE as implemented in the ShengBTE code (Gonze & Lee 1997, Kresse & Joubert 1999, Li et al. 2014b, Togo et al. 2008).

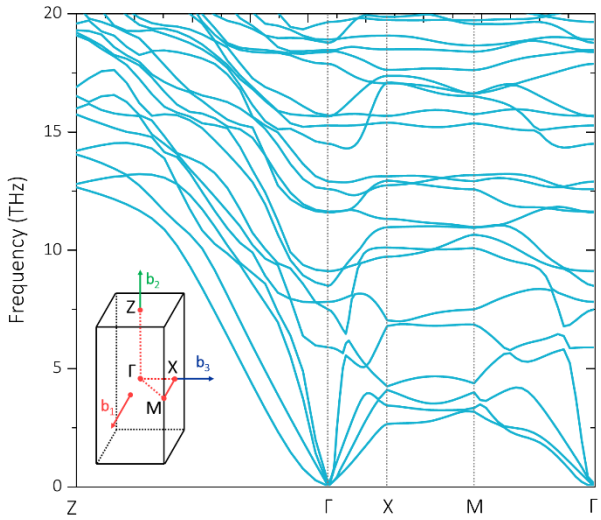

Figure 5.9 Calculated phonon dispersion relation of bulk $NbSe_3$ along high symmetry points, where these high symmetry points in the Brillouin zone is shown in the inset.

We then solve for κ_{ph} along the *b*-direction using (Li et al. 2014b)

$$\kappa_{ph} = \frac{1}{k_B T^2 \Omega N} \sum_j f_0 \left(f_0 + 1 \right) \left(\hbar \omega \upsilon_j \right)^2 \tau_j , \tag{5.4}$$

where k_B, T, Ω, N, $\hbar$, ω, and υ_j are the Boltzmann constant, temperature, volume of unit cell, number of wave vector points, reduced Plank constant, phonon frequency and mode j dependent phonon group velocity, respectively. f_0 is the equilibrium Bose-Einstein distribution, and the mode dependent phonon relaxation time τ_j is considered using Matthiessen's rule as

$$\tau_j^{-1} = \tau_{j,defects}^{-1} + \tau_{j,Umklapp}^{-1} + \tau_{j,boundary}^{-1} + \tau_{j,e-ph}^{-1} . \tag{5.5}$$

The phonon relaxation time is dominated by defects, Umklapp, boundary and e-ph scattering mechanisms, which are determined as $\tau_{j,defects}^{-1} = A\omega_j(q)^4$, $\tau_{j,Umklapp}^{-1} = BT\omega_j(q)^2\exp(-C/T)$, $\tau_{j,boundary}^{-1} = v_j(q)/D_h$, and $\tau_{j,e-ph}^{-1} = (m_e E_D)^2 k_B T \chi_\omega/(2\pi\rho\hbar^4 v_j^2(q))$ (Asheghi et al. 2002), respectively. Here, D_h is the hydraulic diameter of the $NbSe_3$ nanowires; ρ is the material's density; m_e is the electron effective masses (Sengupta et al. 2013); and $\chi_\omega = \hbar\omega/k_B T$. The deformation potential depends on the carrier concentration according to $E_D = Fn^{2/3}$, where F is a fitting parameter (Asheghi et al. 2002, Ziman 2011). The temperature dependent carrier concentration n is calculated according to $n = \sigma/e\mu$, where σ is the measured electrical conductivity of the nanowire, e is the elementary charge, and μ is the mobility obtained from the previously reported experimental data (Ong 1978). We note that for really small wires (<10 nm diameter), it has been predicted that the e-ph scattering rate could be higher than the bulk value due to confinement (Arbouet et al. 2003, Ramayya et al. 2008); however, our wires are still in the classical size effect regime and the measured resistivity resemble the shape of the bulk resistivity, indicating that the e-ph scattering rate does not deviate significantly from the bulk value.

The modeling results for three different wires (D_h = 135, 61, 30 nm) are shown in **Figure 5.10**, and the only parameter varying from wire to wire is the boundary scattering term. For the sample with D_h = 135 nm, the modeled κ_{ph} without considering e-ph scattering displays a trend of $T^{-0.8}$, exhibiting a stronger temperature dependence compared to the measured κ_{ph} and approaches the T^{-1} behavior for bulk single crystalline materials. Moreover, extensive modeling efforts show that without considering e-ph scattering, κ_{ph} always follows the typical shape for crystalline materials with a smooth profile in the whole temperature range, no matter how we tune different scattering mechanisms. Only with the e-ph scattering term introduced, the modeled κ_{ph} can fit the

experimental data well, which strongly indicates that it is indeed the e-ph scattering that leads to the distinct signatures in κ_{ph}.

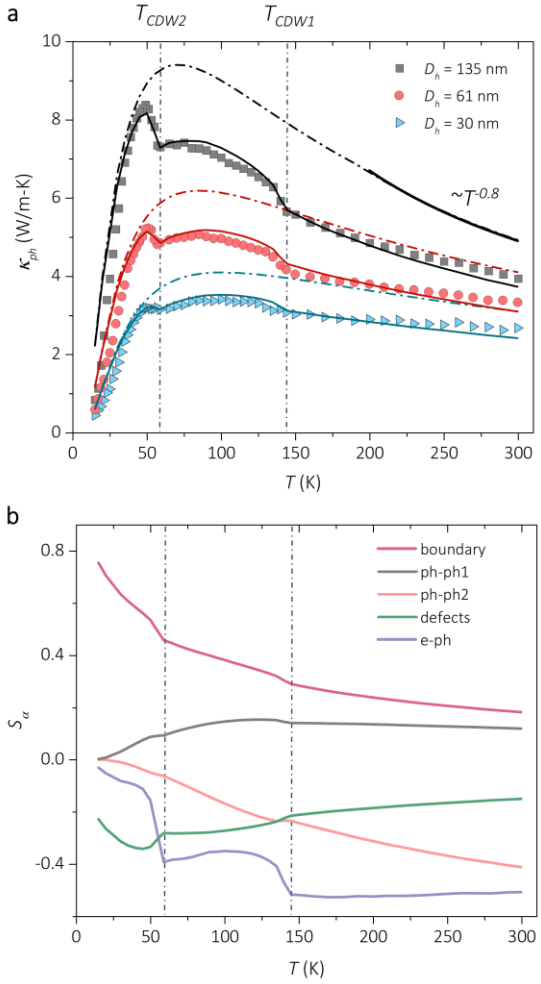

Figure 5.10 (a) Comparison between fitted and measured lattice thermal conductivity for three NbSe3 nanowires with Dh of 135, 61 and 30 nm, where the dashed and solid lines show the modeling result without and with taking the e-ph scattering into consideration, respectively. (b) Sensitivity analysis for different scattering mechanisms, where anomalous jumps corresponding to the two CDW phase transitions could be observed in Se-ph. Here, ph-ph1 and ph-ph2 are the two fitting parameters for the Umklapp scattering mechanism.

To demonstrate the uniqueness of different fitting parameters, we solve for the sensitivity coefficients (S_α) defined as the fractional variation of κ_{ph} with respect to each fitting parameter (α) in different scattering terms, given by $S_\alpha = \partial[\ln(\kappa_{ph})]/\partial[\ln(\alpha)]$ (Koh et al. 2009). The

sensitivity coefficient gives the fractional change in the calculated thermal conductivity divided by the fractional perturbation in the parameter's value from the best fit result at any given temperature. Importantly, the shape of the sensitivity curves determines how uniquely each fitting parameter can be extracted. If two fitting parameters have either similar sensitivity coefficients, or their sensitivity curves have the same trend over a range of temperatures, it means they cannot be uniquely distinguished from each other.

Figure 5.10b depicts the calculated S_α for the boundary, Umklapp, defects, and e-ph scattering parameters as a function of temperature. Consistent with conventional understanding, the magnitude of S_α manifests the dominant role of boundary, defects, and Umklapp scatterings in the low, peak thermal conductivity, and high temperature regimes. Importantly, S_α for the e-ph scattering term shows two anomalous jumps at the onset of the CDW phase transition temperatures, indicating its dominant role for the abnormal peaks observed in κ_{ph}. We note that the extracted e-ph scattering rate is comparable to or a little higher than those for heavily doped Si (Liao et al. 2015) and normal metals (Jain & McGaughey 2016, Wang et al. 2016).

Moreover, **Figure 5.10b** indicates that above 150 K, the sensitivity coefficients for the e-ph scattering and defect scattering demonstrate similar temperature dependence, which means that in this regime, one could fit the measured lattice thermal conductivity by tuning either of the two fitting parameters. This is probably the reason why even though the effects of e-ph scattering are usually neglected in modeling the lattice thermal conductivity of heavily doped semiconductors, as pointed out by Liao et al. (Liao et al. 2015), a fairly good fitting can still be obtained through adjusting the fitting parameter for defect scattering. The distinct signatures in the lattice thermal conductivity of $NbSe_3$ nanowires disclosed here, however, clearly indicate the importance of e-ph

interactions in determining the lattice thermal conductivity and help to understand its contributions quantitatively.

5.6 Summary

In summary, systematic studies on transport properties of $NbSe_3$ nanowires disclose distinct signatures of e-ph scattering on lattice thermal conductivity due to CDW phase transitions, which provides answers to long-standing, fundamental questions of whether and how e-ph interactions affect phonon transport. Given the ubiquitous nature of e-ph coupling in heavily-doped semiconductors and metals, this discovery urges re-examination of thermal transport processes in microelectronic, photovoltaic and optoelectronic devices, which could improve device design and performance.

Chapter 6

Summary

The intent of this dissertation is to address some of the fundamental questions about phonon transport in nanowires beyond the classical size effect. Using the suspended microbridge platform with enhanced thermal and thermoelectric measurement sensitivity, and coupled with Young's modulus measurement using the three-point bending scheme, we are able to uncover several interesting thermal transport phenomena that yield better understanding of thermal transport at the nanoscale. This chapter serves to summarize some of the key findings.

The Wheatstone bridge sensing scheme was incorporated into our measurement setup, which improved the thermal conductance measurement sensitivity down to the order of 10 pW/K. The effectiveness of adding the inner radiation shield is demonstrated by monitoring the local temperature of the measurement device through an additional temperature sensor, and it was confirmed that the temperature deviation from the setting temperature is very small (< 2.8 K) in the whole temperature range (10-420 K).

To explore the conditions for novel size effects beyond the Casimir limit to occur, we fabricated and measured thermal conductivities of two groups of Si nanoribbons of ∼20 and ∼30 nm thickness and various widths. The results show that while the data for the ∼30 nm thick ribbons can be well-explained by the classical size effect, the measured thermal conductivities for the ∼20 nm thick ribbons deviate from the prediction remarkably. Importantly, the measurements of the Young's modulus of the thin nanoribbons yield significantly lower values than the corresponding bulk value, which could lead to a reduced phonon group velocity and subsequently lower thermal conductivity.

Traditionally, thermal transport in amorphous silicon dioxide (a-SiO_2) is treated as random walks of vibrations owing to its greatly disordered structure, which results in a phonon MFP approximately the same as the interatomic distance. However, this picture has been debated constantly and in view of the ubiquitous existence of thin a-SiO_2 layers in nanoelectronic devices, it is imperative to better understand this for precise thermal management of electronic devices. Different from the commonly used cross-plane measurement approaches, we studied the in-plane thermal conductivity of double silicon nanoribbons bonded by van der Waals interaction and with a layer of a-SiO_2 sandwiched in-between. Through comparing the thermal conductivity of the double ribbon samples with that of corresponding single ribbons, we show that thermal phonons can ballistically penetrate through a-SiO_2 of up to 5 nm thick even at room temperature.

Moreover, although tremendous progress in quantitative understanding of several major phonon scattering mechanisms (phonon-phonon, phonon-boundary, phonon-defects) has been achieved, the roles of another fundamental scattering mechanism, electron-phonon (e-ph) interaction, remain elusive. This is largely due to the lack of solid experimental evidence showing the effects of e-ph scattering. To cope with this challenge, we measured the thermal/electrical conductivity and Seebeck coefficient of the same $NbSe_3$ nanowires. $NbSe_3$ belongs to a class of quasi-1D vdW materials with the unique charge density wave (CDW) properties, and the variation of charge carrier concentration upon the onset of CDW modulates the e-ph scattering strength, which results in unique features in the extracted lattice thermal conductivity. The critical role of e-ph scattering is further confirmed by combining the first-principles calculations with phenomenological models, which shows that the distinct signatures in lattice thermal conductivity cannot be recaptured without considering e-ph scattering.

References

Adelman TL, Zaitsev-Zotov SV, Thorne RE. 1995. Field-effect modulation of charge-density-wave transport in NbSe3 and TaS3. *Phys. Rev. Lett.* 74(26):5264–67

Alaie S, Goettler DF, Su M, Leseman ZC, Reinke CM, El-Kady I. 2015. Thermal transport in phononic crystals and the observation of coherent phonon scattering at room temperature. *Nat. Commun.* 6:7228

Anufriev R, Maire J, Nomura M. 2016. Reduction of thermal conductivity by surface scattering of phonons in periodic silicon nanostructures. *Phys. Rev. B.* 93(4):045411

Anufriev R, Nomura M. 2015. Thermal conductance boost in phononic crystal nanostructures. *Phys. Rev. B.* 91(24):245417

Arbouet A, Voisin C, Christofilos D, Langot P, Fatti N Del, et al. 2003. Electron-Phonon Scattering in Metal Clusters. *Phys. Rev. Lett.* 90(17):177401

Asheghi M, Kurabayashi K, Kasnavi R, Goodson KE. 2002. Thermal conduction in doped single-crystal silicon films. *J. Appl. Phys.* 91(8):5079–88

Bellan LM, Kameoka J, Craighead HG. 2005. Measurement of the Young's moduli of individual polyethylene oxide and glass nanofibres. *Nanotechnology*. 16(8):1095–99

Biljaković K, Lasjaunias JC, Monceau P. 1991. Low-temperature specific heat of NbSe3: A reassessment. *Phys. Rev. B.* 43(4):3117–22

Blanc C, Rajabpour A, Volz S, Fournier T, Bourgeois O. 2013. Phonon heat conduction in corrugated silicon nanowires below the Casimir limit. *Appl. Phys. Lett.* 103(2013):3–7

Boukai AI, Bunimovich Y, Tahir-Kheli J, Yu J-K, Goddard III WA, Heath JR. 2008. Silicon nanowires as efficient thermoelectric materials. *Nature*. 451(7175):168–71

Braun JL, Baker CH, Giri A, Elahi M, Artyushkova K, et al. 2016. Size effects on the thermal conductivity of amorphous silicon thin films. *Phys. Rev. B.* 93(14):140201

Brill JW, Ong NP. 1977. Young's modulus of NbSe3. *Solid State Commun.* 25(12):1075—1078

Brockhouse BN. 1959. Lattice Vibrations in Silicon and Germanium. *Phys. Rev. Lett.* 2(6):256–58

Bui CT, Xie R, Zheng M, Zhang Q, Sow CH, et al. 2012. Diameter-dependent thermal transport in individual ZnO nanowires and its correlation with surface coating and defects. *Small*. 8(5):738–45

Butler WH, Williams RK. 1978. Electron-phonon interaction and lattice thermal conductivity. *Phys. Rev. B.* 18(12):6483–94

Cahill DG, Watson SK, Pohl RO. 1992. Lower limit to the thermal conductivity of disordered crystals. *Phys. Rev. B.* 46(10):6131–40

Calahorra Y, Shtempluck O, Kotchetkov V, Yaish YE. 2015. Young's modulus, residual stress, and crystal orientation of doubly clamped silicon nanowire beams. *Nano Lett.* 15(5):2945–50

Callaway J. 1959. Model for lattice Thermal Conductivity at Low Temperatures. *Phys. Rev.* 113(4):1046–51

Cha G, Gafiteanu R, Gosele U. 1994. Low temperature wafer direct bonding. *J. Microelectromechanical Syst.* 3(1):29–35

Chaikin PM, Fuller WW, Lacoe R, Kwak JF, Greene RL, et al. 1981. Thermopower of doped and damaged NbSe3. *Solid State Commun.* 39(4):553–57

Chambers RG. 1950. The Conductivity of Thin Wires in a Magnetic Field. *Proc. R. Soc. A Math. Phys. Eng. Sci.* 202(1070):378–94

Chang CW, Okawa D, Garcia H, Majumdar A, Zettl A. 2007. Nanotube phonon waveguide. *Phys.*

Rev. Lett. 99(4):045901
Chang THP. 1975. Proximity effect in electron-beam lithography. *J. Vac. Sci. Technol.* 12(6):1271–75
Chen CQ, Shi Y, Zhang YS, Zhu J, Yan YJ. 2006. Size dependence of Young's modulus in ZnO nanowires. *Phys. Rev. Lett.* 96(7):075505
Chen J, Zhang G, Li B. 2012. Thermal contact resistance across nanoscale silicon dioxide and silicon interface. *J. Appl. Phys.* 112(6):
Chen R, Hochbaum AI, Murphy P, Moore J, Yang P, Majumdar A. 2008. Thermal Conductance of Thin Silicon Nanowires. *Phys. Rev. Lett.* 101(10):105501
Cheze C, Geelhaar L, Trampert A, Brandt O, Riechert H. 2010. Collector Phase Transitions during Vapor-Solid-Solid Nucleation of GaN Nanowires. *Nano Lett.* 10(9):3426–31
Chiam SY, Kong L, Zhao Y, Wu J, Thong JTL, et al. 2017. Ultralow Thermal Conductivity of Single-Crystalline Porous Silicon Nanowires. *Adv. Funct. Mater.* 27(40):1702824
Crnjar A, Melis C, Colombo L. 2018. Assessing the anomalous superdiffusive heat transport in a single one-dimensional PEDOT chain. *Phys. Rev. Mater.* 2(1):015603
Cuenot S, Frétigny C, Demoustier-Champagne S, Nysten B. 2004. Surface tension effect on the mechanical properties of nanomaterials measured by atomic force microscopy. *Phys. Rev. B.* 69(16):165410
Cuffe J, Chavez E, Shchepetov A, Chapuis PO, El Boudouti EH, et al. 2012. Phonons in slow motion: Dispersion relations in ultrathin Si membranes. *Nano Lett.* 12(7):3569–73
Dames C, Chen G. 2004. Theoretical phonon thermal conductivity of Si/Ge superlattice nanowires. *J. Appl. Phys.* 95(2):682–93
Deal BE, Grove AS. 1965. General relationship for the thermal oxidation of silicon. *J. Appl. Phys.* 36(12):3770–78
Deng B, Chernatynskiy A, Khafizov M, Hurley DH, Phillpot SR. 2014. Kapitza resistance of Si/SiO2 interface. *J. Appl. Phys.* 115(8):084910
Donadio D, Galli G. 2010. Temperature Dependence of the Thermal Conductivity of Thin Silicon Nanowires. *Nano Lett.* 10(3):847–51
Duda JC, Hopkins PE, Shen Y, Gupta MC. 2013. Thermal transport in organic semiconducting polymers. *Appl. Phys. Lett.* 102(25):251912
Einstein A. 1911. Elementare Betrachtungen über die thermische Molekularbewegung in festen Körpern. *Ann. Phys.* 340(9):679–94
Esfarjani K, Chen G, Stokes HT. 2011. Heat transport in silicon from first-principles calculations. *Phys. Rev. B - Condens. Matter Mater. Phys.* 84(8):085204
Ferain I, Colinge CA, Colinge J-P. 2011. Multigate transistors as the future of classical metal–oxide–semiconductor field-effect transistors. *Nature*. 479(7373):310–16
Gonze X, Lee C. 1997. Dynamical matrices, Born effective charges, dielectric permittivity tensors, and interatomic force constants from density-functional perturbation theory. *Phys. Rev. B.* 55(16):10355–68
Goodson KE, Flik MI, Su LT, Antoniadis DA. 1994. Prediction and Measurement of the Thermal Conductivity of Amorphous Dielectric Layers. *J. Heat Transfer*. 116(2):317
Gösele U, Bluhm Y, Kästner G, Kopperschmidt P, Kräuter G, et al. 1999. Fundamental issues in wafer bonding. *J. Vac. Sci. Technol. A Vacuum, Surfaces, Film.* 17(4):1145
Graebner JE, Golding B, Allen LC. 1986. Phonon localization in glasses. *Phys. Rev. B.* 34(8):5696–5701
Griffin AJ, Brotzen FR, Loos PJ. 1994. Effect of thickness on the transverse thermal conductivity

of thin dielectric films. *J. Appl. Phys.* 75(8):3761–64
Grüner G. 1988. The dynamics of charge-density waves. *Rev. Mod. Phys.* 60(4):1129–81
He Y, Galli G. 2012. Microscopic origin of the reduced thermal conductivity of silicon nanowires. *Phys. Rev. Lett.* 108(21):215901
Heitsch AT, Fanfair DD, Tuan H-Y, Korgel BA. 2008. Solution−Liquid−Solid (SLS) Growth of Silicon Nanowires. *J. Am. Chem. Soc.* 130(16):5436–37
Henry A, Chen G. 2008. High thermal conductivity of single polyethylene chains using molecular dynamics simulations. *Phys. Rev. Lett.* 101(23):235502
Herring C. 1954. Theory of the thermoelectric power of semiconductors. *Phys. Rev.* 96(5):1163–87
Hippalgaonkar K, Huang B, Chen R, Sawyer K, Ercius P, Majumdar A. 2010. Fabrication of microdevices with integrated nanowires for investigating low-dimensional phonon transport. *Nano Lett.* 10(11):4341–48
Ho CY, Powell RW, Liley PE. 1972. Thermal Conductivity of the Elements. *J. Phys. Chem. Ref. Data*. 1(2):279
Hobbs RG, Petkov N, Holmes JD. 2012. Semiconductor Nanowire Fabrication by Bottom-Up and Top-Down Paradigms. *Chem. Mater.* 24(11):1975–91
Hochbaum AI, Chen R, Delgado RD, Liang W, Garnett EC, et al. 2008. Enhanced thermoelectric performance of rough silicon nanowires. *Nature*. 451(7175):163–67
Hochbaum AI, Gargas D, Hwang YJ, Yang P. 2009. Single Crystalline Mesoporous Silicon Nanowires. *Nano Lett.* 9(10):3550–54
Hodeau JL, Marezio M, Roucau C, Ayroles R, Meerschaut A, et al. 1978. Charge-density waves in NbSe3 at 145K: crystal structures and electron diffraction studies. *J. Phys. C Solid State Phys.* 11:4117–30
Holland M. 1963. Analysis of Lattice Thermal Conductivity. *Phys. Rev.* 132(6):2461–71
Holland MG. 1964. Phonon Scattering in Semiconductors From Thermal Conductivity Studies. *Phys. Rev.* 134(2A):A471–80
Holmes JD, Johnston KP, Doty RC, Korgel BA. 2000. Control of thickness and orientation of solution-grown silicon nanowires. *Science (80-.).* 287(5457):1471–73
Hopkins PE, Rakich PT, Olsson RH, El-kady IF, Phinney LM. 2009. Origin of reduction in phonon thermal conductivity of microporous solids. *Appl. Phys. Lett.* 95(16):161902
Hu Y, Zeng L, Minnich AJ, Dresselhaus MS, Chen G. 2015. Spectral mapping of thermal conductivity through nanoscale ballistic transport. *Nat. Nanotechnol.* 10(8):701–6
Hurley DH, Khafizov M, Shinde SL. 2011. Measurement of the Kapitza resistance across a bicrystal interface. *J. Appl. Phys.* 109(8):083504
Iijima S. 1991. Helical microtubules of graphitic carbon. *Nature*. 354(6348):56–58
Jain A, McGaughey AJH. 2016. Thermal transport by phonons and electrons in aluminum, silver, and gold from first principles. *Phys. Rev. B*. 93(8):081206
Jain A, Yu YJ, McGaughey AJH. 2013. Phonon transport in periodic silicon nanoporous films with feature sizes greater than 100 nm. *Phys. Rev. B - Condens. Matter Mater. Phys.* 87(19):195301
Jeng M-S, Yang R, Song D, Chen G. 2008. Modeling the Thermal Conductivity and Phonon Transport in Nanoparticle Composites Using Monte Carlo Simulation. *J. Heat Transfer*. 130(4):042410
Jerez-Hanckes CF, Qiao D, Lau SS. 2003. A study of Si wafer bonding via methanol capillarity. *Mater. Chem. Phys.* 77(3):751–54

Jiang JW, Yang N, Wang BS, Rabczuk T. 2013. Modulation of thermal conductivity in kinked silicon nanowires: Phonon interchanging and pinching effects. *Nano Lett.* 13(4):1670–74
Jiang Z, Qing Q, Xie P, Gao R, Lieber CM. 2012. Kinked p-n junction nanowire probes for high spatial resolution sensing and intracellular recording. *Nano Lett.* 12(3):1711–16
Jin Y, Shao C, Kieffer J, Pipe KP, Shtein M. 2012. Origins of thermal boundary conductance of interfaces involving organic semiconductors. *J. Appl. Phys.* 112(9):093503
Josell D, Brongersma SH, Tőkei Z. 2009. Size-Dependent Resistivity in Nanoscale Interconnects. *Annu. Rev. Mater. Res.* 39(1):231–54
Josell D, Burkhard C, Li Y, Cheng YW, Keller RR, et al. 2004. Electrical properties of superfilled sub-micrometer silver metallizations. *J. Appl. Phys.* 96(1):759–68
Ju YS, Goodson KE. 1999. Phonon scattering in silicon films with thickness of order 100 nm. *Appl. Phys. Lett.* 74(20):3005
Kaibe H, Tanaka Y, Sakata M, Nishida I. 1989. Anisotropic galvanomagnetic and thermoelectric properties of n-type Bi2Te3 single crystal with the composition of a useful thermoelectric cooling material. *J. Phys. Chem. Solids*. 50(9):945–50
Kim HS, Gibbs ZM, Tang Y, Wang H, Snyder GJ. 2015a. Characterization of Lorenz number with Seebeck coefficient measurement. *APL Mater.* 3(4):041506
Kim S Il, Lee KH, Mun HA, Kim HS, Hwang SW, et al. 2015b. Thermoelectrics. Dense dislocation arrays embedded in grain boundaries for high-performance bulk thermoelectrics. *Science*. 348(6230):109–14
Kim P, Shi L, Majumdar a, McEuen PL. 2001. Thermal transport measurements of individual multiwalled nanotubes. *Phys. Rev. Lett.* 87(21):215502
Kim TY, Park C-H, Marzari N. 2016. The electronic thermal conductivity of graphene. *Nano Lett.* 16(4):2439–43
Kittel C. 1949. Interpretation of the Thermal Conductivity of Glasses. *Phys. Rev.* 75(6):972–74
Kodama T, Jain A, Goodson KE. 2009. Heat Conduction through a DNA?Gold Composite. *Nano Lett.* 9(5):2005–9
Koh M. 2001. Limit of gate oxide thickness scaling in MOSFETs due to apparent threshold voltage fluctuation induced by tunnel leakage current. *IEEE Trans. Electron Devices*. 48(2):259–64
Koh YK, Cahill DG. 2007. Frequency dependence of the thermal conductivity of semiconductor alloys. *Phys. Rev. B.* 76(7):075207
Koh YK, Singer SL, Kim W, Zide JMO, Lu H, et al. 2009. Comparison of the 3ω method and time-domain thermoreflectance for measurements of the cross-plane thermal conductivity of epitaxial semiconductors. *J. Appl. Phys.* 105(5):054303
Kresse G, Furthmüller J. 1996. Efficiency of ab-initio total energy calculations for metals and semiconductors using a plane-wave basis set. *Comput. Mater. Sci.* 6(1):15–50
Kresse G, Joubert D. 1999. From ultrasoft pseudopotentials to the projector augmented-wave method. *Phys. Rev. B.* 59(3):1758–75
Kwok RS, Brown SE. 1989. Thermal conductivity of the charge-density-wave systems K0.3MoO3 and (TaSe4)2I near the peierls transition. *Phys. Rev. Lett.* 63(8):895–98
Kwon S, Zheng J, Wingert MC, Cui S, Chen R. 2017. Unusually High and Anisotropic Thermal Conductivity in Amorphous Silicon Nanostructures. *ACS Nano*. 11(3):2470–76
Lanzara A, Bogdanov P V., Zhou XJ, Kellar SA, Feng DL, et al. 2001. Evidence for ubiquitous strong electron–phonon coupling in high-temperature superconductors. *Nature*. 412(6846):510–14
Larkin JM, McGaughey AJH. 2014. Thermal conductivity accumulation in amorphous silica and

amorphous silicon. *Phys. Rev. B - Condens. Matter Mater. Phys.* 89(14):144303
Lee J, Lee W, Lim J, Yu Y, Kong Q, et al. 2016a. Thermal Transport in Silicon Nanowires at High Temperature up to 700 K. . 16(7), 4133-4140.
Lee J, Lee W, Lim J, Yu Y, Kong Q, et al. 2016b. Thermal Transport in Silicon Nanowires at High Temperature up to 700 K. *Nano Lett.* 16(7):4133–40
Lee J, Lee W, Wehmeyer G, Dhuey S, Olynick DL, et al. 2017. Investigation of phonon coherence and backscattering using silicon nanomeshes. *Nat. Commun.* 8:14054
Lee S, Cahill D. 1997. Heat transport in thin dielectric films. *J. Appl. Phys.* 81(1997):2590–95
Lee V, Chen R, Chang C-W. 2013. Probing the limit of one-dimensional heat transfer under extreme bending strain. *Phys. Rev. B.* 87(3):035406
Lepri S, Livi R, Politi A. 2003. Thermal conduction in classical low-dimensional lattices. *Phys. Rep.* 377(1):1–80
Li B, Wang J. 2003. Anomalous Heat Conduction and Anomalous Diffusion in One-Dimensional Systems. *Phys. Rev. Lett.* 91(4):044301
Li D, Huxtable ST, Abramson AR, Majumdar A. 2005. Thermal Transport in Nanostructured Solid-State Cooling Devices. *J. Heat Transfer*. 127(1):108
Li D, Wu Y, Fan R, Yang P, Majumdar A. 2003a. Thermal conductivity of Si/SiGe superlattice nanowires. *Appl. Phys. Lett.* 83(15):3186–88
Li D, Wu Y, Kim P, Shi L, Yang P, Majumdar A. 2003b. Thermal conductivity of individual silicon nanowires. *Appl. Phys. Lett.* 83(14):2934
Li P, Hu L, McGaughey AJH, Shen S. 2014a. Crystalline polyethylene nanofibers with the theoretical limit of Young's modulus. *Adv. Mater.* 26(7):1065–70
Li W, Carrete J, A. Katcho N, Mingo N. 2014b. ShengBTE: A solver of the Boltzmann transport equation for phonons. *Comput. Phys. Commun.* 185(6):1747–58
Li X, Ono T, Wang Y, Esashi M. 2003c. Ultrathin single-crystalline-silicon cantilever resonators: Fabrication technology and significant specimen size effect on Young's modulus. *Appl. Phys. Lett.* 83(15):3081–83
Liang Z, Keblinski P. 2016. Sound attenuation in amorphous silica at frequencies near the boson peak. *Phys. Rev. B - Condens. Matter Mater. Phys.* 93(5):054205
Liang Z, Wilson TE, Keblinski P. 2017. Phonon interference in crystalline and amorphous confined nanoscopic films. *J. Appl. Phys.* 121(7):075303
Liao B, Maznev AA, Nelson KA, Chen G. 2016. Photo-excited charge carriers suppress sub-terahertz phonon mode in silicon at room temperature. *Nat. Commun.* 7:13174
Liao B, Qiu B, Zhou J, Huberman S, Esfarjani K, Chen G. 2015. Significant reduction of lattice thermal conductivity by the electron-phonon interaction in silicon with high carrier concentrations: A first-principles study. *Phys. Rev. Lett.* 114(11):115901
Lim J, Hippalgaonkar K, Andrews SC, Majumdar A. 2012. Quantifying Surface Roughness Effects on Phonon Transport in Silicon Nanowires. *Nano Lett.* 12(5):2475–2482
Lim J, Wang H-T, Tang J, Andrews SC, So H, et al. 2016. Simultaneous Thermoelectric Property Measurement and Incoherent Phonon Transport in Holey Silicon. *ACS Nano*. 10(1):124–32
Liu L, Chen X. 2010. Effect of surface roughness on thermal conductivity of silicon nanowires. *J. Appl. Phys.* 107(3):033501
Liu S, Xu XF, Xie RG, Zhang G, Li BW. 2012. Anomalous heat conduction and anomalous diffusion in low dimensional nanoscale systems. *Eur. Phys. J. B.* 85(10):337
Liu W, Asheghi M. 2004. Phonon-boundary scattering in ultrathin single-crystal silicon layers. *Appl. Phys. Lett.* 84(19):3819–21

Liu W, Asheghi M. 2005. Thermal conduction in ultrathin pure and doped single-crystal silicon layers at high temperatures. *J. Appl. Phys.* 98(12):123523

Liu X, Liu J, Antipina LY, Hu J, Yue C, et al. 2016. Direct Fabrication of Functional Ultrathin Single-Crystal Nanowires from Quasi-One-Dimensional van der Waals Crystals. *Nano Lett.* 16(10):6188–95

Ljungberg, Karin, Anders Söderbärg and YB. 1993. Spontaneous bonding of hydrophobic silicon surfaces. *Appl. Phys. Lett.* 62(12):1362–64

Losego MD, Grady ME, Sottos NR, Cahill DG, Braun P V. 2012. Effects of chemical bonding on heat transport across interfaces. *Nat. Mater.* 11(6):502–6

Lu L, Yi W, Zhang DL. 2001. 3Ω Method for Specific Heat and Thermal Conductivity Measurements. *Rev. Sci. Instrum.* 72(7):2996

Lü X, Chu JH, Shen WZ. 2003. Modification of the lattice thermal conductivity in semiconductor rectangular nanowires. *J. Appl. Phys.* 93(2):1219–29

Lundstrom M. 2009. *Fundamentals of Carrier Transport*. Cambridge University Press, Cambridge, England

Ma J, Zhang Q, Mayo A, Ni Z, Yi H, et al. 2015. Thermal conductivity of electrospun polyethylene nanofibers. *Nanoscale*. 7(40):16899–908

Maire J, Nomura M. 2014. Reduced thermal conductivities of Si one-dimensional periodic structure and nanowire. *Jpn. J. Appl. Phys.* 53(6):06JE09

Majumdar A. 2004. Thermoelectricity in semiconductor nanostructures. *Science (80-.).* 303(5659):777–78

Martin P, Aksamija Z, Pop E, Ravaioli U. 2009. Impact of phonon-surface roughness scattering on thermal conductivity of thin Si nanowires. *Phys. Rev. Lett.* 102(12):125503

Mavrokefalos A, Moore AL, Pettes MT, Shi L, Wang W, Li X. 2009. Thermoelectric and structural characterizations of individual electrodeposited bismuth telluride nanowires. *J. Appl. Phys.* 105(10):104318

Mavrokefalos A, Pettes MT, Zhou F, Shi L. 2007. Four-probe measurements of the in-plane thermoelectric properties of nanofilms. *Rev. Sci. Instrum.* 78(3):034901

McCarten J, Maher M, Adelman TL, Thorne. RE. 1989. Size effects and charge-density-wave pinning in NbSe3. *Phys. Rev. Lett.* 63(26):2841–44

McGaughey AJH, Jain A. 2012. Nanostructure thermal conductivity prediction by Monte Carlo sampling of phonon free paths. *Appl. Phys. Lett.* 100(6):061911

Meitl M a., Zhu Z-T, Kumar V, Lee KJ, Feng X, et al. 2006. Transfer printing by kinetic control of adhesion to an elastomeric stamp. *Nat. Mater.* 5(1):33–38

Miller RE, Shenoy VB. 2000. Size-dependent elastic properties of nanosized structural elements. *Nanotechnology*. 11(3):139–47

Mingo N. 2003. Calculation of Si nanowire thermal conductivity using complete phonon dispersion relations. *Phys. Rev. B.* 68(11):113308

Mingo N, Hauser D, Kobayashi NP, Plissonnier M, Shakouri a. 2009. Nanoparticle-in-alloy approach to efficient thermoelectrics: Silicides in SiGe. *Nano Lett.* 9(2):711–15

Mingo N, Yang L, Li D, Majumdar A. 2003. Predicting the Thermal Conductivity of Si and Ge Nanowires. *Nano Lett.* 3(12):1713–16

Minnich AJ, Johnson JA, Schmidt AJ, Esfarjani K, Dresselhaus MS, et al. 2011. Thermal conductivity spectroscopy technique to measure phonon mean free paths. *Phys. Rev. Lett.* 107(9):095901

Momose HS, Ohguro T, Kojima K, Nakamura S, Toyoshima Y. 2003. 1.5-nm Gate oxide CMOS

on [110] surface-oriented Si substrate. *IEEE Trans. Electron Devices*. 50(4):1001–8
Moore AL, Saha SK, Prasher RS, Shi L. 2008. Phonon backscattering and thermal conductivity suppression in sawtooth nanowires. *Appl. Phys. Lett.* 93(8):6–8
Moore AL, Shi L. 2010. On errors in thermal conductivity measurements of suspended and supported nanowires using micro-thermometer devices from low to high temperatures. *Meas. Sci. Technol.* 22(1):015103
Morelli DT, Heremans JP, Beetz CP, Yoo WS, Matsunami H. 1993. Phonon-electron scattering in single crystal silicon carbide. *Appl. Phys. Lett.* 63(23):3143–45
Nguyen B-Y, Celler G, Mazuré C. 2009. A Review of SOI Technology and its Applications. *J. Integr. Circuits Syst.* 2(4):51–54
Nilsson G, Nelin G. 1972. Study of the Homology between Silicon and Germanium by Thermal-Neutron Spectrometry. *Phys. Rev. B.* 6(10):3777–86
Nilsson SG, Borrisé X, Montelius L. 2004. Size effect on Young's modulus of thin chromium cantilevers. *Appl. Phys. Lett.* 85(16):3555–57
Nomura K, Kamiya T, Ohta H, Uruga T, Hirano M, Hosono H. 2007. Local coordination structure and electronic structure of the large electron mobility amorphous oxide semiconductor In-Ga-Zn-O: Experiment and *ab initio* calculations. *Phys. Rev. B.* 75(3):035212
Nomura M, Maire J. 2015. Mechanism of the Reduced Thermal Conductivity of Fishbone-Type Si Phononic Crystal Nanostructures. *J. Electron. Mater.* 44(6):1426–31
Núñez-Regueiro M, Lopez-Castillo J, Ayache C. 1985. Thermal conductivity of 1T-TaS2 and 2H-TaSe2. *Phys. Rev. Lett.* 55(18):1931–34
O'Brien PJ, Shenogin S, Liu J, Chow PK, Laurencin D, et al. 2013. Bonding-induced thermal conductance enhancement at inorganic heterointerfaces using nanomolecular monolayers. *Nat. Mater.* 12(2):118–22
Ong NP. 1978. Two-band model for NbSe3 (Ohmic regime). *Phys. Rev. B.* 18(10):5272–79
Peierls R. 1955. *Quantum Theory of Solids*. Oxford Univ Press, New York
Pettes MT, Shi L. 2009. Thermal and Structural Characterizations of Individual Single-, Double-, and Multi-Walled Carbon Nanotubes. *Adv. Funct. Mater.* 19(24):3918–25
Poncharal P, Wang ZL, Ugarte D, de Heer WA. 1999. Electrostatic Deflections and Electromechanical Resonances of Carbon Nanotubes. *Science (80-.).* 283(5407):
Ponomareva I, Srivastava D, Menon M. 2007. Thermal conductivity in thin silicon nanowires: Phonon confinement effect. *Nano Lett.* 7(5):1155–59
Pop E. 2010. Energy dissipation and transport in nanoscale devices. *Nano Res.* 3(3):147–69
Pop E, Mann D, Wang Q, Goodson K, Dai H. 2006. Thermal conductance of an individual single-wall carbon nanotube above room temperature. *Nano Lett.* 6(1):96–100
Poudel B, Hao Q, Ma Y, Lan Y, Minnich A, et al. 2008. High-thermoelectric performance of nanostructured bismuth antimony telluride bulk alloys. *Science.* 320(5876):634–38
Prasher R. 2009. Acoustic mismatch model for thermal contact resistance of van der Waals contacts. *Appl. Phys. Lett.* 94(4):041905
Qing Q, Jiang Z, Xu L, Gao RX, Mai LQ, Lieber CM. 2014. Free-standing kinked nanowire transistor probes for targeted intracellular recording in three dimensions. *Nat. Nanotechnol.* 9(2):142–47
Raith Software. 2008. Raith NanoPECS Software Description
Ramayya EB, Vasileska D, Goodnick SM, Knezevic I. 2008. Electron transport in silicon nanowires: The role of acoustic phonon confinement and surface roughness scattering. *J. Appl. Phys.* 104(6):063711

Ravichandran J, Yadav AK, Cheaito R, Rossen PB, Soukiassian A, et al. 2013. Crossover from incoherent to coherent phonon scattering in epitaxial oxide superlattices. *Nat. Mater.* 13(2):168–72

Ravichandran NK, Minnich AJ. 2014. Coherent and incoherent thermal transport in nanomeshes. *Phys. Rev. B.* 89(20):205432

Regner KT, Sellan DP, Su Z, Amon CH, McGaughey AJH, Malen J. 2013. Broadband phonon mean free path contributions to thermal conductivity measured using frequency domain thermoreflectance. *Nat. Commun.* 4:1640

Requardt H, Lorenzo JE, Monceau P, Currat R, Krisch M. 2002. Dynamics in the charge-density-wave system NbSe3 using inelastic x-ray scattering with meV energy resolution. *Phys. Rev. B.* 66(21):214303

Sadeghian H, Goosen JFL, Bossche A, Thijsse BJ, Van Keulen F. 2011. Effects of size and surface on the elasticity of silicon nanoplates: Molecular dynamics and semi-continuum approaches. *Thin Solid Films*. 520(1):391–99

Sadhu J, Sinha S. 2011. Room-temperature phonon boundary scattering below the Casimir limit. *Phys. Rev. B - Condens. Matter Mater. Phys.* 84(11):115450

Schroeder DP, Aksamija Z, Rath A, Voyles PM, Lagally MG, Eriksson MA. 2015. Thermal Resistance of Transferred-Silicon-Nanomembrane Interfaces. *Phys. Rev. Lett.* 115(25):256101

Sengupta S, Samudrala N, Singh V, Thamizhavel A, Littlewood PB, et al. 2013. Plasmon mode modifies the elastic response of a nanoscale charge density wave system. *Phys. Rev. Lett.* 110(16):166403

Shanks HR, Maycock PD, Sidles PH, Danielson GC. 1963. Thermal Conductivity of Silicon from 300 to 1400°K. *Phys. Rev.* 130(5):1743–48

Shi L. 2012. Thermal and Thermoelectric Transport in Nanostructures and Low-Dimensional Systems. *Nanoscale Microscale Thermophys. Eng.* 16(2):79–116

Shi L, Li D, Yu C, Jang W, Kim D, et al. 2003. Measuring thermal and thermoelectric properties of one-dimensional nanostructures using a microfabricated device. *J. Heat Transfer*. 125(5):881

Shim HW, Zhou LG, Huang H, Cale TS. 2005. Nanoplate elasticity under surface reconstruction. *Appl. Phys. Lett.* 86(15):151912

Slot E, van der Zant HSJ, O'neill K, Thorne RE. 2004. Crossover from two-dimensional to one-dimensional collective pinning in NbSe3. *Phys. Rev. B - Condens. Matter Mater. Phys.* 69(7):073105

Soffer SB. 1967. Statistical Model for the Size Effect in Electrical Conduction. *J. Appl. Phys.* 38(4):1710

Sondheimer EH. 1952. The mean free path of electrons in metals. *Adv. Phys.* 1(1):1–42

Sondheimer EH. 2001. The mean free path of electrons in metals. *Adv. Phys.* 50(6):499–537

Steinhögl W, Schindler G, Steinlesberger G, Engelhardt M. 2002. Size-dependent resistivity of metallic wires in the mesoscopic range. *Phys. Rev. B.* 66(7):075414

Tang J, Wang HT, Lee DH, Fardy M, Huo Z, et al. 2010. Holey silicon as an efficient thermoelectric material. *Nano Lett.* 10(10):4279–83

Termentzidis K, Barreteau T, Ni Y, Merabia S, Zianni X, et al. 2013. Modulated SiC nanowires: Molecular dynamics study of their thermal properties. *Phys. Rev. B.* 87(12):125410

Tham D, Nam C-Y, Fischer J ?E. 2006. Microstructure and Composition of Focused-Ion-Beam-Deposited Pt Contacts to GaN Nanowires. *Adv. Mater.* 18(3):290–94

Thompson S, Packan P, Bohr M. 1998. MOS Scaling : Transistor Challenges for the 21st Century. *Intel Technol. J.* 1–19

Tian B, Xie P, Kempa TJ, Bell DC, Lieber CM. 2009. Single-crystalline kinked semiconductor nanowire superstructures. *Nat. Nanotechnol.* 4(12):824–29

Tian Z, Esfarjani K, Shiomi J, Henry AS, Chen G. 2011. On the importance of optical phonons to thermal conductivity in nanostructures. *Appl. Phys. Lett.* 99(5):053122

Timp G, Bude J, Baumann F, Bourdelle K., Boone T, et al. 2000. The relentless march of the MOSFET gate oxide thickness to zero. *Microelectron. Reliab.* 40(4–5):557–62

Togo A, Oba F, Tanaka I. 2008. First-principles calculations of the ferroelastic transition between rutile-type and CaCl2-type SiO2 at high pressures. *Phys. Rev. B.* 78(13):134106

Tomić S, Biljakovic K, Djurek D, Cooper JR, Monceau P, Meerschaut A. 1981. Calorimetric study of the phase transitions in niobium triselenide NbSe3. *Solid State Commun.* 38(2):109–12

Tong Q-Y, Lee T-H, Gösele U, Reiche M, Ramm J, Beck E. 1997. The Role of Surface Chemistry in Bonding of Standard Silicon Wafers. *J. Electrochem. Soc.* 144(1):384

Tong Q-Y, Schmidt E, Gösele U, Reiche M. 1994. Hydrophobic silicon wafer bonding. *Appl. Phys. Lett.* 64(5):625

Tong QQY. 1999. Low Vacuum Wafer Bonding. *Electrochem. Solid-State Lett.* 1(1):52

Tong QY, Gan Q, Hudson G, Fountain G, Enquist P, et al. 2003. Low-temperature hydrophobic silicon wafer bonding. *Appl. Phys. Lett.* 83(23):4767–69

Van Smaalen S, De Boer JL, Meetsma A, Graafsma H, Sheu HS, et al. 1992. Determination of the structural distortions corresponding to the q1- and q2-type modulations in niobium triselenide NbSe3. *Phys. Rev. B.* 45(6):3103–6

Venkatasubramanian R. 2000. Lattice thermal conductivity reduction and phonon localizationlike behavior in superlattice structures. *Phys. Rev. B.* 61(4):3091–97

Volz SG, Chen G. 1999a. Molecular dynamics simulation of thermal conductivity of silicon nanowires. *Appl. Phys. Lett.* 75(14):2056

Volz SG, Chen G. 1999b. Molecular dynamics simulation of thermal conductivity of silicon nanowires. *Appl. Phys. Lett.* 75(1999):2056–58

Wang J-S, Li B. 2004. Intriguing Heat Conduction of a Chain with Transverse Motions. *Phys. Rev. Lett.* 92(7):074302

Wang J, Xiong R, Yin D, Li C, Tang Z, et al. 2006. Low-temperature specific heat of the quasi-two-dimensional charge-density wave compound K Mo6 O17. *Phys. Rev. B - Condens. Matter Mater. Phys.* 73(19):193102

Wang Y, Lu Z, Ruan X. 2016. First principles calculation of lattice thermal conductivity of metals considering phonon-phonon and phonon-electron scattering. *J. Appl. Phys.* 119(22):225109

Ward A, Broido DA. 2010. Intrinsic phonon relaxation times from first-principles studies of the thermal conductivities of Si and Ge. *Phys. Rev. B.* 81(8):085205

Weathers A, Shi L. 2013. Thermal Transport Measurement Techniques for Nanowires and Nanotubes. *Annu. Rev. Heat Transf.* 16(1):101–34

Werheit H, Kuhlmann U, Herstell B, Winkelbauer W. 2009. Reliable measurement of Seebeck coefficient in semiconductors. *J. Phys. Conf. Ser.* 176:012037

Wingert MC, Chen ZCY, Dechaumphai E, Moon J, Kim J, et al. 2011a. Thermal Conductivity of Ge and Ge–Si Core–Shell Nanowires in the Phonon Confinement Regime. *Nano Lett.* 11(12):5507–13

Wingert MC, Chen ZCY, Dechaumphai E, Moon J, Kim JH, et al. 2011b. Thermal conductivity of Ge and Ge-Si core-shell nanowires in the phonon confinement regime. *Nano Lett.*

11(12):5507–13
Wingert MC, Chen ZCY, Kwon S, Xiang J, Chen R. 2012. Ultra-sensitive thermal conductance measurement of one-dimensional nanostructures enhanced by differential bridge. *Rev. Sci. Instrum.* 83(2):114901
Wingert MC, Kwon S, Cai S, Chen R. 2016a. Fluid-like Surface Layer and Its Flow Characteristics in Glassy Nanotubes. *Nano Lett.* 16(12):7545–50
Wingert MC, Kwon S, Hu M, Poulikakos D, Xiang J, Chen R. 2015. Sub-amorphous Thermal Conductivity in Ultrathin Crystalline Silicon Nanotubes. *Nano Lett.* 15(4):2605–11
Wingert MC, Zheng J, Kwon S, Chen R. 2016b. Thermal transport in amorphous materials: a review. *Semicond. Sci. Technol.* 31(11):113003
Wolfe J. 2005. *Imaging Phonons: Acoustic Wave Propagation in Solids*. Cambridge University Press
Xi X, Zhao L, Wang Z, Berger H, Forró L, et al. 2015. Strongly enhanced charge-density-wave order in monolayer NbSe2. *Nat. Nanotechnol.* 10(9):765–69
Xiong S, Kosevich Y a., Sääskilahti K, Ni Y, Volz S. 2014. Tunable thermal conductivity in silicon twinning superlattice nanowires. *Phys. Rev. B.* 90:195439
Yamamoto T, Watanabe S, Watanabe K. 2004. Universal Features of Quantized Thermal Conductance of Carbon Nanotubes. *Phys. Rev. Lett.* 92(7):075502
Yang J, Shen M, Yang Y, Evans WJ, Wei Z, et al. 2014. Phonon Transport through Point Contacts between Graphitic Nanomaterials. *Phys. Rev. Lett.* 112(20):205901
Yang J, Yang Y, Waltermire SW, Gutu T, Zinn A a., et al. 2011a. Measurement of the intrinsic thermal conductivity of a multiwalled carbon nanotube and its contact thermal resistance with the substrate. *Small*. 7(16):2334–40
Yang J, Yang Y, Waltermire SW, Wu X, Zhang H, et al. 2011b. Enhanced and switchable nanoscale thermal conduction due to van der Waals interfaces. *Nat. Nanotechnol.* 7(2):91–95
Yang L, Tao Y, Liu J, Liu C, Zhang Q, et al. 2019. Distinct Signatures of Electron–Phonon Coupling Observed in the Lattice Thermal Conductivity of NbSe 3 Nanowires. *Nano Lett.* 19(1):415–21
Yang L, Yang Y, Zhang Q, Zhang Y, Jiang Y, et al. 2016. Thermal conductivity of individual silicon nanoribbons. *Nanoscale*. 8(41):17895–901
Yang L, Zhang Q, Cui Z, Gerboth M, Zhao Y, et al. 2017. Ballistic Phonon Penetration Depth in Amorphous Silicon Dioxide. *Nano Lett.* 17(12):7218–25
Yang N, Zhang G, Li B. 2010. Violation of Fourier's law and anomalous heat diffusion in silicon nanowires. *Nano Today*. 5(2):85–90
Yao H, Yun G, Bai N, Li J. 2012. Surface elasticity effect on the size-dependent elastic property of nanowires. *J. Appl. Phys.* 111(8):083506
Yoshikawa T, Yagi T, Oka N, Jia J, Yamashita Y, et al. 2013. Thermal Conductivity of Amorphous Indium--Gallium--Zinc Oxide Thin Films. *Appl. Phys. Express*. 6(2):021101
Yu C, Shi L, Yao Z, Li D, Majumdar A. 2005. Thermal conductance and thermopower of an individual single-wall carbon nanotube. *Nano Lett.* 5(9):1842–46
Yu J-K, Mitrovic S, Tham D, Varghese J, Heath JR. 2010. Reduction of thermal conductivity in phononic nanomesh structures. *Nat. Nanotechnol.* 5(10):718–21
Zaslavsky GM. 2002. Chaos, fractional kinetics, and anomalous transport. *Phys. Rep.* 371(6):461–580
Zhang G, Li B. 2005. Anomalous vibrational energy diffusion in carbon nanotubes. *J. Chem. Phys.* 123(1):2003–6

Zhang Q, Cui Z, Wei Z, Chang SY, Yang L, et al. 2017. Defect facilitated phonon transport through kinks in boron carbide nanowires. *Nano Lett.* 17(6):3550–55
Zhang Q, Liu C, Liu X, Liu J, Cui Z, et al. 2018. Thermal transport in quasi-1D van der Waals crystal Ta2Pd3Se8 nanowires: size and length dependence. *ACS Nano*. 12(3):2634–42
Zheng J, Wingert MC, Dechaumphai E, Chen R. 2013. Sub-picowatt/kelvin resistive thermometry for probing nanoscale thermal transport. *Rev. Sci. Instrum.* 84(11):114901
Zheng Q, Mei AB, Tuteja M, Sangiovanni DG, Hultman L, et al. 2017. Phonon and electron contributions to the thermal conductivity of VNx epitaxial layers. *Phys. Rev. Mater.* 1(6):065002
Zhong Z, Wingert MC, Strzalka J, Wang H-H, Sun T, et al. 2014. Structure-induced enhancement of thermal conductivities in electrospun polymer nanofibers. *Nanoscale*. 6(14):8283
Zhou F, Szczech J, Pettes MT, Moore AL, Jin S, Shi L. 2007. Determination of transport properties in chromium disilicide nanowires via combined thermoelectric and structural characterizations. *Nano Lett.* 7(6):1649–54
Zhou Y, Zhang X, Hu M. 2017. Nonmonotonic Diameter Dependence of Thermal Conductivity of Extremely Thin Si Nanowires: Competition between Hydrodynamic Phonon Flow and Boundary Scattering. *Nano Lett.* 17(2):1269–76
Zhu X, Cao Y, Zhang J, Plummer EW, Guo J. 2015. Classification of charge density waves based on their nature. *Proc. Natl. Acad. Sci.* 112(8):2367–71
Zhu Y, Xu F, Qin Q, Fung WY, Lu W. 2009. Mechanical properties of vapor-liquid-solid synthesized silicon nanowires. *Nano Lett.* 9(11):3934–39
Ziman J. 1960. *The Theory of Transport Phenomena in Solids*. Clarendon Press, Oxford
Ziman JM. 2011. *Electrons and Phonons of Solides*. Oxford University Press
Zou J, Balandin A. 2001. Phonon heat conduction in a semiconductor nanowire. *J. Appl. Phys.* 89(5):2932–38